ELECTRON SCATTERING IN GRAPHENE BY ELECTRIC AND MAGNETIC DIPOLE

By

Yohannes Achenefe

SUBMITTED IN PARTIAL FULFILLMENT OF THE
REQUIREMENTS FOR THE DEGREE OF
DOCTOR OF PHILOSOPHY
AT
ADDIS ABBABA UNIVERSITY
ADDIS ABABA, ETHIOPIA
FEB 2016

ADDIS ABBABA UNIVERSITY
DEPARTMENT OF
PHYSICS

The undersigned hereby certify that they have read and recommend to the Faculty of Graduate Studies for acceptance a thesis entitled "**Electron Scattering in Graphene by Electric and Magnetic dipole**" by **Yohannes Achenefe** in partial fulfillment of the requirements for the degree of **Doctor of Philosophy**.

Dated: Feb 2016

External Examiner: _____
Dr.

Research Supervisor: _____
Proff. Vadim N. Mal'nev

Examing Committee: _____
Dr.

_____
Dr.

ADDIS ABBABA UNIVERSITY

Date: **Feb 2016**

Author: **Yohannes Achenefe**

Title: **Electron Scattering in Graphene by Electric and Magnetic dipole**

Department: **Physics**

Degree: **Ph.D.** Convocation: **June** Year: **2016**

Permission is herewith granted to Addis Abbaba University to circulate and to have copied for non-commercial purposes, at its discretion, the above title upon the request of individuals or institutions.

Signature of Author

To my family

Table of Contents

List of Figures

Abstract

The two-dimensional form of graphite (graphene) has been obtained only very recently, and immediately attracted great deal of attention. Electrons in graphene, obeying linear dispersion relation, behave like massless relativistic particles. It is believed that graphene can replace silicon in electronics world. But the biggest obstacle is that graphene itself does not have a band gap. This property makes graphene always conducting and conduction can not be completely turned off. One of the most challenging task is to learn how to control the electron behavior using electric fields in this two-dimensional layer. In this work we wanted to learn (and to propose mechanisms) "How to control the electron motion in graphene using magnetic dipole and electric dipole?". The second idea was to investigate if it is possible to use magnetic fields of large suspended nanomagnet to open a gap in the energy spectrum of graphene.

The elastic electron scattering by impurities with electric and magnetic dipoles in graphene is studied with the help of Born approximation. Both types of scatterers give the nonzero cross section of backscattering. The scattering by the impurities with electric dipoles is more efcient even comparing to the scattering by the nanomagnets with anomalous magnetic moments. A comparison of the electron scattering transport cross sections by charged impurities and impurities with electric dipole moments shows that they can be comparable. The scattering by the impurities electric dipoles can be important in limiting the electron mobility in graphene along with the Coulomb scattering.

The elastic electron scattering by a nonuniform magnetic eld of a remote nanomagnets in the graphene is also considered with the help of the modied Born approximation. The nanomagnets are modeled by point like magnetic dipoles oriented transversally and parallel to the graphene plane. They can form rather high magnetic elds without any damage of the graphene plane. The electron scattering cross sections are obtained in the closed form and analyzed numerically. It is shown that this mechanism of scattering has nonzero backscattering cross section and can considerably affect the graphene conductivity.

Acknowledgements

This work is dedicated to the late Professor Vadim N. Malnev who was our teacher, mentor, and colleague. His continuous guidance from the early years of confusion (MSc study) to this time PhD work was quite unstinting. He departed suddenly while this work was in its final stage. We greatly acknowledge his invaluable contributions. Let his soul rest in peace.

I am also thankful to Dr. Teshome Senbeta, my supervisor, for his many suggestions and constant support during this work. He shared with me his knowledge and provided many useful references and friendly encouragement.

Of course, I am grateful to my parents for their patience and *love*. My wife Habtam Gizat and my son Daniel Yohannes (for special effects)

Finally, I wish to thank the following:

- All my friends (for all the good and bad times we had together)
- Department of Physics, Addis Ababa University all necessary support
- Graduate program, Addis Ababa University Financial support
- Dire-Dawa University for sponsorship of my study

.

Chapter 1

Introduction

1.1 Allotropes of Carbon

1.1.1 Diamond

Diamond is one of the best known allotropes of carbon, whose hardness and high dispersion of light make it useful for industrial applications and jewelry. Diamond is an excellent abrasive and makes it hold polish and luster extremely well.

In diamonds, each carbon atom is covalently bonded to four other carbons in a tetrahedron (a three-sided pyramid). The four valence electrons of each carbon atom participate in the formation of very strong covalent bonds. These bonds have the same strength in all directions. This gives diamonds their great hardness.

Since there are no free electrons to wander through the structure, diamonds are excellent insulators. The brilliance and "fire" of cut diamonds is due to a very high index of refraction (2.42) and the strong dispersion of light; properties which are related to the structure of diamonds. Diamond will scratch all other materials. It is the best conductor of heat that we know, conducting up to five times the amount

that copper does. Diamond also conducts sound, but not electricity; it is an insulator, and its electrical resistance, optical transmissivity and chemical inertness are correspondingly remarkable.

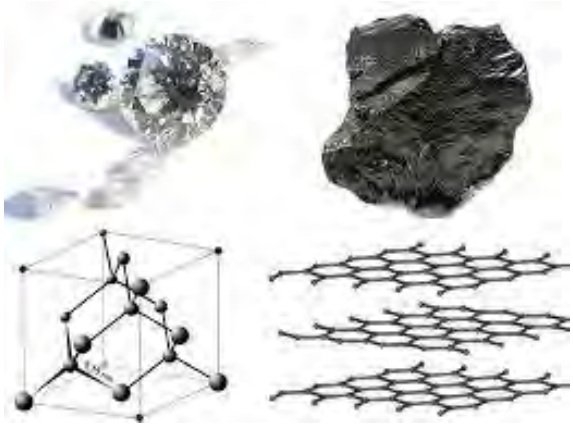

Figure 1.1: Structure of Diamond and Graphite

1.1.2 Graphite

Graphite is one of the most common allotropes of carbon. Unlike diamond, graphite is a conductor, and can be used, for instance, as the material in the electrodes of an electrical arc lamp. Graphite holds the distinction of being the most stable form of solid carbon ever discovered. Graphite is named by Abraham G. Werner in 1789, it is a Greek word meaning "to draw/write", for its use in pencils.

Graphite has a layered, planar structure. In each layer, the carbon atoms are arranged in a honeycomb lattice with separation of 0.142 nm, and the distance between planes is 0.335 nm. Graphite is able to conduct electricity due to the unpaired fourth electron in each carbon atom. This unpaired 4th electron forms delocalised planes above and below the planes of the carbon atoms. These electrons are free to move,

so are able to conduct electricity. However, the electricity is only conducted within the plane of the layers.

Natural and crystalline graphites are not often used in pure form as structural materials due to their shear-planes, brittleness and inconsistent mechanical properties. Of all materials, graphite has the highest melting point (4200 K), the highest thermal conductivity (3000W/mK) and a high room temperature electron mobility $(30,000 cm^2/(Vs)$ [1, 2, 3].

1.1.3 Fullerene

In 1985, the discovery of another unique carbon system took place, the observation of the C_{60} fullerene molecule [4]. The fullerene molecule consists of 60 carbon atoms with mostly sp^2 bonding and appropriate π bonding to form a closed surface with hollow sphere. Because of topological restrictions, fullerenes, in general, have 12 pentagonal rings and any numbers of hexagonal rings, thereby generating a large variety of C_n fullerene molecules. The C_{60} molecule with full icosahedral symmetry can be regarded as the first isolated carbon nanosystem. Fullerenes stimulated and motivated a large scientific community into new research directions from the time of their discovery up to the end of the twentieth century, but fullerene-based applications remain sparse to date.

1.1.4 Carbon Nanotube

Carbon nanotubes (CNTs) are allotropes of carbon with a cylindrical nanostructure . They are very thin lightweight hollow tubes made up of carbon atoms [5, 6]. A carbon nanotube is like a sheet of graphite that is rolled into a cylinder, with distinctive

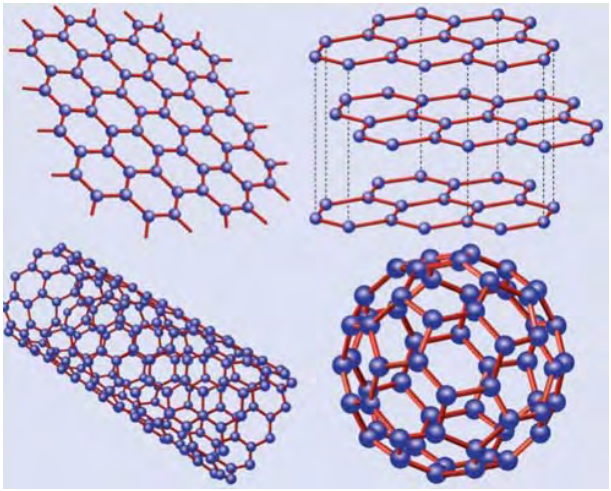

Figure 1.2: Graphene(top left) is a honeycomb lattice of carbon atoms. Graphite (top right) can be viewed as a stack of graphene layers. Carbon Nanotubes rolled up cylinders of graphene(bottom left). Fullerenes (C_{60}) molecules consisting of wrapped graphene by introduction of pentagons on hexagonal lattice. [**?**]

hexagonal latticework making up the sheet. Carbon nanotubes are extremely small; the diameter of one carbon nanotube is one nanometer, which is one ten-thousandth (1/10,000) the diameter of a human hair. Carbon nanotubes can be produced to varying lengths [7, 8].

Carbon nanotubes are classified according to their structures: single-wall nanotubes (SWNTs), double-wall nanotubes (DWNTs), and multi-wall nanotubes (MWNTs). The different structures have individual properties that make the nanotubes appropriate for different applications [8, 9]. Because of their unique mechanical, electrical, and thermal properties, carbon nanotubes present exciting opportunities for scientific research and industrial and commercial applications. There is much potential for CNTs in the composites industry [7].

The great interest in the fundamental properties of carbon nanotubes and in their exploitation through a wide range of applications is due to their unique properties,

including high thermal and electrical conductivity, optical properties, flexibility, high tensile strength (100 times stronger than steel per unit of weight), light weight. When applied to products, these properties provide tremendous advantages. For example, when used in polymers, bulk carbon nanotubes can improve the thermal and electrical properties of the products [10, 11, 12].

After more than a decade and a half of intense activity in carbon nanotube research, more and more attention is now being focused on the practical applications of the many unique and special properties of carbon nanotubes [13]. Further background information on the synthesis, structure, properties and applications of carbon nanotubes can be found in [10, 14]. Today, carbon nanotubes find application in many different products, and researchers continue to explore creative new applications.

1.2 Graphene

The interest in a single atomic layer of carbon (called graphene; see Fig. 1.2) goes back to the pioneering theoretical work of Wallace in 1947 [15] which was for many years used as a model system for all carbons. This very early work provides a framework for comparing the structures of graphite, fullerenes, carbon nanotubes and other nanocarbons. The synthesis of single-layer graphene was actually reported by Boehm in 1962 [16], but this early discovery was neither confirmed nor followed up for many years.

For a long time, one was convinced that two dimensional crystals can not exist because thermal fluctuations will destroy it [17, 18, 19, 20, 21]. A lot of effort in the past to create atomically thin films of other materials failed since the films became unstable and tended to separate and clump up rather than form perfect layers. It

come on a big surprise when in 2004 a group of scientists in Manchester university led by Andre Geim and Kostya Novoselov succeeded to extract a stable single layer of carbon atoms. Nowadays the stability of graphene is explained by postulating small out-of-plane corrugations [22].

The preparation of monolayer graphene by Novoselov et al. [23], using a simple Scotch tape method to prepare and transfer monolayer graphene from the c-face of graphite to a suitable substrate such as SiO_2. The measurement of the electrical and optical properties of monolayer graphene done on this substrate [24]. The Novoselov and Geim studies of transport in few layer graphene in 2004 [23] led to a renewed interest in monolayer and few layer graphene. And to an in-depth study of the unique properties of this material in the monolayer and bilayer limit. Surprisingly, this very basic system, which had been conceptually utilized by researchers over a period of many decades, suddenly appeared on the experimental scene. Graphene demonstrate many novel physical properties that were not even imagined previously [24, 25]. The discovery of these novel properties launched a rush into the study of graphene science in the first decade of the twenty-first century, and culminating in the 2010 Nobel Prize in physics [26].

Graphene has the outstanding mechanical properties [27] (breaking strength $\sim 40N/m$, Youngs modulus $\sim 1TPa$) and thermal properties [28, 29] (room temperature thermal conductivity $\sim 3000Wm^{-1}K^{-1}$ [29]). The scientific interest in graphene was stimulated [30, 31] by the widespread report of the relativistic (massless) electronic properties of the conduction electrons (and holes) in a single layer less than 1 nm thick. The mobility of graphene reaching $\mu = 200,000cm^2/Vs$ at room temperature for freely suspended graphene [30, 31, 32, 33, 34, 35]. Other unusual properties have been

predicted and demonstrated experimentally. Some of such properties are the half-integer quantum Hall effect in monolayer graphene [36] and the integer quantum Hall effect in bilayer graphene [36, 37], operation as a transparent conductor [38], Klein tunneling [39, 40, 41, 42, 43, 44], negative refractive index and Veselago lensing [42]. Applications such as filters for composite materials, as super-capacitors, batteries, interconnects and field emitters are being developed. It is still too early to say to what extent graphene will be able to compete with carbon nanotubes and other established materials systems in the applications world [45]. Although nanotubes and graphene are both carbon-based nanostructures, they have different properties related to the planar aspects of graphene and the tubular aspects of nanotubes, and this basic difference should distinguish their optimal usage in applications.

1.3 Graphene Applications

1.3.1 Transistors

A key electrical property of graphene is its electron mobility (the speed at which electrons move within it when a voltage is applied) [30]. Graphenes electron mobility is faster than any known material and researchers are developing methods to build transistors on graphene that would be much faster than the transistors currently built on silicon wafers [46, 47, 48, 50, 51, 52]. The ability to build high frequency transistors with graphene is possible because of the higher speed at which electrons in graphene move compared to electrons in silicon [53, 54].

In 2008, the smallest transistor so far, one atom thick, 10 atoms wide was made of graphene [55, 56]. IBM announced in December 2008 that they had fabricated

and characterized graphene transistors operating at GHz frequencies [47]. In May 2009, an n-type transistor was announced meaning that both n and p-type graphene transistors had been created [57, ?]. A functional graphene integrated circuit was demonstrated a complementary inverter consisting of one p- and one n-type graphene transistor [48]. In 2013 researchers reported the creation of transistors printed on flexible plastic that operate at 25 gigahertz, sufficient for communications circuits and that can be fabricated at scale.

1.3.2 Integrated circuits

For integrated circuits, graphene has a high carrier mobility, as well as low noise, allowing it to be used as the channel in a field-effect transistor [58, 59]. Single sheets of graphene are hard to produce and even harder to make on an appropriate substrate [13].

According to a January 2010 report,[60] graphene was epitaxially grown on SiC in a quantity and with quality suitable for mass production of integrated circuits [61]. At high temperatures, the quantum Hall effect could be measured in these samples. IBM built 'processors' using 100 GHz transistors on 2-inch (51 mm) graphene sheets [62]. In June 2011, IBM researchers announced that they had succeeded in creating the first graphene-based integrated circuit, a broadband radio mixer [61]. The circuit handled frequencies up to 10 GHz. Its performance was unaffected by temperatures up to 127^0 C. In June 2013 an 8 transistor 1.28 GHz ring oscillator circuit was described [62]. Graphene does not have an energy band-gap, which presents a hurdle for its applications in digital logic gates. The efforts to induce a band-gap in graphene via quantum confinement or surface functionalization have not resulted in

a breakthrough.

1.3.3 Optoelectronics

Another interesting application in which we will soon begin to see graphene used on a commercial scale is that in optoelectronics; specifically touch screens, liquid crystal displays (LCD) and organic light emitting diodes (OLEDs)[63, 64, 65]. For a material to be able to be used in optoelectronic applications, it must be able to transmit more than 90 percent of light and also offer electrical conductive properties exceeding $1 \times 10^6 S/m$ and therefore low electrical resistance. Graphene is an almost completely transparent material and is able to optically transmit up to 97.7 percent of light [63]. It is also highly conductive, as we have previously mentioned and so it would work very well in optoelectronic applications such as LCD touchscreens for smartphones, tablet and desktop computers and televisions.

Currently the most widely used material is indium tin oxide (ITO), and the development of manufacture of ITO over the last few decades time has resulted in a material that is able to perform very well in this application. However, recent tests have shown that graphene is potentially able to match the properties of ITO, even in current (relatively under-developed) states. Also, it has recently been shown that the optical absorption of graphene can be changed by adjusting the Fermi level. While this does not sound like much of an improvement over ITO, graphene displays additional properties which can enable very clever technology to be developed in optoelectronics by replacing the ITO with graphene. The fact that high quality graphene has a very high tensile strength, and is flexible (with a bending radius of less than the required 5-10mm for rollable e-paper), makes it almost inevitable that it will soon become

utilized in these aforementioned applications.

In terms of potential real-world electronic applications we can eventually expect to see such devices as graphene based e-paper with the ability to display interactive and updatable information and flexible electronic devices including portable computers and televisions.

1.3.4 Photovoltaic Cells

Offering very low levels of light absorption (at around 2.7 percent of white light) whilst also offering high electron mobility means that graphene can be used as an alternative to silicon or ITO in the manufacture of photovoltaic cells [66, 67, 68]. Silicon is currently widely used in the production of photovoltaic cells, but while silicon cells are very expensive to produce, graphene based cells are potentially much less so [69]. When materials such as silicon turn light into electricity it produces a photon for every electron produced, meaning that a lot of potential energy is lost as heat. Recently published research has proved that when graphene absorbs a photon, it actually generates multiple electrons[70]. Also, while silicon is able to generate electricity from certain wavelength bands of light, graphene is able to work on all wavelengths, meaning that graphene has the potential to be as efficient as, if not more efficient than silicon, ITO or (also widely used) gallium arsenide [71]. Being flexible and thin means that graphene based photovoltaic cells could be used in clothing;[72] to help recharge your mobile phone.

1.4 Motivation and Outline

One of the biggest dream for graphene is to use it one day as a replacement of silicon. But the biggest obstacle is that graphene itself does not have a band gap. This property makes graphene always conducting and conduction can not be completely turned off. One of the most challenging task is to learn how to control the electron behavior using electric fields in this two-dimensional (2D) layer. This task is made complicated by the so called Klein effect according to which Dirac electrons in graphene can tunnel through any electric barrier [41, 94]. In this thesis we wanted to learn (and to propose mechanisms) "How to control the electron motion in graphene using magnetic dipole and electric dipole?". The second motivation was to investigate if it is possible to use magnetic fields of large suspended nanomagnet to open a gap in the energy spectrum of graphene.

In order to tackle these questions, we approached the problem in this directions: First using Dirac equations for massless particle in graphene in the external scattering fields, we developed our model based on the Born approximation. The scattering amplitude, differential cross sections, transport cross sections and backscattering cross section are calculated; several quantities of interest are also calculated. And, numerical we analysis the results.

The thesis is organised as follows

- Chapter 2: The electronic properties of graphene will be explained; the crystal structure of graphene, the tight binding model of monolayer and bilayer graphene, the intrinsic density of states, conductivity, mobility, the integer quantum Hall effect in both mono layer and bilayer graphene is briefly presented.

- Chapter 3: The 2D scattering theory for schrodinger electrons and Dirac electrons separately reviewed. By using both the partial wave method and Born approximation the scattering amplitude, differential cross section and transport cross section calculated for Schrodinger electrons. As already done by Katsnelson and Novikov, using the the partial wave method we calculate scattering amplitude, differential cross section and transport cross section for Dirac electrons.

- Chapter 4: Electron scattering in graphene by electric dipole and magnetic dipole will be presented, in this chapter we develop our own model of the Born approximation. The scattering of electrons by electric dipole gives large contribution compared to magnetic dipole scattering. The electric dipole scattering is even comparable to coulomb scattering. Where as the magnetic scattering depend on the size of the magnetic dipole which again affect the surface of graphene plane. The graphene plane is one atomic thick which can be affected by large size magnetic dipole.

- Chapter 5: Electron scattering in graphene by large suspended nanomagnet is discussed. We assume the magnetic dipole is suspended above the graphene plane. First when the magnetic field of the dipole perpendicular to the graphene plane, we calculate the differential cross section and transport cross section. Again similar calculation is done when the magnetic field is parallel to the graphene plane. Finally the obtained result is analysed numerically.

Chapter 2

Electronic Properties of Graphene

2.1 Introduction

More than sixty years ago, Wallace [15] modeled the electronic band structure of graphene. Research into graphene was stimulated by interest in the properties of bulk graphite because, from a theoretical point of view, two-dimensional graphene serves as a building block for the three-dimensional material. Following further work, the tight-binding model of electrons in graphite, that takes into account coupling between layers [73, 74, 75]. As well as serving as the basis for models of carbon-based materials including graphite, buckyballs, and carbon nanotubes [76, 77, 78, 79, 80, 81, 82], the honeycomb lattice of graphene has been used theoretically to study Dirac fermions in a condensed matter system [83, 84]. Since the experimental isolation of individual graphene flakes [36], and the observation of the integer quantum Hall effect in monolayers [37, 85] and bilayers [**?**], there has been an explosion of interest in the behavior of chiral electrons in graphene.

Section 2.2 of this chapter devoted to a description of the crystal structure of monolayer graphene. Section 2.3 briefly reviews the tight-binding model of electrons

in condensed matter materials [82, 86], and Section 2.4 describes application to monolayer graphene [**?**, 82, 87]. Then, in Section 2.5, we explain how a Dirac-like Hamiltonian describing massless chiral fermions emerges from the tight-binding model at low energy. The tight-binding model is applied to bilayer graphene in Section 2.6, and Section 2.7 describes transport properties of pristine graphene [30, 88]. In Section 2.8, we describe the integer quantum Hall effect of monolayer and bilayer graphene [37, 85, **?**].

2.2 The Crystal Structure of Monolayer Graphene

2.2.1 The Real Space Structure

Monolayer graphene consists of carbon atoms arranged with a two-dimensional honeycomb crystal structure as shown in Fig. 2.1(a). The honeycomb structure [82, 86] consists of the hexagonal Bravais lattice, Fig. 2.1(b), with a basis of two atoms, labeled A and B, at each lattice point. Throughout this chapter, we use a Cartesian coordinate system with x and y axes in the plane of the graphene crystal, and a z axis perpendicular to the graphene plane. Two-dimensional vectors in the same plane as the graphene are expressed solely in terms of their x and y coordinates, so that, for example, the primitive lattice vectors of the hexagonal Bravais lattice, Fig. 2.1(b), are $\vec{a}_1$ and $\vec{a}_2$ where

$$\begin{aligned} \vec{a}_1 &= (\frac{a}{2}, \frac{\sqrt{3}a}{2}), \\ \vec{a}_2 &= (\frac{a}{2}, -\frac{\sqrt{3}a}{2}), \end{aligned} \tag{2.2.1}$$

and $a = |\vec{a}_1| = |\vec{a}_2|$ is the lattice constant. In graphene, $a = 2.46A^0$ [82]. The lattice constant is the distance between unit cells, where as the distance between carbon

atoms is the carbon-carbon bond length $a_{CC} = a/\sqrt{3} = 1.42A^0$. Note that the honeycomb structure is not a Bravais lattice because atomic positions A and B are not equivalent: it is not possible to connect them with a lattice vector $\vec{R} = n_1\vec{a}_1 + n_2\vec{a}_2$ where n_1 and n_2 are integers. Taken alone, the A atomic positions (or, the B atomic positions) make up an hexagonal Bravais lattice and, in the following, we will often refer to them as the A sublattice (or, the B sublattice).

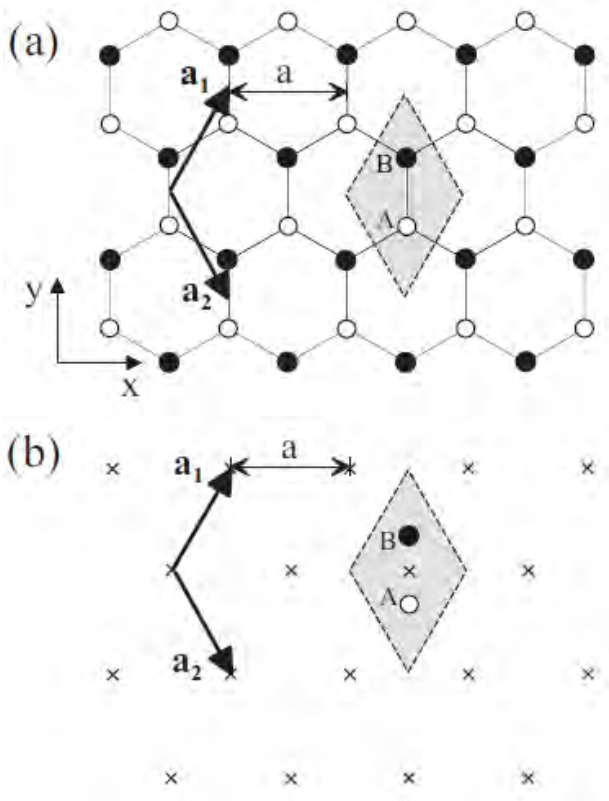

Figure 2.1: (a) The honeycomb crystal structure of monolayer graphene where white (black) circles indicate carbon atoms on A (B) sites and straight lines indicate bonds between them. Vectors $\vec{a}_1$ and $\vec{a}_2$ are primitive lattice vectors of length equal to the lattice constant a. The shaded rhombus is a unit cell containing two atoms, one A and one B.

2.2.2 The Reciprocal Lattice of Graphene

Primitive reciprocal lattice vectors $\vec{b}_1$ and $\vec{b}_2$ satisfying $\vec{a}_1 \cdot \vec{b}_1 = \vec{a}_2 \cdot \vec{b}_2 = 2\pi$ and $\vec{a}_1 \cdot \vec{b}_2 = \vec{a}_2 \cdot \vec{b}_1 = 0$ are given by

$$\begin{aligned} \vec{b}_1 &= (\frac{2\pi}{a}, \frac{2\pi}{\sqrt{3}a}), \\ \vec{b}_2 &= (\frac{2\pi}{a}, -\frac{2\pi}{\sqrt{3}a}). \end{aligned} \tag{2.2.2}$$

The resulting reciprocal lattice is shown in Fig. 2.2, which is an hexagonal Bravais lattice. The first Brillouin zone is hexagonal, as indicated by the shaded region in Fig. 2.2.

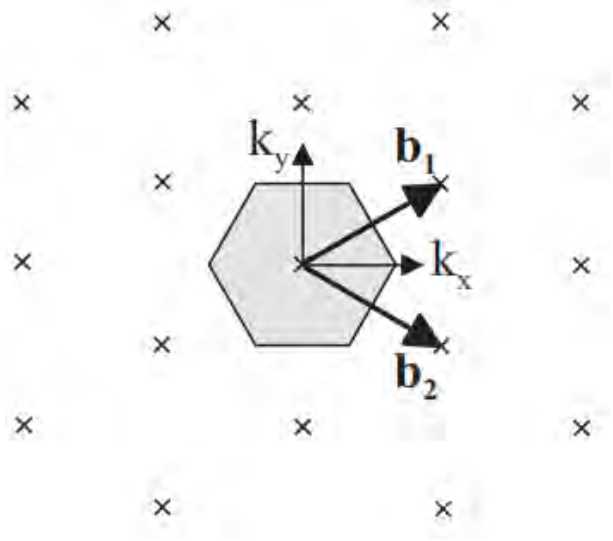

Figure 2.2: The reciprocal lattice of monolayer graphene where crosses indicate reciprocal lattice points, and vectors $\vec{b}_1$ and $\vec{b}_2$ are primitive lattice vectors. The shaded hexagon indicates the first Brillouin zone.

2.2.3 The Atomic Orbitals of Graphene

Each carbon atom has six electrons, of which two are core electrons and four are valence electrons. The latter occupy $2s, 2p_x, 2p_y$, and $2p_z$ orbitals. In graphene, the

orbitals are sp^2 hybridized, meaning that two of the 2p orbitals, the $2p_x$ and $2p_y$ that lie in the graphene plane, mix with the 2s orbital to form three sp^2 hybrid orbitals per atom, each lying in the graphene plane and oriented 120^0 to each other [82]. They form σ bonds with other atoms, shown as straight lines in the honeycomb crystal structure, Fig. 2.1(a). The remaining $2p_z$ orbital for each atom lies perpendicular to the plane, and, when combined with the $2p_z$ orbitals on adjacent atoms in graphene, forms a π orbital. Electronic states close to the Fermi level in graphene are described well by a model taking into account only the orbital, meaning that the tight-binding model can include only one electron per atomic site, in a $2p_z$ orbital.

2.3 The Tight-Binding Model

We begin by presenting a general description of the tight-binding model for a system with n atomic orbitals ϕ_j in the unit cell, labeled by index $j = 1, ..., n$. Further details may be found in the book by Saito, Dresselhaus, and Dresselhaus [82]. It is assumed that the system has translational invariance. Then, the model may be written using n different Bloch functions $\Phi_j(k, r)$ that depend on the position vector r and wave vector k. They are given by

$$\Phi_j(\mathbf{k},\mathbf{r}) = \frac{1}{\sqrt{N}} \sum_{i=1}^{N} e^{i\mathbf{k}.\mathbf{R}_{j,i}} \phi_j(\mathbf{r} - \mathbf{R}_{j,i}), \tag{2.3.1}$$

where the sum is over N different unit cells, labeled by index $i = 1...N$, and $R_{j,i}$ denotes the position of the j^{th} orbital in the i^{th} unit cell. In general, an electronic wave function $\Psi_j(k, r)$ is given by a linear superposition of the n different Bloch functions,

$$\Psi_j(\mathbf{k},\mathbf{r}) = \sum_{l=1}^{n} c_{j,l}(\mathbf{k}) \Phi_l(\mathbf{k},\mathbf{r}), \tag{2.3.2}$$

where $c_{j,l}$ are coefficients of the expansion. The energy $E_j(k)$ of the j_{th} band is given by

$$E_j(k) = \frac{\langle \Psi_j | H | \Psi_j \rangle}{\langle \Psi_j | \Psi_j \rangle}, \tag{2.3.3}$$

where H is the Hamiltonian. Substituting the expansion of the wave function (2.3.2) into the energy gives

$$E_j(k) = \frac{\sum_{i,l}^{n} c_{ji}^* c_{jl} \langle \Phi_i | H | \Phi_l \rangle}{\sum_{i,l}^{n} c_{ji}^* c_{jl} \langle \Phi_i | \Phi_l \rangle}, \tag{2.3.4}$$

$$= \frac{\sum_{i,l}^{n} H_{il} c_{ji}^* c_{jl}}{\sum_{i,l}^{n} S_{il} c_{ji}^* c_{jl}}, \tag{2.3.5}$$

where transfer integral matrix elements H_{il} and overlap integral matrix elements S_{il} are defined by

$$\begin{aligned} H_{il} &= \langle \Phi_i | H | \Phi_l \rangle, \\ S_{il} &= \langle \Phi_i | \Phi_l \rangle. \end{aligned} \tag{2.3.6}$$

We minimize the energy E_j with respect to the coefficient c_{jm}^* by calculating the derivative,

$$\frac{\partial E_j}{\partial c_{jm}^*} = \frac{\sum_{i,l}^{n} H_{ml} c_{jl}}{\sum_{i,l}^{n} S_{il} c_{ji}^* c_{jl}} - \frac{\sum_{i,l}^{n} H_{il} c_{ji}^* c_{jl} (\sum_{l}^{n} S_{ml} c_{jl})}{(\sum_{i,l}^{n} S_{il} c_{ji}^* c_{jl})^2}. \tag{2.3.7}$$

The second term contains a factor equal to the energy E_j itself, (2.3.5). Then, setting $\partial E_j / \partial c_{jm}^* = 0$ and omitting the common factor $\sum_{i,l}^{n} S_{il} c_{ji}^* c_{jl}$ gives

$$\sum_{l=1}^{n} H_{ml} c_{jl} = E_j \sum_{l=1}^{n} S_{ml} c_{jl}. \tag{2.3.8}$$

This can be written as a matrix equation. Consider the specific example of two orbitals per unit cell, $n = 2$. Then, we can select the possible values of m (either $m = 1$ or $m = 2$) and write out the summation in (2.3.8) explicitly:

$$m = 1 \Rightarrow H_{11} c_{j1} + H_{12} c_{j2} = E_j (S_{11} c_{j1} + S_{12} c_{j2}), \tag{2.3.9}$$

$$m = 2 \Rightarrow H_{21}c_{j1} + H_{22}c_{j2} = E_j(S_{21}c_{j1} + S_{22}c_{j2}). \tag{2.3.10}$$

These two equations may be combined into a matrix equation,

$$\begin{pmatrix} H_{11} & H_{12} \\ H_{21} & H_{22} \end{pmatrix} \begin{pmatrix} c_{j1} \\ c_{j2} \end{pmatrix} = \begin{pmatrix} S_{11} & S_{12} \\ S_{21} & S_{22} \end{pmatrix} \begin{pmatrix} c_{j1} \\ c_{j2} \end{pmatrix}. \tag{2.3.11}$$

For general values of n, defining H as the transfer integral matrix, S as the overlap integral matrix and ψ_j as a column vector,

$$H = \begin{pmatrix} H_{11} & H_{12} & \dots & H_{1n} \\ H_{21} & H_{22} & \dots & H_{2n} \\ \vdots & \vdots & \ddots & \vdots \\ H_{n1} & H_{n2} & \dots & H_{nn} \end{pmatrix}, \qquad S = \begin{pmatrix} S_{11} & S_{12} & \dots & S_{1n} \\ S_{21} & S_{22} & \dots & S_{2n} \\ \vdots & \vdots & \ddots & \vdots \\ S_{n1} & S_{n2} & \dots & S_{nn} \end{pmatrix}, \qquad \psi_j = \begin{pmatrix} c_{jl} \\ c_{j2} \\ \vdots \\ c_{jn} \end{pmatrix}, \tag{2.3.12}$$

allows the relation (2.3.8) to be expressed as

$$H\psi_j = E_j S\psi_j. \tag{2.3.13}$$

The energies E_j may be determined by solving the secular equation

$$det(H - E_j S) = 0, \tag{2.3.14}$$

once the transfer integral matrix H and the overlap integral matrix S are known. Here, *det* stands for the determinant of the matrix. In the following, we will omit the subscript $j = 1 \dots n$ in (2.3.13), (2.3.14), bearing in mind that the number of solutions is equal to the number of different atomic orbitals per unit cell.

2.4 The Tight-Binding Model of Monolayer Graphene

We apply the tight-binding model described in Section 2.3 to monolayer graphene, taking into account one $2p_z$ orbital per atomic site. As there are two atoms in the

unit cell of graphene, labeled A and B in Fig. 2.1, the model includes two Bloch functions, $n = 2$. For simplicity, we replace index $j = 1$ with $j = A$, and $j = 2$ with $j = B$. For monolayer graphene values of $n = 2$, the transfer integral matrix H_1, the overlap integral matrix S_1 and ψ_j as a column vector,

$$H_1 = \begin{pmatrix} H_{AA} & H_{AB} \\ H_{BA} & H_{BB} \end{pmatrix}, \qquad S_1 = \begin{pmatrix} S_{AA} & S_{AB} \\ S_{BA} & S_{BB} \end{pmatrix}, \qquad \psi_j = \begin{pmatrix} c_A \\ c_B \end{pmatrix}.$$

Now we proceed to determine the transfer integral matrix H_1 and the overlap integral matrix S_1.

2.4.1 Diagonal Matrix Elements

Substituting the expression for the Bloch function (2.3.1) into the definition of the transfer integral (2.3.6) allows us to write the diagonal matrix element corresponding to the A sublattice as

$$\begin{aligned} H_{AA} &= \langle \Phi_A | H | \Phi_A \rangle, \\ H_{AA} &= \frac{1}{N} \sum_{i=1}^{N} \sum_{j=1}^{N} e^{i\mathbf{k}\cdot(\mathbf{R}_{A,j} - \mathbf{R}_{A,i})} \langle \phi_A(\mathbf{r} - \mathbf{R}_{A,i}) | H | \phi_A(\mathbf{r} - \mathbf{R}_{A,j}) \rangle, \end{aligned} \tag{2.4.1}$$

where $\mathbf{k} = (k_x, k_y)$ is the wave vector in the graphene plane. Equation (2.4.1) includes a double summation over all the A sites of the lattice. If we assume that the dominant contribution arises from the same site $j = i$ within every unit cell, then:

$$H_{AA} \approx \frac{1}{N} \sum_{i=1}^{N} \langle \phi_A(\mathbf{r} - \mathbf{R}_{A,i}) | H | \phi_A(\mathbf{r} - \mathbf{R}_{A,i}) \rangle, \tag{2.4.2}$$

The matrix element $\langle \phi_A | H | \phi_A \rangle$ within the summation has the same value on every A site, i.e. it is independent of the site index i. We set it to be equal to a parameter

$$\epsilon_{2p} = \langle \phi_A(\mathbf{r} - \mathbf{R}_{A,i}) | H | \phi_A(\mathbf{r} - \mathbf{R}_{A,i}) \rangle, \tag{2.4.3}$$

that is equal to the energy of the $2p_z$ orbital. Then, keeping only the same site contribution,

$$H_{AA} \approx \frac{1}{N}\sum_{i=1}^{N} \epsilon_{2p} = \epsilon_{2p}. \tag{2.4.4}$$

It is possible to take into account the contribution of other terms in the double summation (2.4.1), such as next-nearest neighbor contributions [89, 90]. They generally have a small effect on the electronic band structure and will not be discussed here. The B sublattice has the same structure as the A sublattice, and the carbon atoms on the two sublattices are chemically identical. This means that the diagonal transfer integral matrix element corresponding to the B sublattice has the same value as that of the A sublattice:

$$H_{BB} = H_{AA} \approx \epsilon_{2p}. \tag{2.4.5}$$

A calculation of the diagonal elements of the overlap integral matrix proceeds in a similar way as for those of the transfer integral. In this case, the overlap between a $2p_z$ orbital on the same atom is equal to unity,

$$\langle \phi_A(\mathbf{r} - \mathbf{R}_{A,i}) | \phi_A(\mathbf{r} - \mathbf{R}_{A,i}) \rangle = 1. \tag{2.4.6}$$

Then, assuming that the same site contribution dominates,

$$S_{AA} = \frac{1}{N}\sum_{i=1}^{N}\sum_{j=1}^{N} e^{i\mathbf{k}\cdot(\mathbf{R}_{A,j} - \mathbf{R}_{A,i})} \langle \phi_A(\mathbf{r} - \mathbf{R}_{A,i}) | \phi_A(\mathbf{r} - \mathbf{R}_{A,j}) \rangle, \tag{2.4.7}$$

$$\approx \frac{1}{N}\sum_{i=1}^{N} \langle \phi_A(\mathbf{r} - \mathbf{R}_{A,i}) | \phi_A(\mathbf{r} - \mathbf{R}_{A,j}) \rangle, \tag{2.4.8}$$

$$= \frac{1}{N}\sum_{i=1}^{N} 1 = 1. \tag{2.4.9}$$

Again, as the B sublattice has the same structure as the A sublattice,

$$S_{BB} = S_{AA} = 1. \tag{2.4.10}$$

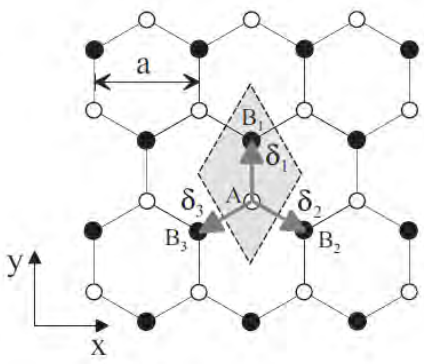

Figure 2.3: The honeycomb crystal structure of monolayer graphene. In the nearest-neighbor approximation, we consider hopping from an A site (white) to three adjacent B sites (black), labeled B_1, B_2, B_3, with position vectors $\delta_1, \delta_2, \delta_3$, respectively, relative to the A site.

2.4.2 Off-Diagonal Matrix Elements

Substituting the expression for the Bloch function (2.3.1) into the definition of the transfer integral (2.3.6) allows us to write an off-diagonal matrix element as

$$H_{AB} = \frac{1}{N} \sum_{i=1}^{N} \sum_{j=1}^{N} e^{i\mathbf{k}\cdot(\mathbf{R}_{B,j} - \mathbf{R}_{A,i})} \langle \phi_A(\mathbf{r} - \mathbf{R}_{A,i}) | H | \phi_B(\mathbf{r} - \mathbf{R}_{B,j}) \rangle. \tag{2.4.11}$$

It describes processes of hopping between the A and B sublattices, and contains a summation over all the A sites ($i = 1, ..., N$) at positions $\mathbf{R}_{A,i}$ and all the B sites ($j = 1, ..., N$) at $\mathbf{R}_{B,j}$.

In the following, we assume that the dominant contribution to the off-diagonal matrix element (2.4.12) arises from hopping between nearest neighbors only. If we

focus on an individual A atom, i.e. we consider a fixed value of the index i, we see that it has three neighboring B atoms, Fig. 2.3, that we will label with a new index l ($l = 1, 2, 3$). Each A atom has three such neighbors, so it is possible to write the nearest-neighbors contribution to the off-diagonal matrix element(2.4.12) as

$$H_{AB} \approx \frac{1}{N} \sum_{i=1}^{N} \sum_{l=1}^{3} e^{i\mathbf{k}\cdot(\mathbf{R}_{B,l} - \mathbf{R}_{A,i})} \langle \phi_A(\mathbf{r} - \mathbf{R}_{A,i}) | H | \phi_B(\mathbf{r} - \mathbf{R}_{B,l}) \rangle. \tag{2.4.12}$$

The matrix element between neighboring atoms, $\langle \phi_A | H | \phi_B \rangle$, has the same value for each neighboring pair, i.e. it is independent of indices i and l. We set it equal to a parameter, $t = \langle \phi_A(\mathbf{r} - \mathbf{R}_{A,i}) | H | \phi_B(\mathbf{r} - \mathbf{R}_{B,l}) \rangle$. Since t is negative [82], it is common practice to express it in terms of a positive parameter $\gamma_0 = -t$, where

$$\gamma_0 = -\langle \phi_A(\mathbf{r} - \mathbf{R}_{A,i}) | H | \phi_B(\mathbf{r} - \mathbf{R}_{B,l}) \rangle. \tag{2.4.13}$$

Then, we write the off-diagonal transfer integral matrix element as

$$H_{AB} \approx -\frac{1}{N} \sum_{i=1}^{N} \sum_{l=1}^{3} e^{i\mathbf{k}\cdot(\mathbf{R}_{B,l} - \mathbf{R}_{A,i})} \gamma_0, \tag{2.4.14}$$

$$H_{AB} = -\frac{\gamma_0}{N} \sum_{i=1}^{N} \sum_{l=1}^{3} e^{i\mathbf{k}\cdot\delta_l} = -\gamma_0 f(\mathbf{k}), \tag{2.4.15}$$

$$f(\mathbf{k}) = \sum_{l=1}^{3} e^{i\mathbf{k}\cdot\vec{\delta}_l}, \tag{2.4.16}$$

where the position vector of atom B_l relative to the A_i atom is denoted $\delta_l = \mathbf{R}_{B,l} - \mathbf{R}_{A,i}$, and we used the fact that the summation over the three neighboring B atoms is the same for all A_i atoms.

For the three B atoms shown in Fig. 2.3, the three vectors are

$$\vec{\delta}_1 = (0, \frac{a}{\sqrt{3}}), \qquad \vec{\delta}_2 = (\frac{a}{2}, -\frac{a}{2\sqrt{3}}), \qquad \vec{\delta}_3 = (-\frac{a}{2}, -\frac{a}{2\sqrt{3}}). \tag{2.4.17}$$

Note that $|\vec{\delta}_1| = |\vec{\delta}_2| = |\vec{\delta}_3| = a/\sqrt{3}$ is the carbon-carbon bond length. Then, the function $f(\mathbf{k})$ describing nearest-neighbor hopping may be evaluated as

$$f(\mathbf{k}) = \sum_{l=1}^{3} e^{i\mathbf{k}\cdot\vec{\delta}_l}, \tag{2.4.18}$$

$$= e^{ik_y a/\sqrt{3}} + e^{ik_x a/2} e^{-ik_y a/2\sqrt{3}} + e^{-ik_x a/2} e^{-ik_y a/2\sqrt{3}}, \tag{2.4.19}$$

$$= e^{ik_y a/\sqrt{3}} + 2e^{-ik_y a/2\sqrt{3}} \cos(k_x a/2), \tag{2.4.20}$$

The other off-diagonal matrix element H_{BA} is the complex conjugate of H_{AB}:

$$H_{AB} \approx -\gamma_0 f(\mathbf{k}), H_{BA} \approx -\gamma_0 f^*(\mathbf{k}). \tag{2.4.21}$$

A calculation of an off-diagonal element of the overlap integral matrix proceeds in a similar way as for the transfer integral:

$$S_{AB} = \frac{1}{N} \sum_{i=1}^{N} \sum_{j=1}^{N} e^{i\mathbf{k}\cdot(\mathbf{R}_{B,j} - \mathbf{R}_{A,i})} \langle \phi_A(\mathbf{r} - \mathbf{R}_{A,i}) | \phi_B(\mathbf{r} - \mathbf{R}_{B,j}) \rangle, \tag{2.4.22}$$

$$S_{AB} \approx \frac{1}{N} \sum_{i=1}^{N} \sum_{l=1}^{3} e^{i\mathbf{k}\cdot(\mathbf{R}_{B,l} - \mathbf{R}_{A,i})} \langle \phi_A(\mathbf{r} - \mathbf{R}_{A,i}) | \phi_B(\mathbf{r} - \mathbf{R}_{B,l}) \rangle, \tag{2.4.23}$$

$$= -s_0 f(\mathbf{k}), \tag{2.4.24}$$

where the parameter $s_0 = \langle \phi_A(\mathbf{r} - \mathbf{R}_{A,i}) | \phi_B(\mathbf{r} - \mathbf{R}_{B,l}) \rangle$, and $S_{BA} = S_{AB}^* = -s_0 f(\mathbf{k})$. The presence of non-zero s_0 takes into account the possibility that orbitals on adjacent atomic sites are not strictly orthogonal.

2.4.3 The Low-energy Electronic Bands of Monolayer Graphene

Summarizing the results of this section, the transfer integral matrix elements (2.4.5) and (2.4.22), and the overlap integral matrix elements (2.4.11) and (2.4.25) give

$$H_1 = \begin{pmatrix} \epsilon_{2p} & -\gamma_0 f(\mathbf{k}) \\ -\gamma_0 f^*(\mathbf{k}) & \epsilon_{2p} \end{pmatrix}, S_1 = \begin{pmatrix} 1 & s_0 f(\mathbf{k}) \\ s_0 f^*(\mathbf{k}) & 1 \end{pmatrix}, \tag{2.4.25}$$

where we use the subscript 1 to stress that these matrices apply to monolayer graphene. The corresponding energy E may be determined by solving the secular equation $det(H_1 - ES_1) = 0$,

$$det \begin{pmatrix} \epsilon_{2p} - E & -(\gamma_0 + Es_0) f(\mathbf{k}) \\ -(\gamma_0 + Es_0) f^*(\mathbf{k}) & \epsilon_{2p} - E \end{pmatrix} = 0, \tag{2.4.26}$$

$$\Rightarrow (E - \epsilon_{2p})^2 - ([E - \epsilon_{2p}]s_0 + \epsilon_{2p}s_0 + \gamma_0)^2 |f(\mathbf{k}|^2 = 0. \tag{2.4.27}$$

Solving this quadratic equation yields the energy:

$$E_\pm = \frac{\epsilon_{2p} \pm \gamma_0 |f(\mathbf{k})|}{1 \mp s_0 |f(\mathbf{k})|} \tag{2.4.28}$$

This expression appears in Saito et al [82], where parameter values $\gamma_0 = 3.033eV$, $s_0 = 0.129$, $\epsilon_{2p} = 0$ are quoted. The latter value ($\epsilon_{2p} = 0$) means that the zero of energy is set to be equal to the energy of the $2p_z$ orbital. The resulting band structure $E_\pm$ is shown in Fig. 2.4 in the vicinity of the Brillouin zone. A particular cut through the band structure is shown in Fig. 2.5 where the bands are plotted as a function of wave vector component k_x along the line $k_y = 0$, a line that passes through the center of the Brillouin zone, labeled Γ, and two corners of the Brillouin zone, labeled K_+ and K_- (see the inset of Fig. 2.5). The Fermi level in pristine graphene is located at zero energy. There are two energy bands, that we refer to as the conduction band

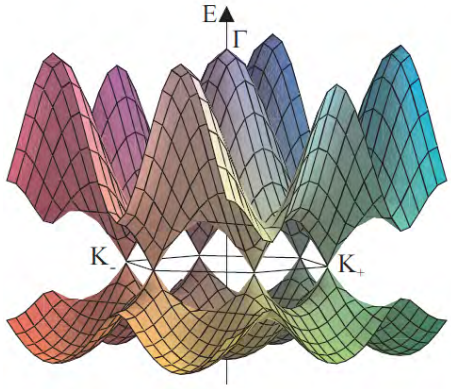

Figure 2.4: The low-energy band structure of monolayer graphene Eq. (2.4.29) taking into account nearest-neighbor hopping with parameter $\gamma_0 = 3.033eV$, nearestneighbor overlap parameter $s_0 = 0.129$, and orbital energy $\epsilon_{2p} = 0$ [82]. The plot shows the bands calculated in the vicinity of the first Brillouin zone, with conduction and valence bands touching at six corners of the Brillouin zone, two of them are labeled K_+ and K_- . Label Γ indicates the center of the Brillouin zone.

(E_+) and the valence band (E_-). The interesting feature of the band structure is that there is no band gap between the conduction and valence bands. Instead the bands cross at the six corners of the Brillouin zone, Fig. 2.4. The corners of the Brillouin zone are known as K points, and two of them are explicitly labeled K_+ and K_- in Fig. 2.4. Near these points, the dispersion is linear and electronic properties may be described by a Dirac-like Hamiltonian. This will be explored in more detail in the next section. Note also that the band structure displays a large asymmetry between the conduction and valence bands that is most pronounced in the vicinity of the Γ point. This arises from the non-zero overlap parameter s_0 appearing in (2.4.29).

The tight-binding model described here cannot be used to determine the values of parameters such as Γ and s_0. They must be determined either by an alternative theoretical method, such as density-functional theory, or by comparison of the tight-binding model with experiments. Note, however, that the main qualitative features

described in this chapter do not depend on the precise values of the parameters quoted.

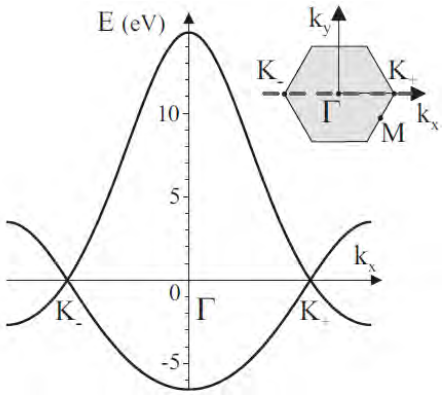

Figure 2.5: The low-energy band structure of monolayer graphene Eq. (2.4.29) taking into account nearest-neighbor hopping with parameter $\gamma_0 = 3.033eV$, nearestneighbor overlap parameter $s_0 = 0.129$, and orbital energy $\epsilon_{2p} = 0$ [82]. The plot shows a cut through the band structure Fig. 2.4, plotted along the k_x axis intersecting points K_-, γ, and K_+ in the Brillouin zone, shown as the dotted line in the inset.

2.5 Massless Dirac Fermions in Monolayer Graphene

2.5.1 The Dirac-like Hamiltonian

As described in the previous section, the electronic band structure of monolayer graphene, Figs. 2.4, 2.5, is gapless, with crossing of the bands at points K_+ and K_- located at corners of the Brillouin zone. In this section, we show that electronic properties near these points may be described by a Dirac-like Hamiltonian.

Although the first Brillouin zone has six corners, only two of them are non-equivalent. In this Chapter, we choose points K_+ and K_-, Figs. 2.4, 2.5, as a non-equivalent pair. It is possible to connect two of the other corners to K_+ using a

reciprocal lattice vector (hence, the other two are equivalent to K_+), and it is possible to connect the remaining two corners to K_- using a reciprocal lattice vector (hence, the remaining two are equivalent to K_-), but it is not possible to connect K_+ and K_- with a reciprocal lattice vector. To distinguish between K_+ and K_-, we will use an index $\xi = \pm 1$. Using the values of the primitive reciprocal lattice vectors b_1 and b_2, (2.2.2), it can be seen that the wave vector corresponding to point K_ξ is given by

$$K_\xi = \xi \left(\frac{4\pi}{3a}, 0 \right). \tag{2.5.1}$$

Note that the K points are often called valleys using nomenclature from semiconductor physics.

In the tight-binding model, coupling between the A and B sublattices is described by the off-diagonal matrix element H_{AB}, (2.4.22), that is proportional to parameter γ_0 and the function $f(k)$, (2.4.19). Exactly at the K_ξ point, $k = K_\xi$, the latter is equal to

$$f(K_\xi) = e^0 + e^{i\xi 2\pi/3} + e^{-i\xi 2\pi/3} = 0. \tag{2.5.2}$$

This indicates that there is no coupling between the A and B sublattices exactly at the K_ξ point. Since the two sublattices are both hexagonal Bravais lattices of carbon atoms, they support the same quantum states, leading to a degeneracy point in the spectrum at K_ξ, Figs. 2.4, 2.5.

The exact cancelation of the three factors describing coupling between the A and B sublattices, (2.4.31), no longer holds when the wave vector is not exactly equal to that of the K_ξ point. We introduce a momentum $\mathbf{p}$ that is measured from the center of the K_ξ point,

$$\mathbf{p} = \hbar k - \hbar K_\xi. \tag{2.5.3}$$

Then, the coupling between the A and B sublattices is proportional to

$$f(k) = e^{ip_y a/\sqrt{3}\hbar} + e^{-ip_y a/2\sqrt{3}\hbar} \cos\left(\frac{2\pi\xi}{3} + \frac{p_x a}{2\hbar}\right), \tag{2.5.4}$$

$$\approx \left(1 + \frac{ip_y a}{\sqrt{3}\hbar}\right) + 2\left(1 - \frac{ip_y a}{2\sqrt{3}\hbar}\right)\left(-\frac{1}{2} - \frac{\xi\sqrt{3}p_x a}{4\hbar}\right), \tag{2.5.5}$$

$$\approx -\frac{\sqrt{3}a}{2\hbar}(\xi p_x - ip_y), \tag{2.5.6}$$

where we kept only linear terms in the momentum $\mathbf{p} = (p_x, p_y)$, an approximation that is valid close to the K_ξ point, i.e. for $pa/\hbar << 1$, where $p = |\mathbf{p}| = (p_x^2 + p_y^2)^{1/2}$. Using this approximate expression for the function $f(k)$, the transfer integral matrix (2.4.26) in the vicinity of point K_ξ becomes

$$H_{1,\xi} = \nu_F \begin{pmatrix} 0 & \xi p_x - ip_y \\ \xi p_x + ip_y & 0 \end{pmatrix} \tag{2.5.7}$$

Here, we used $\epsilon_{2p} = 0$ [82] which defines the zero of the energy axis to coincide with the energy of the $2p_z$ orbital. The parameters a and γ_0 were combined into a velocity v_F defined as $v_F = \sqrt{3}a\gamma_0/2\hbar$.

Within the linear-in-momentum approximation for $f(k)$, (2.4.35), the overlap matrix S_1 may be regarded as a unit matrix, because its off-diagonal elements, proportional to s_0, only contribute quadratic-in-momentum terms to the energy $E_\pm$, (2.4.29). Since S_1 is approximately equal to a unit matrix, (2.3.13) becomes $H_1\psi = E\psi$, indicating that H_1, (2.5.7), is an effective Hamiltonian for monolayer graphene at low-energy. The energy eigenvalues and eigenstates of H_1 are given by(see Appendix A)

$$E_{\pm} = \pm\nu_F p, \qquad \psi_{\pm} = \frac{1}{\sqrt{2}} \begin{pmatrix} 1 \\ \pm\xi e^{i\xi\varphi} \end{pmatrix} e^{i\mathbf{p}\cdot\mathbf{r}/\hbar}, \tag{2.5.8}$$

where $\pm$ refer to the conduction and valence bands, respectively. Here φ is the polar angle of the momentum in the graphene plane, $\mathbf{p} = (p_x, p_y) = p(\cos\varphi, \sin\varphi)$.

2.6 The Tight-Binding Model of Bilayer Graphene

In this section, we describe the tight-binding model of bilayer graphene. To do so, we use the tight-binding model described in Sect.2.3 in order to generalize the model for monolayer graphene discussed in Sect.2.4.

We consider Bernal-stacked bilayer graphene [37, 91, 92] (also called AB stacked bilayer graphene). It consists of two parallel layers of carbon atoms, each arranged with a honeycomb arrangement as in a monolayer, that are coupled together, Fig. 2.6. There are four atoms in the unit cell, a pair A1, B1, from the lower layer and a pair A2, B2, from the upper layer. In Bernal stacking, the layers are arranged so that two atoms, B1 and A2, are directly below or above each other, whereas the other two atoms, A1 and B2, do not have a counterpart in the other layer. The primitive lattice vectors a_1 and a_2, and the lattice constant a are the same as for monolayer graphene, and the unit cell, shown in Fig. 2.6(a), has the same area in the x-y plane as in the monolayer. Therefore, the reciprocal lattice and first Brillouin zone are the same as in monolayer graphene, Fig. 2.2. The unit cell of bilayer graphene contains four atoms, and, if the tight-binding model includes one p_z orbital per atomic site, there will be four bands near zero energy, instead of the two bands in monolayer graphene.

Essential features of the low-energy electronic band structure may be described

by a minimal tight-binding model including nearest-neighbor coupling γ_0 between A1 and B1, and A2 and B2, atoms on each layer, and nearest neighbor interlayer coupling γ_1 between B1 and A2 atoms that are directly below or above each other,

$$\gamma_1 = \langle \phi_{A2}(\mathbf{r} - \mathbf{R}_{A2}) | H | \phi_{B1}(\mathbf{r} - \mathbf{R}_{B1}) \rangle. \tag{2.6.1}$$

Then, we can generalize the treatment of monolayer graphene, (2.4.26), to write the transfer and overlap integral matrices of bilayer graphene, in a basis with components A1, B1, A2, B2, as

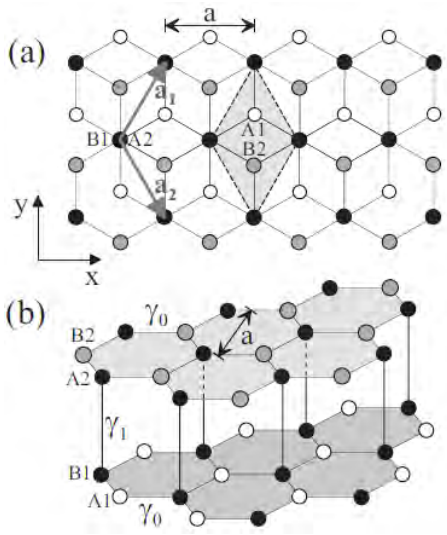

Figure 2.6: Schematic representation of the crystal structure of AB-stacked bilayer graphene: (a) plan view with A1 (white) and B1 atoms (black) on the lower layer, A2 (black) and B2 atoms (grey) on the upper layer. Vectors a_1 and a_2 are primitive lattice vectors of length equal to the lattice constant a, and the shaded rhombus is a unit cell; (b) side view where the parameter γ_0 represents nearest-neighbor coupling within each layer, γ_1 nearest-neighbor coupling between the B1 and A2 atoms on different layers [91].

$$H = \begin{pmatrix} \epsilon_{2p} & -\gamma_0 f(\mathbf{k}) & 0 & 0 \\ -\gamma_0 f^*(\mathbf{k}) & \epsilon_{2p} & \gamma_1 & 0 \\ 0 & \gamma_1 & \epsilon_{2p} & -\gamma_0 f(\mathbf{k}) \\ 0 & 0 & -\gamma_0 f^*(\mathbf{k}) & \epsilon_{2p} \end{pmatrix}, \tag{2.6.2}$$

$$S = \begin{pmatrix} 1 & s_0 f(\mathbf{k}) & 0 & 0 \\ s_0 f^*(\mathbf{k}) & 1 & 0 & 0 \\ 0 & 0 & 1 & s_0 f(\mathbf{k}) \\ 0 & 0 & s_0 f^*(\mathbf{k}) & 1 \end{pmatrix}. \tag{2.6.3}$$

The upper-left and lower-right 2×2 blocks describe behavior within the lower (A1/B1) and upper (A2/B2) layers, respectively. The off-diagonal 2×2 blocks, containing parameter γ_1, describe interlayer coupling. The band structure of bilayer graphene may

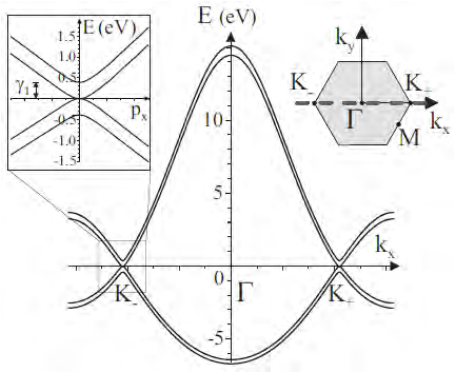

Figure 2.7: The low-energy band structure of bilayer graphene taking into account nearest-neighbor hopping with parameter $\gamma_0 = 3.033eV$, nearest-neighbor overlap parameter $s_0 = 0.129$, orbital energy $\epsilon_{2p} = 0$ [11], and interlayer coupling $\gamma_1 = 0.39eV$. The plot shows the bands calculated along the k_x axis intersecting points K_-, Γ, and K_+ in the Brillouin zone, shown as the dotted line in the right inset. The left inset shows the band structure in the vicinity of the point K_-.

be determined by solving the secular equation $\det(H - E_j S) = 0$, (2.3.14). It is plotted in Fig. 2.7 for parameter values $\gamma_0 = 3.033eV$, $s_0 = 0.129$, $\epsilon_{2p} = 0$ [82] and interlayer coupling $\gamma_1 = 0.39eV$. There are four energy bands, two conduction bands

and two valence bands. Overall, the band structure is similar to that of monolayer graphene, Fig. 2.5, with each monolayer band split into two by an energy approximately equal to the interlayer coupling γ_1[92]. The most interesting part of the band structure is in the vicinity of the K points [91], as shown in the left inset of Fig. 2.7 which focuses in on the bands around K_-. At the K point, one of the conduction (valence) bands is split away from zero energy by an amount equal to the interlayer coupling $\gamma_1(-\gamma_1)$. The split bands originate from atomic sites B1 and A2 that have a counterpart atom directly above or below them on the other layer. Orbitals on these pairs of atoms (B1 and A2) are strongly coupled by the interlayer coupling γ_1 and they form a bonding and anti-bonding pair of bands, split away from zero energy. In the following, we refer to them as dimer states, and atomic sites B1 and A2 are called dimer sites. The remaining two bands, one conduction and one valence band, touch at zero energy: as in the monolayer, there is no band gap between the conduction and valence bands. In the vicinity of the K points, the dispersion of the latter bands is quadratic $E_\pm \propto \pm|k - K_\xi|^2$, and electronic properties of the low-energy bands may be described by an effective Hamiltonian describing massive chiral particles. This will be explored in more detail in the next section.

2.6.1 The Low-energy Bands of Bilayer Graphene

To begin the description of the low-energy bands in bilayer graphene, we set $s_0 = 0$, thus neglecting the non-orthogonality of orbitals that tends to become important at high energy. Then, the overlap matrix S, (2.6.3), becomes a unit matrix, and H, (2.6.2), is an effective Hamiltonian for the four bands of bilayer graphene at low-energy [91]:

$$H = \begin{pmatrix} 0 & -\gamma_0 f(\mathbf{k}) & 0 & 0 \\ -\gamma_0 f^*(\mathbf{k}) & 0 & \gamma_1 & 0 \\ 0 & \gamma_1 & 0 & -\gamma_0 f(\mathbf{k}) \\ 0 & 0 & -\gamma_0 f^*(\mathbf{k}) & 0 \end{pmatrix}, \tag{2.6.4}$$

where we used $\epsilon_{2p} = 0$ [82] to define the zero of the energy axis to coincide with the energy of the $2p_z$ orbital. Eigenvalues of the Hamiltonian are given by

$$E_{\pm}^{(\alpha)} = \pm\frac{\gamma_1}{2}\left(\sqrt{1 + \frac{4\gamma_0^2|f(\mathbf{k})|^2}{\gamma_1^2}} + \alpha\right), \alpha = \pm 1. \tag{2.6.5}$$

Over most of the Brillouin zone, where $4\gamma_0^2|f(k)|^2 >> \gamma_1^2$, the energy may be approximated as $E_{\pm}^{(\alpha)} \approx \pm(\gamma_0|f(\mathbf{k})| + \alpha\gamma_1/2)$, meaning that the $\alpha = \pm 1$ bands are approximately the same as the monolayer bands, (2.4.29), but they are split by the interlayer coupling γ_1. The eigenvalues $E_{\pm}^{1}$, (2.6.5), describe two bands that are split away from zero energy by $\pm\gamma_1$ at the K point (where $|f(\mathbf{k})| = 0$) as shown in the left inset of Fig. 2.7. This is because the orbitals on the A2 and B1 sites form a dimer that is coupled by interlayer hopping γ_1, resulting in a bonding and anti-bonding pair of states $\pm\gamma_1$.

The remaining two bands are described by $E_{\pm}^{-1}$. Near to the K_ξ point, $pa/\hbar << 1$, we replace the factor $\gamma_0|f(k)|$ with $\nu_F p$, (2.4.35):

$$E_{\pm}^{(-1)} \approx \pm\frac{\gamma_1}{2}\left(\sqrt{1 + \frac{4\nu_F^2 p^2}{\gamma_1^2}} - 1\right), \alpha = \pm 1. \tag{2.6.6}$$

This formula interpolates between linear dispersion at large momenta ($\gamma_1 << \nu_F p < \gamma_0$) and quadratic dispersion $E_{\pm}^{(-1)} \approx \pm\nu_F^2 p^2/\gamma_1$ near zero energy where the bands touch. These bands arise from effective coupling between the orbitals on sites, A1 and B2, that do not have a counterpart in the other layer. In the absence of direct

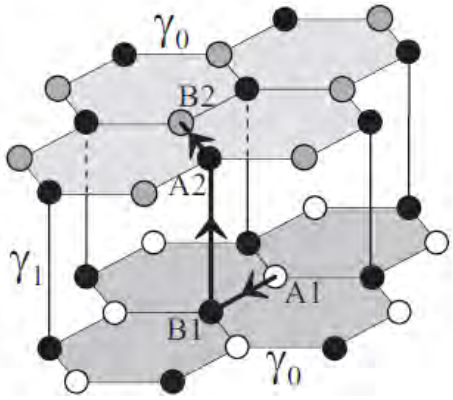

Figure 2.8: Schematic representation of the crystal structure of AB-stacked bilayer graphene illustrating the processes that contribute to effective coupling between A1 (white) and B2 atoms (grey), in the presence of strongly-coupled dimer sites B1 and A2 (black). The black arrowed line indicates the three stage process: intralayer hopping between A1 and B1, followed by an interlayer transition via the dimer sites B1 and A2, followed by another intralayer hopping between A2 and B2.

coupling between A1 and B2, the effective coupling is achieved through a three stage process as indicated in Fig. 2.8. It can be viewed as an intralayer hopping between A1 and B1, followed by an interlayer transition via the dimer sites B1 and A2, followed by another intralayer hopping between A2 and B2. This effective coupling may be described by an effective low-energy Hamiltonian written in a two-component basis of p_z orbitals on A1 and B2 sites.

2.6.2 The Two-Component Hamiltonian of Bilayer Graphene

The effective two-component Hamiltonian may be derived from the four component Hamiltonian, (2.6.4), [91, 93]. In the present context, a straightforward way to do the transformation is to consider the eigenvalue equation for the four component Hamiltonian, (2.6.4), as four simultaneous equations for the wave-function components

$c_{A1}, c_{B1}, c_{A2}, c_{B2}$:

$$Ec_{A1} + \gamma_0 f(\mathbf{k}) c_{B1} = 0, \tag{2.6.7}$$

$$\gamma_0 f^*(\mathbf{k}) c_{A1} + Ec_{B1} - \gamma_1 c_{A2} = 0, \tag{2.6.8}$$

$$\gamma_1 c_{B1} + Ec_{A2} + \gamma_0 f(\mathbf{k}) c_{B2} = 0, \tag{2.6.9}$$

$$\gamma_0 f^*(\mathbf{k}) c_{A2} + Ec_{B2} = 0. \tag{2.6.10}$$

Using the second and third equations, (2.6.8) and (2.6.9), it is possible to express the components on the dimer sites, c_{B1} and c_{A2}, in terms of the other two:

$$c_{B1} = \frac{\gamma_0 f(\mathbf{k})}{\gamma_1 d} c_{B2} + \frac{E\gamma_0 f^*(\mathbf{k})}{\gamma_1^2 d} c_{A1}, \tag{2.6.11}$$

$$c_{A2} = \frac{\gamma_0 f(\mathbf{k})}{\gamma_1^2 d} c_{B2} + \frac{E\gamma_0 f^*(\mathbf{k})}{\gamma_1 d} c_{A1}, \tag{2.6.12}$$

where $d = 1 - E^2/\gamma_1^2$. Substituting these expressions into the first and fourth equations, (2.6.7) and (2.6.10), produces two equations solely in terms of c_{A1} and c_{B2}. Assuming $|E| << |\gamma_1|$ and $|\gamma_0 f(\mathbf{k})| << |\gamma_1|$, we use $d \approx 1$ and keep terms up to order $1/\gamma_1$ only:

$$Ec_{A1} + \frac{\gamma_0^2 f^2(\mathbf{k})}{\gamma_1} c_{B2} = 0, \tag{2.6.13}$$

$$\frac{\gamma_0^2 (f^*(\mathbf{k}))^2}{\gamma_1} c_{A1} + Ec_{B2} + = 0. \tag{2.6.14}$$

It is possible to express these two equations as a Schrodinger equation, $H_2\psi = E\psi$, with a two-component wave function $\psi = (c_{A1}, c_{B2})^T$ and two-component Hamiltonian

$$H_{2,\xi} = -\frac{1}{2m} \begin{pmatrix} 0 & (\xi p_x - i p_y)^2 \\ (\xi p_x + i p_y)^2 & 0 \end{pmatrix}, \tag{2.6.15}$$

where we used the approximation $f(\mathbf{k}) \approx -\nu_F(\xi p_x - i p_y)/\gamma_0$, (2.5.6), valid for momentum $pa/\hbar << 1$ close to the K point, and parameters ν_F and γ_1 were combined into a mass $m = \gamma_1/(2\nu_F^2)$.

The effective low-energy Hamiltonian of bilayer graphene, (2.6.15), resembles the Dirac-like Hamiltonian of monolayer graphene, (2.5.7), but with a quadratic term on the off-diagonal instead of linear. The energy eigenvalues and eigenstates of H_2 are given by

$$E_{\pm} = \pm\frac{p^2}{2m}, \qquad \psi_{\pm} = \frac{1}{\sqrt{2}} \begin{pmatrix} 1 \\ \mp e^{i2\xi\varphi} \end{pmatrix} e^{i\mathbf{p}\cdot\mathbf{r}/\hbar}, \tag{2.6.16}$$

where $\pm$ refer to the conduction and valence bands, respectively. Here φ is the polar angle of the momentum in the graphene plane, $\mathbf{p} = (p_x, p_y) = p(\cos\varphi, \sin\varphi)$.

2.7 Transport Parameters in pristine Graphene

2.7.1 Electron Velocity

Let us calculate quantum mechanical average electron velocity. It is natural that for a quantum particle the average velocity is just the group velocity of the wave package representing quantum particle [95]. To find an expression for the electron velocity vector $\vec{v}(\vec{k})$ and its magnitude, we drive the equation of motion of an electron in an energy band. And we look at the motion of a wave packet in applied electric field [96]. Suppose that the wave packet is made up of a wavefunctions near a particular wave vector k. The group velocity is

$$\vec{v} = \frac{1}{\hbar}\frac{\partial E}{\partial k} = v_F \frac{\vec{k}}{|\vec{k}|}. \tag{2.7.1}$$

In this part, we can see that $|\vec{v}(\vec{k})| = v_F = 10^8 cm/s$ for all electrons in graphene is the same and equals v_F irrespective of the wave vector [97, 98]. So all electrons in graphene always move with the same speed. Therefore, an externally applied field can never change the speed of the carriers. In response to an electric field the electrons

in graphene change their direction of motion (but not their speed). This is also why the electrons that had a larger component of their initial velocity perpendicular to the electric field contributed the most to the conductivity.

2.7.2 Electronic Density of States

The electronic density of states $g(E)$ counts the number of quantum states in the vicinity of a fixed energy E. It turns out to be a very useful quantity when discussing the electric transport in the diffusive regime. It may be obtained from the total number of states below the energy E. Let we have $L \times L$ graphene sheets, then we have $4(L/2\pi)^2$ density of states in the reciprocal space. Therefore, the total number of states can be given by [25]

$$N = g\frac{L^2}{(2\pi)^2}\int_0^k dk_x dk_y, \tag{2.7.2}$$

and include contributions from all valleys (pockets) and spin. The factor g takes into account the degeneracy due to internal degrees of freedom g = 4 in the case of graphene because of the two fold valley degeneracy and the electron spin. Again the above equation can be written in polar coordinates as follows:

$$N = 4\frac{L^2}{(2\pi)^2}\int_0^k 2\pi k dk = \frac{2L^2}{\pi}\int_0^k k dk. \tag{2.7.3}$$

The calculation of the density of states may be rather involved because one needs to calculate a 2D integral over the wave vector as a function of energy, by inverting the energy dispersion. In the vicinity of the Dirac points, however, it may be calculated

quite easily because of the isotropy of the linear energy dispersion.

$$\begin{aligned} E &= \hbar v_F k, \\ k &= \frac{E}{\hbar v_F}, \\ dk &= \frac{dE}{\hbar v_F}. \end{aligned} \tag{2.7.4}$$

Thus the density of states per unit energy $g(E)dE$ of graphene can be found as follows. One may identify substituting the non parabolic dispersion of energy

$$g(E)dE = 4A\frac{2\pi k dk}{(2\pi)^2} = \frac{2A|E|dE}{\pi\hbar^2 v_F^2} \tag{2.7.5}$$

from which the density of states is

$$g(E \geq 0) = \frac{2A}{\pi(\hbar v_F)^2}E. \tag{2.7.6}$$

and for the full (positive and negative) energy range [25]

$$g(E) = \frac{2A}{\pi(\hbar v_F)^2}|E|. \tag{2.7.7}$$

The density of states, therefore, vanishes linearly at the Dirac points, at zero energy. This is a direct consequence of the linearity of the energy dispersion in the vicinity of the Dirac points. This particular situation needs to be contrasted to the conventional case of electrons in 2D metals, with an energy dispersion of $E = \hbar^2 k^2/2m^*$, in terms of the band mass m^*, where one obtains a constant density of states, $g(E)^{2D}(E) = gm^*/2\pi\hbar^2$. The density of states of graphene is linear with energy unlike other two dimensional semiconductor materials, which makes graphene unique two dimensional system.

2.7.3 Electrical Conductivity

Now suppose an electric field $\vec{E}$ is applied to graphene. The scattering time is τ. We need to find an expression for the current density $\vec{j}$. In general, the current density

for non-parabolic bands is not linearly related to the electric field $\vec{E}$. However, for small electric fields one can keep the terms that are of first order in the electric field. In this small-field limit, we can say that that:

$$j = \sigma \vec{E}. \tag{2.7.8}$$

The dynamical equation for the crystal momentum holds. Also we include contributions from all valleys and spin. The current density can be written as

$$\vec{j} = 2 \times 2 \times A \int_0^\infty \frac{d^2k}{(2\pi)^2} f(\vec{k} + e\tau\vec{E}/\hbar)\vec{v}(\vec{k}), \tag{2.7.9}$$

let $\vec{q} = \vec{k} + e\tau\vec{E}/\hbar$, and then substituting this in the above expression, we get:

$$\vec{j} = \frac{e^2\tau}{\pi\hbar^2} \int_0^\infty \frac{d^2q}{(2\pi)^2} f(q) v_F \frac{\vec{q} - e\tau\vec{E}/\hbar}{|\vec{q} - e\tau\vec{E}/\hbar|}, \tag{2.7.10}$$

and also remember that the velocity vector defined in (Equation 2.7.1) used here. After Taylor expansion select and keep terms that are of first order in the electric field. The current density will be

$$j_x = \frac{e^2\tau}{\pi\hbar^2} \int_0^\infty d\varepsilon f(\varepsilon - \varepsilon_F) E_x. \tag{2.7.11}$$

From which the conductivity will be

$$\sigma = \frac{e^2\tau}{\pi\hbar^2} \int_0^\infty d\varepsilon f(\varepsilon - \varepsilon_F), \tag{2.7.12}$$

we can say that the conductivity in graphene is not directly proportional to the electron density as is the case in most other semiconductors that have parabolic energy dispersions near the band edges.

2.7.4 Electrical Resistivity

The universal resistance of graphene was predicted in 1986 by Eduardo Fradkin and observed experimentally by Geim and collaborators in 2005. However, the value of the resistivity was about 20 percent less than the theoretical prediction. This result remains a mystery, although Geim has suggested that it may be due to electrons being scattered by ripples in the surface of the graphene sheet itself.

Resistivity of the graphene sheet $\sim 10^{-6}\Omega \cdot cm$, less than the resistivity of silver (Ag), the lowest resistivity substance known at room temperature.

2.7.5 Electrical Mobility

In solid-state physics, the electron mobility characterizes how quickly an electron can move through a metal or semiconductor, when pulled by an electric field. In semiconductors, there is an analogous quantity for holes, called hole mobility. The term carrier mobility refers in general to both electron and hole mobility in semiconductors. Electron and hole mobility are special cases of electrical mobility of charged particles in a fluid under an applied electric field. When an electric field is applied across a piece of material, the electrons respond by moving with an average velocity called the drift velocity, v_d, Electron mobility is almost always specified in units of $cm^2/(Vs)$. Mobility is usually a strong function of material impurities and temperature. The electron mobility, μ defined by the equation

$$\mu = \frac{v_d}{E}. \tag{2.7.13}$$

The band structure of graphene differs from that of a typical semiconductor in the following points:

(1) at around the point where the conduction band and the valence band meet each other, the slope of the band structure is linear ;
(2) the conduction band is connected continuously with the valence band, which means the band gap is zero.

With respect to characteristic (1) of the band structure, in the case of a typical semiconductor, the band structure at around the top of the valence band and the bottom of the conduction band shows a parabolic shape and the slope changes gradually. The larger the change of the slope of the band, the less the effective-mass of the electrons (virtual mass of electrons in a material). On the other hand, in the case of graphene, because the slope is linear, the effective mass of electrons is zero. This means that graphene shows very high electron-mobility. A theoretical expectation of the electron-mobility of graphene is 1,000 times higher than that of silicon, and an electron mobility as high as $2 \times 10^5 cm^2/Vsec$[Bolotin,10,11] has been experimentally achieved, which is 100 times higher than that of silicon. Because higher electron mobility leads to shorter switching time for a transistor, graphene has been expected as a material that could realize high-speed electronic devices which could break the speed records made by conventional semiconductors such as silicon or compound semiconductors. For that reason, graphene has been expected to be applied to high speed-transistors. In addition, graphene has been paid much attention as a target of physics because the zero effective mass in graphene is a special quantum mechanical phenomenon[9,12].

On the other hand, the zero bandgap in graphene, mentioned in (2), means that a

very small thermal energy excites electrons out of the valence band up to the conduction band. Therefore, graphene cannot be kept semi-insulating. Therefore, the zero bandgap of graphene is a very high hurdle for application to digital transistors. Several methods are proposed to open the bandgap of graphene, and some experiments have been reported to succeed to tune the bandgap. Generally speaking, the wider bandgap of graphene is achievable by deforming, more or less, the band structure, and may therefore easily result in diminishing the advantage of high electron mobility. In this respect, it is a big challenge for the technology development of graphene, to make the bandgap wider without diminishing the high electron mobility.

At the same time, there is strong evidence that graphene is a nearly perfect crystal free of the structural defects [4,5] that characterize most conductors. As a result, it has been put forth that the scattering of charge carriers stems from extrinsic sources [6,11]. Although the exact nature of the scattering that limits the mobility of graphene devices remains unclear, evidence has mounted that interactions with the underlying substrate are largely responsible. Surface charge traps [69], interfacial phonons [11], substrate stabilized ripples [5,10,12], and fabrication residues on or under the graphene sheet may all contribute. Consequently, improving substrate quality or eliminating the substrate altogether by suspending graphene seems a promising strategy towards higher quality samples. While devices suspended over the substrate were achieved in the past [12], they lacked multiple electrical contacts thus difficult for transport measurements.

In the recent paper [11] report the fabrication of electrically contacted suspended graphene and achieve a tenfold improvement in mobility as compared to the best values reported in the literature for traditional devices fabricated on a substrate.

Besides opening new avenues for studying the intrinsic physics of Dirac fermions, this improvement demonstrates the dominant role played by extrinsic scattering in limiting the transport properties of unsuspended graphene samples.

2.8 Graphene in a uniform magnetic field

When a perpendicular magnetic field is applied a two-dimensional electron gas, the electrons follow cyclotron orbits, and their allowed energies are quantized into values known as Landau levels [101]. At higher magnetic fields, the discrete Landau level spectrum is manifest in the integer quantum Hall effect [102, 103, 104], a quantization of Hall conductivity into integer values of the quantum of conductivity e^2/h. For monolayer graphene, the Landau level spectrum was calculated over fifty years ago by McClure [105], and the integer quantum Hall effect was observed [36, 85] and studied theoretically [84, 90, 107, 108, 109] in recent years. The chiral nature of electrons in graphene results in an unusual sequencing of the quantized plateaus of the Hall conductivity. In bilayer graphene, the experimental observation of the integer quantum Hall effect [37] and calculation of the Landau level spectrum [91] revealed further unusual features related to the chirality of electrons.

2.8.1 The Landau Level Spectrum of Monolayer Graphene

The motion of charge carriers in 2DEG in a magnetic field is quantized, the motion of relativistic charges in graphene in a strong magnetic field is also quantized. In a conventional electron gas (non-relativistic) Landau quantization produces equidistant energy levels, which is due to the parabolic dispersion law of free electrons. In graphene

the electrons have relativistic dispersion law, which strongly modifies the Landau quantization of the energy and the position of the levels. In the Dirac like Hamiltonian (2.5.7) for free electron in graphene, we make the substitution $p_i \to p_i = p_i - \frac{eA_i}{c}$ when perpendicular magnetic field is applied to graphene. Let us find the energy eigenvalues E for stationary equation [99]:

$$v_F \begin{pmatrix} 0 & \pi_x - i\pi_y \\ \pi_x + i\pi_y & 0 \end{pmatrix} \begin{pmatrix} \psi_A \\ \psi_B \end{pmatrix} = E \begin{pmatrix} \psi_A \\ \psi_B \end{pmatrix}, \tag{2.8.1}$$

where $\pi_x = p_x - eA_x/c, \pi_y = p_y - eA_y/c$, where ψ_A and ψ_B are the spinor wave function, E is the energy eigne value, $\hat{p} = \hbar\nabla/i$ is the charge carrier momentum, and $\vec{A}$ is the vector potential and $\vec{B} = \nabla \times \vec{A}$. And Eq.(2.8.1) can be written as two equations:

$$\begin{cases} v_F[\pi_x - i\pi_y]\psi_B = E\psi_A, \\ v_F[\pi_x + i\pi_y]\psi_A = E\psi_B. \end{cases} \tag{2.8.2}$$

Again by inserting one equation into another the above equation can further decoupled into

$$\begin{cases} v_F^2[\pi_x - i\pi_y][\pi_x + i\pi_y]\psi_A = E^2\psi_A, \\ v_F^2[\pi_x + i\pi_y][\pi_x - i\pi_y]\psi_B = E^2\psi_B. \end{cases} \tag{2.8.3}$$

In the above equation for a charge carriers in a uniform magnetic field , $\vec{B}$, say along z-direction , we can choose the vector potential as $A_x = 0, A_y = Bx, A_z = 0$ (Landau gauge). Note that at this choice of $\vec{A}$ we get only z-component of magnetic field ($\vec{B}$). Then substituting, the vector potentials and the x and y components of the momentum, in (2.8.3), we obtain

$$\begin{cases} v_F^2[p_x - i(p_y - \frac{eBx}{c})][p_x + i(p_y - \frac{eBx}{c})]\psi_A = E^2\psi_A, \\ v_F^2[p_x + i(p_y - \frac{eBx}{c})][p_x - i(p_y - \frac{eBx}{c})]\psi_B = E^2\psi_B, \end{cases} \tag{2.8.4}$$

after simplification of the above equations, we get the following

$$\begin{cases} [p_x^2 + i[p_y, p_x] + i\frac{eB}{c}[x, p_x] + (p_y - \frac{eBx}{c})^2]\psi_A = \frac{E^2}{v_F^2}\psi_A, \\ [p_x^2 + i[p_y, p_x] - i\frac{eB}{c}[x, p_x] + (p_y - \frac{eBx}{c})^2]\psi_B = \frac{E^2}{v_F^2}\psi_B. \end{cases} \tag{2.8.5}$$

By using commutation relations, $[p_x, p_y] = [p_y, p_x] = 0$, and $[x, p_x] = i\hbar$, the equations can be further simplified as follows

$$\begin{cases} [\frac{p_x^2}{2m} + \frac{e^2B^2}{2mc^2}(x - \frac{p_y c}{eB})^2]\psi_A = \frac{1}{2m}(\frac{E^2}{v_F^2} + \frac{eB\hbar}{c})\psi_A, \\ [\frac{p_x^2}{2m} + \frac{e^2B^2}{2mc^2}(x - \frac{p_y c}{eB})^2]\psi_B = \frac{1}{2m}(\frac{E^2}{v_F^2} - \frac{eB\hbar}{c})\psi_B. \end{cases} \tag{2.8.6}$$

Now let us substitute the following variables $\omega_c = \frac{eB}{mc}$, $x_0 = \frac{p_y c}{eB}$, $\varepsilon_\pm = \frac{1}{2m}(\frac{E^2}{v_F^2} \pm \frac{eB\hbar}{c})$, then the resulting equation is one dimensional Schrodinger equation for simple harmonic oscillator frequency ω_c (the cyclotron frequency) and displacement $(x - x_0)$. Thus harmonic oscillator equations given by

$$\begin{cases} [\frac{p_x^2}{2m} + \frac{m\omega_c}{2}(x - x_0)^2]\psi_A = \varepsilon_+\psi_A, \\ [\frac{p_x^2}{2m} + \frac{m\omega_c}{2}(x - x_0)^2]\psi_B = \varepsilon_-\psi_B. \end{cases} \tag{2.8.7}$$

From which, we get the quantized energy and wave function [100, 101]. The quantized energy of the different oscillator levels Landau Levels (the energy eigenvalue of free electron Hamilton in a uniform magnetic field $\vec{B}$ to the z-direction) is obtained as a solution of the the above equation as [100, 101]

$$\varepsilon_\pm = \hbar\omega_c(n + \frac{1}{2}), \tag{2.8.8}$$

where $n = 0, 1, 2, 3, ...$ goes through the same values as for harmonic oscillator. Since E has positive and negative roots, we can extend the domain of n to integer values and write energy levels as

$$\begin{cases} E_A = \pm v_F\sqrt{\frac{2\hbar eB}{c}n} = \pm\hbar\omega^{Dirac}\sqrt{n}, \\ E_B = \pm v_F\sqrt{\frac{2\hbar eB}{c}(n+1)} = \pm\hbar\omega^{Dirac}\sqrt{n+1}. \end{cases} \tag{2.8.9}$$

Here, $\omega^{Dirac} = v_F\sqrt{\frac{2eB}{\hbar c}}$ denotes the analogues expression to cyclotron frequency $\omega_c = \frac{eB}{mc}$. The Landau level index, n, can be positive or negative. The positive values correspond to electrons (conduction band), while the negative values correspond to holes (valence band). Furthermore, they are not equidistant as in conventional case and the largest energy separation is between the zero and the first Landau level. This large gap allows one to observe the quantum Hall effect in graphene, even at room temperature [10].

If we compar the results (2.8.9) for the A and B sublattice. In the wavefunction, ψ_B , lacks the level with $E_B = 0$. In terms of the occupation of the sublattices A and B, we can therefore expect interesting properties. Specifically, the wave function at the Landau level $n \neq 0$ should always have non-zero amplitudes on both sublattices A and B, while the wavefunctions at the Landau level $n = 0$ should have non-zero amplitude only on one sublattice: B sublattice for valley K_+ or A sublattice for valley K_-. The asymmetry between A and B sublattice originates from asymmetry in positions of the nearest neighbors for atoms at A and B sublattice. This property of the wavefunctions for the Landau levels in graphene makes the $n = 0$ level very special for different magnetic applications of graphene.

The wave functions corresponding to the Landau levels (2.8.9) are labeled by three indices. Using the Landau gauge $\mathbf{A} = (0, Bx, 0)$ preserves translational invariance in the y direction, so that eigenstates may be written in terms of states that are plane waves in the y direction and harmonic oscillator states in the x direction [41, 42],

$$\phi_n(x, y) = A_n H_n\left(\frac{x}{\lambda_B} - \frac{p_y\lambda_B}{\hbar}\right)\exp\left[-\frac{1}{2}\left(\frac{x}{\lambda_B} - \frac{p_y\lambda_B}{\hbar}\right)^2 + i\frac{p_y y}{\hbar}\right] \tag{2.8.10}$$

Here, H_n are Hermite polynomials of order n, for integer $n \geq 0$, and the normalization constant is $A_n = 1/\sqrt{2^n n!\sqrt{\pi}}$. The magnetic length λ_B, and a related energy scale

Γ, are defined as

$$\lambda_B = \sqrt{\frac{\hbar c}{eB}}. \tag{2.8.11}$$

In (2.8.10) the wave function, $\phi_n(x, y)$, depend on the parameters n, p_y, where as in (2.8.9) the Landau Level energy, E, depends only on the parameters n. This implies degeneracy [99].

2.8.2 The Landau Level degeneracy of monolayer graphene

The Landau Levels energy in Eq.(2.8.9) is not dependent on the momentum p_y, where as the wave functions, $\phi_n(x, y)$, Eq.(2.8.10) depend on the parameters n, p_y. This means that the Landau levels (2.8.9) have a macroscopically large degeneracy g. To calculate it, it is convenient to use a periodic (Born von Karman) boundary condition in the y-direction,

$$\psi_{A,B}(x, y) = \psi_{A,B}(x, y + L_y), \tag{2.8.12}$$

(for large enough samples the density of states does not depend on boundary conditions, Vonsovsky and Katsnelson (1989)). Thus,

$$k_y = \frac{2\pi}{L_y} n, \tag{2.8.13}$$

where $n = 0, \pm 1, ...$ The maximum value of n is determined by the condition that the centre of the orbit should be within the sample: $0 < x_0 < L_x$ (L_x is the width of the sample in the x-direction), or

$$|k_y| < \frac{L_x}{\lambda_B^2} = \frac{|e|BL_x}{hc}. \tag{2.8.14}$$

Thus, the total number of solutions is

$$g = \frac{|e|B}{hc}\frac{L_x L_y}{2\pi} = \frac{|e|B}{hc}\frac{A}{2\pi} = \frac{\phi}{\phi_0}. \tag{2.8.15}$$

where $A = L_x L_y$ is the sample area, ϕ is the total magnetic flux though the sample and

$$\phi_0 = \frac{hc}{|e|}. \tag{2.8.16}$$

is the flux quantum. Keeping in mind further applications to graphene, one should multiply the degeneracy (2.8.15) by a factor of 4, namely a factor of 2 for the two valleys K_+ and K_- and a further factor of 2 for the two spin projections. The latter is possible since the ratio of the Zeeman energy $E_z = |e|hB/(2mc)$ to the cyclotron quantum $h\omega_c$ is always very small (about 0.01 in fields $B \approx 10 - 30T$).

We can solve the Landau Levels in graphene using operator method. We will see later that this representation is very convenient for the cases of both single-layer and, especially, bilayer graphene [99]. The Dirac-like Hamiltonian of monolayer graphene (2.5.7) may be written as

$$H_{1,K_+} = \nu_F \begin{pmatrix} 0 & \pi_- \\ \pi_+ & 0 \end{pmatrix}, \qquad H_{1,K_-} = -\nu_F \begin{pmatrix} 0 & \pi_+ \\ \pi_- & 0 \end{pmatrix}, \tag{2.8.17}$$

in the vicinity of corners of the Brillouin zone K_+ and K_-, respectively, where

$$\pi_+ = (p_x - \frac{eA_x}{c}) + i(p_y - \frac{eA_y}{c}), \qquad \pi_- = (p_x - \frac{eA_x}{c}) - i(p_y - \frac{eA_y}{c}), \tag{2.8.18}$$

We consider a magnetic field perpendicular to the graphene sheet, $\mathbf{A} = (0, Bx, 0)$. With this choice of vector potential, acting on the harmonic oscillator states (2.8.10) gives

$$\pi_+ \phi_n = -\frac{\sqrt{2}i\hbar}{\lambda_B}\sqrt{n}\phi_{n-1}, \tag{2.8.19}$$

$$\pi_- \phi_n = \frac{\sqrt{2}i\hbar}{\lambda_B}\sqrt{n+1}\phi_{n+1}, \tag{2.8.20}$$

and $\pi_+\phi_0 = 0$. These equations indicate that operators π_+ and π_- are proportional to lowering and raising operators of the harmonic oscillator states ϕ_n. The Landau level spectrum is, therefore, straightforward to calculate [43, 44, 45]. At the first valley, K_+, the Landau level energies and eigenstates of H_{1,K_+} are

$$K_+, n \geq 1 : E_{n,\pm} = \pm\frac{\sqrt{2}\hbar\nu}{\lambda_B}\sqrt{n}, \qquad \psi_{n,\pm} = \frac{1}{\sqrt{2}}\begin{pmatrix} \phi_n \\ \pm i\phi_{n-1} \end{pmatrix}, \tag{2.8.21}$$

$$K_+, n = 0 : E_0 = 0, \qquad \psi_0 = \begin{pmatrix} \phi_0 \\ 0 \end{pmatrix}, \tag{2.8.22}$$

where $\pm$ refer to the conduction and valence bands, respectively. Equation (2.8.16) describes an electron (plus sign) and a hole (minus sign) series of energy levels, with prefactor (2.8.11), proportional to the square root of the magnetic field. In addition, there is a special level (2.8.17) fixed at zero energy that arises from the presence of the lowering operator in the Hamiltonian, $\pi_+\psi_0 = 0$. The corresponding eigenfunction ψ_0 has non-zero amplitude on the A sublattice, but its amplitude is zero on the B sublattice. The form (2.8.12) of the Hamiltonian H_{1,K_-} at the second valley, K_-, shows that its spectrum is degenerate with that at K_+, with the role of the A and B sublattices reversed:

$$K_-, n \geq 1 : E_{n,\pm} = \pm\frac{\sqrt{2}\hbar\nu}{\lambda_B}\sqrt{n}, \qquad \psi_{n,\pm} = \frac{1}{\sqrt{2}}\begin{pmatrix} \pm i\phi_{n-1} \\ \phi_n \end{pmatrix}, \tag{2.8.23}$$

$$K_-, n = 0 : E_0 = 0, \qquad \psi_0 = \begin{pmatrix} 0 \\ \phi_0 \end{pmatrix}. \tag{2.8.24}$$

Thus, the eigenfunction ψ_0 of the zero-energy level has zero amplitude on the B sublattice at valley K_+ and zero amplitude on the A sublattice at K_-. If we take into account electronic spin, which contributes a twofold degeneracy of the energy levels,

as well as valley degeneracy, then the Landau level spectrum of monolayer graphene consists of fourfold-degenerate Landau levels.

2.8.3 The Integer Quantum Hall Effect in Monolayer Graphene

In this section, we describe how the Landau level spectrum of graphene is reflected in the dependence of the Hall conductivity $\sigma_{xy}(n)$ on carrier density n. In conventional two-dimensional semiconductor systems, in the absence of any Berrys phase effects, the Landau level spectrum is given by $E_n = \hbar\omega_c(n + 1/2)$, $n \geq 0$, where $\omega_c = eB/mc$ is the cyclotron frequency [103, 104]. Here, the lowest state lies at finite energy $E_0 = \hbar\omega_c/2$. If the system has an additional degeneracy g (for example, $g = 2$ for spin), then plateaus [102, 103, 104] occur at quantized σ_{xy} values of $\nu(ge^2/h)$ where ν is an integer and e^2/h is the quantum value of conductance, i.e. each step between adjacent plateaus has height ge^2/h, Fig. 2.9(a). Each σ_{xy} step coincides with the crossing of a Landau level on the density axis. Since the maximum carrier density per Landau level is gB/ϕ_0, where $\phi_0 = hc/e$ is the flux quantum, the distance between the σ_{xy} steps on the density axis is gB/ϕ_0.

As described above, monolayer graphene has fourfold (spin and valley) degenerate Landau levels $E_{n,\pm} = \pm\sqrt{2}\hbar n/\lambda_B$ for $n \geq 1$ and $E_0 = 0$. The Hall conductivity $\sigma_{xy}(n)$, Fig. 2.9(b), displays a series of quantized plateaus separated by steps of size $4e^2/h$, as in the conventional case, but the plateaus occur at half-integer values of $4e^2/h$ rather than integer ones:

$$\sigma_{xy} = -\frac{1}{2}(2\upsilon + 1)\frac{4e^2}{h}, \tag{2.8.25}$$

where υ is an integer, as observed experimentally [36, 85] and described theoretically [84, 90, 107, 108, 109]. This unusual sequencing of σ_{xy} plateaus is explained by the

presence of the fourfold-degenerate Landau level E_0 fixed at zero energy. Since it lies at the boundary between the electron and hole gases, it creates a step in σ_{xy} of $4e^2/h$ at zero density. Each Landau level in monolayer graphene is fourfold degenerate, including the zero energy one, so the distance between each σ_{xy} step on the density axis is $4B/\phi_0$, i.e. the steps occur at densities equal to integer values of $4B/\phi_0$.

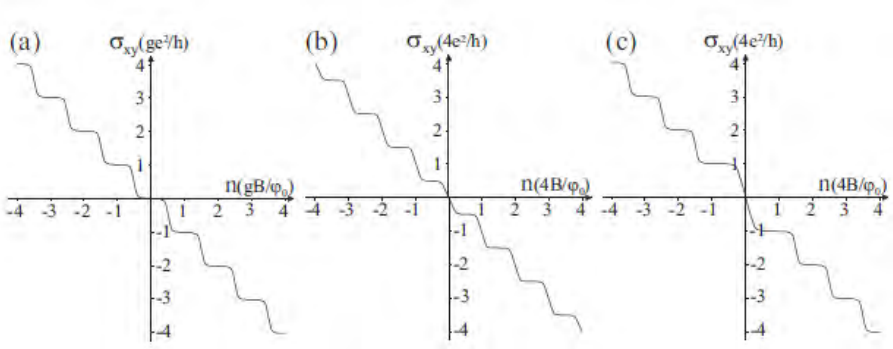

Figure 2.9: Schematic representation of three types of integer quantum Hall effect, showing the density dependence of the Hall conductivity $\sigma_{xy}(n)$: (a) conventional two-dimensional semiconductor systems with additional system degeneracy g; (b) monolayer graphene; (c) bilayer graphene. Here, B is the magnitude of the magnetic field and $\phi_0 = h/e$ is the flux quantum.

2.8.4 The Landau Level Spectrum of Bilayer Graphene

In the presence of a perpendicular magnetic field, the Hamiltonian (2.6.15) describing massive chiral electrons in bilayer graphene may be written as

$$H_{1,K_+} = -\frac{1}{2m}\begin{pmatrix} 0 & \pi_-^2 \\ \pi_+^2 & 0 \end{pmatrix}, H_{1,K_-} = -\frac{1}{2m}\begin{pmatrix} 0 & \pi_+^2 \\ \pi_-^2 & 0 \end{pmatrix}, \tag{2.8.26}$$

in the vicinity of corners of the Brillouin zone K_+ and K_-, respectively. Using the action of operators π_+ and π_- on the harmonic oscillator states ϕ_n , (2.8.14) and (2.8.15), the Landau level spectrum of bilayer graphene may be calculated [91]. At

the first valley, K_+, the Landau level energies and eigenstates of H_{2,K_+} are

$$K_+, n \geq 2 : E_{n,\pm} = \pm\frac{\hbar^2}{m\lambda_B^2}\sqrt{n(n-1)}, \psi_{n,\pm} = \frac{1}{\sqrt{2}}\begin{pmatrix} \phi_n \\ \pm i\phi_{n-2} \end{pmatrix}, \tag{2.8.27}$$

$$K_+, n = 1 : E_1 = 0, \psi_n = \begin{pmatrix} \phi_1 \\ 0 \end{pmatrix}, \tag{2.8.28}$$

$$K_+, n = 0 : E_0 = 0, \psi_0 = \begin{pmatrix} \phi_0 \\ 0 \end{pmatrix}, \tag{2.8.29}$$

where $\pm$ refer to the conduction and valence bands, respectively. Equation (2.8.22) describes an electron (plus sign) and a hole (minus sign) series of energy levels. The prefactor $\hbar^2/(m\lambda_B^2)$ is proportional to the magnetic field, and it may equivalently be written as Γ^2/γ_1 or as $\hbar\omega_c$ where $\omega_c = eB/mc$. For high levels, $n >> 1$, the spectrum consists of approximately equidistant levels with spacing $\hbar\omega_c$. Note, however, that we are considering the low-energy Hamiltonian, so that the above spectrum is only valid for sufficiently small level index and magnetic field $\sqrt{n}\Gamma << \gamma_1$. As well as the field-dependent levels, there are two special levels, (2.8.23) and (2.8.24), fixed at zero energy. There are two zero-energy levels because of the presence of the square of the lowering operator in the Hamiltonian. It may act on the oscillator ground state to give zero energy, $\pi_+^2\phi_0 = 0$, (2.8.24), but also on the first excited state to give zero energy, $\pi_+^2\phi_1 = 0$, (2.8.23). The corresponding eigenfunctions ψ_0 and ψ_1 have non-zero amplitude on the A1 sublattice, that lies on the bottom layer, but their amplitude is zero on the B2 sublattice.

The form (2.8.21) of the Hamiltonian H_{2,K_-} at the second valley, K_-, shows that its spectrum is degenerate with that at K_+ with the role of the A1 and B2 sublattices reversed. It may be expressed as $H_{2,K_-} = \sigma_x H_{2,K_+}\sigma_x$ so that $\psi_{n,\pm}(K_-) = \sigma_x\psi_{n,\pm}(K_+)$, $\psi_n(K_-) = \sigma_x\psi_n(K_+)$, and $\psi_0(K_-) = \sigma_x\psi_0(K_+)$. Thus, the eigenfunctions ψ_0 and ψ_1

of the zero-energy levels have zero amplitude on the B2 sublattice at valley K_+ and zero amplitude on the A1 sublattice at K_-. If we take into account electronic spin, which contributes a twofold degeneracy of the energy levels, as well as valley degeneracy, then the Landau level spectrum of bilayer graphene consists of fourfold degenerate Landau levels, except for the zero-energy levels which are eightfold degenerate. This doubling of the degeneracy of the zero-energy levels is reflected in the density dependence of the Hall conductivity.

2.8.5 The Integer Quantum Hall Effect in Bilayer Graphene

The Hall conductivity $\sigma_{xy}(n)$ of bilayer graphene, Fig. 2.9(c), displays a series of quantized plateaus occurring at integer values of $4e^2/h$ that is practically the same as in the conventional case, Fig. 2.9(a), with degeneracy per level $g = 4$ accounting for spin and valleys. However, there is a step of size $8e^2/h$ in σ_{xy} across zero density in bilayer graphene [37, 91]. This unusual behavior is explained by the eightfold degeneracy of the zero-energy Landau levels. Their presence creates a step in σ_{xy} at zero density, as in monolayer graphene, but owing to the doubled degeneracy as compared to other levels, it requires twice as many carriers to fill them. Thus, the transition between the corresponding plateaus is twice as wide in density, $8B/\phi_0$ as compared to $4B/\phi_0$, and the step in σ_{xy} between the plateaus must be twice as high, $8e^2/h$ instead of $4e^2/h$. This demonstrates that, although Berrys phase 2π is not reflected in the sequencing of quantum Hall plateaus at high density, it has a consequence in the quantum limit of zero density, as observed experimentally [37].

Here, we showed that the chiral Hamiltonians of monolayer and bilayer graphene

corresponding to Berrys phase π and 2π, respectively, have associated four- and eight-fold degenerate zero-energy Landau levels, producing steps of four and eight times the conductance quantum e^2/h in the Hall conductivity across zero density [36, 37, 85]. In our discussion, we neglected interaction effects and we assumed that any valley and spin splitting, or splitting of the $n = 1$ and $n = 0$ levels in bilayer graphene, are negligible as compared to temperature and level broadening.

Chapter 3

2D Electron Scattering Theory

3.1 Scattering theory for 2D Schrodinger electrons

3.1.1 Asymptotic wave function

Consider a free particle moving in the positive x-axis is described by plane wave, which we take in the form, $\psi = e^{ikx}$, and the scattered particle is described at great distance from the scattering center, by an outgoing spherical wave of the form $f(\varphi)R(r)$, where $f(\varphi)$ is a function of scattering angle φ (angle between the x-axis and the direction of scattered particle). This function is called scattering amplitude. Thus the exact wavefunction which is a solution of schrodinger equation with a potential $V(\rho)$ must have at large distance the asymptotic form [99, 100]

$$\psi(\rho, \varphi) = e^{ikx} + f(\varphi)R(\rho). \tag{3.1.1}$$

Now we start from the two-dimensional stationary Schrodinger equation with a potential $V(\rho)$ depending only on the distance ρ from the origin:

$$-\frac{\hbar^2}{2m}\nabla^2\psi(\rho, \varphi) + V(\rho)\psi(\rho, \varphi) = E\psi(\rho, \varphi), \tag{3.1.2}$$

leads to the following differential equation for the wave function

$$\left[\frac{\partial^2}{\partial\rho^2}+\frac{1}{\rho}\frac{\partial}{\partial\rho}+\frac{1}{\rho^2}\frac{\partial^2}{\partial\varphi^2}+\frac{2m}{\hbar^2}(E-V(\rho))\right]\psi(\rho,\varphi)=0. \tag{3.1.3}$$

On expressing the wave function as the product

$$\psi(\rho,\varphi)=R(\rho)e^{im\varphi}, m=0,1,2,..., \tag{3.1.4}$$

the resulting differential equation for the radial, $R(\rho)$, part of the wave function can be given by

$$\left[\frac{\partial^2}{\partial\rho^2}+\frac{1}{\rho}\frac{\partial}{\partial\rho}-\frac{m^2}{\rho^2}+\frac{2m}{\hbar^2}(E-V(\rho))\right]R(\rho)=0, \tag{3.1.5}$$

where m and E denotes the angular momentum and the energy spectra, respectively.

And now multiply both side of Eq.(3.1.5) by ρ^2 and let $V(\rho)=0$ rearranging the equation, it leads to,

$$\left[\rho^2\frac{\partial^2}{\partial\rho^2}+\rho\frac{\partial}{\partial\rho}+k^2\rho^2-m^2\right]R(\rho)=0. \tag{3.1.6}$$

We now make the following change of variable:

$r=k\rho$

so that

$$\begin{aligned}\frac{d}{d\rho}&=\frac{d}{dr}\frac{dr}{d\rho}=k\frac{d}{dr},\\ \frac{d^2}{d\rho^2}&=k^2\frac{d^2}{dr^2}.\end{aligned} \tag{3.1.7}$$

By use of this change of variable, Eq.(3.1.6) reduces to

$$\left[r^2\frac{\partial^2}{\partial r^2}+r\frac{\partial}{\partial r}+r^2-m^2\right]R(r)=0, \tag{3.1.8}$$

which is Bessel's equation, and its solutions are called Bessel functions. The solution to this equation is,[99, 100]

$$R(r)=AJ_m(r)+BY_m(r). \tag{3.1.9}$$

Which is linear combination of $J_m(r)$ called the first kind m order Bessel function and $Y_m(r)$ called the second kind m order Bessel function. Note that Bessel function of the first kind are diverge at infinity but Bessel function of second kind are well behave at large r. So in our solution we drop Bessel function of first kind and take bessel function of second kind i.e

$$R(r) = BY_m(r). \tag{3.1.10}$$

And Hanckel function of the first kind can be written as

$$H_m^1(r) = J_m(r) + iY_m(r). \tag{3.1.11}$$

So at large r

$$R(r) = -iH_m^1(r), \tag{3.1.12}$$

the asymptote of the Hankel function [100, 111] is

$$H_m^1(r) \approx \frac{1-i}{\sqrt{\pi r}} e^{ir}, \tag{3.1.13}$$

then the radial function is

$$R(r) \approx A\frac{e^{ir}}{\sqrt{\pi r}}. \tag{3.1.14}$$

Therefore, the solution of schrodinger equation must have at large distance the asymptotic form

$$\psi(\rho, \varphi) = e^{ikx} + f(\varphi)\frac{e^{ir}}{\sqrt{-ir}}. \tag{3.1.15}$$

3.1.2 Partial Wave Method

Having established the basic concepts for the scattering problem, we turn now to consider operationally how the scattering characteristics can be computed. Here, for simplicity, we will focus on the properties of a centrally symmetric potential, $V(r)$, where the scattering wavefunction, $\psi(r)$ (and indeed that scattering amplitudes, $f(\varphi)$ must be symmetrical about the axis of incidence. In this case, the radial wavefunction can be expanded as the solutions (3.1.9) are the Bessel functions $J_m(r)$ and the Neumann functions $Y_m(r)$, whose asymptotic behavior [99, 100, 112]

$$J_m(r >> m) \simeq \sqrt{\frac{2}{\pi r}} \cos\left(r - \frac{m\pi}{2} - \frac{\pi}{4}\right), \tag{3.1.16}$$

$$Y_m(r >> m) \simeq \sqrt{\frac{2}{\pi r}} \sin\left(r - \frac{m\pi}{2} - \frac{\pi}{4}\right). \tag{3.1.17}$$

Their corresponding short-distance behavior is

$$J_m(kr) \sim \frac{1}{m!}\left(\frac{kr}{2}\right)^m, \tag{3.1.18}$$

and

$$Y_m(kr) \sim \begin{cases} -\frac{\Gamma(m)}{\pi}(\frac{2}{kr})^m, & m > 0; \\ \frac{2}{\pi} ln\gamma_E kr/2, & m = 0, \end{cases} . \tag{3.1.19}$$

where $\gamma_E = 0.577$ is the Eulers constant. [For $m < 0$, we use $J_{-m} = (-1)^m J_m$ and $Y_{-m} = (-1)^m Y_m$]. Thus for the wave regular at $r = 0$, one chooses $R_m \propto J_m(kr)$, the solution of radial wave function R_{km} normalized according to $\int_0^\infty r dr R_{km} R_{k'm'} = 2\pi\delta_{m,m'}\delta(k - k')$ [100, 112]:

$$R_{km} = \sqrt{2\pi k} \times J_m(kr) \sim \sqrt{\frac{2}{\pi kr}} \cos\left(kr - \frac{m\pi}{2} - \frac{\pi}{4}\right). \tag{3.1.20}$$

Scattering amplitude and cross section

Now let us develop the elastic scattering theory for the 2D schrodinger fermions in the presence of the axially symmetric potential $V(r)$. Our objective is to express the scattering amplitude and the cross section in terms of the scattering phase shifts for the spherical waves of the form (3.1.15).

First we recall that in the nonrelativistic case, with the incident flux along the x-direction, in two dimensional case the wave function far from the scatterer is superposition of a plane wave and outgoing spherical wave, then the wave function has the asymptotic form [100, 112]

$$\psi(r,\varphi) = e^{ikx} + f(\varphi)\frac{e^{ikr}}{\sqrt{-ir}}, \tag{3.1.21}$$

where f is the 2D scattering amplitude. The differential and the total cross sections, that have the dimensionality of length, are [100, 112]

$$\frac{d\sigma}{d\varphi} = |f(\varphi)|^2 \tag{3.1.22}$$

$$\sigma_{tot} = \int_0^{2\pi} |f(\varphi)|^2 d\varphi \tag{3.1.23}$$

We have denoted the scattering cross section by σ, one way to find the scattering amplitude f is to represent the wave function ψ in the spherical wave basis.

A solution of schrodinger equation for scattering in the potential $V(r)$, must evidently axially symmetric about the x-axis, the direction of the incident particles. Any solution can be represented as superposition of wave function of different spectrum, corresponding to motion, of particles with given energy E and orbital angular momentum, m and zero x-component; this functions are independent azimuthal angle φ

around the x-axis, i.e they are symmetric. Thus the required wave function has the form [100, 112]

$$\psi(r,\varphi) = \sum_{m=-\infty}^{\infty} A_m R_{km}(r)\Phi(\varphi), \tag{3.1.24}$$

where A_m are constants and the R_{km} are radial functions satisfying the equation

$$\left[\frac{\partial^2}{\partial r^2} + \frac{1}{r}\frac{\partial}{\partial r} - \frac{m^2}{r^2} + k^2 - \frac{2mV(r)}{\hbar^2}\right] R(r) = 0. \tag{3.1.25}$$

For each of the radial components R_{km} the scattering phase shifts δ_m are then defined by the asymptotic form of the solutions of Eq. (3.1.25)[100, 112]:

$$R_{km} \simeq \sqrt{\frac{2}{\pi kr}} \cos\left(\Delta_m + \delta_m\right), \tag{3.1.26}$$

where $\Delta_m = kr - \frac{m\pi}{2} - \frac{\pi}{4}$.

Substituting the asymptotic form of the function (3.1.26) in (3.1.24), we obtain the asymptotic expression for the wave function in the form

$$\begin{aligned} \psi(r,\varphi) &= \sqrt{\frac{2}{\pi kr}} \sum_{m=-\infty}^{\infty} A_m e^{im\varphi} \cos\left(\Delta_m + \delta_m\right), \\ &= \frac{1}{\sqrt{2\pi kr}} \sum_{m=-\infty}^{\infty} A_m e^{im\varphi} \left(e^{i(\Delta_m+\delta_m)} + e^{-i(\Delta_m+\delta_m)}\right). \end{aligned} \tag{3.1.27}$$

In the absence of the potential, the phase shift δ_m, must be zero and the wave function should be of the form written below. Using the decomposition of the plane wave

$$\begin{aligned} e^{ikx} = e^{ikrcos\varphi} &= \sum_{m=-\infty}^{\infty} i^m e^{im\varphi} J_m(kr), \\ &\simeq \sqrt{\frac{2}{\pi kr}} \sum_{m=-\infty}^{\infty} i^m e^{im\varphi} \cos\Delta_m \\ &= \frac{1}{\sqrt{2\pi kr}} \sum_{m=-\infty}^{\infty} i^m e^{im\varphi} (e^{i\Delta_m} + e^{-i\Delta_m}). \end{aligned} \tag{3.1.28}$$

The coefficient A_m must be chosen so that at large distance the function Eq.(3.1.27) has asymptotic form Eq.(3.1.21). One can show that this implies that

$$A_m = \frac{i^m}{\sqrt{2}} e^{i\delta_m}, \tag{3.1.29}$$

and expressing the scattering amplitude in terms of the phase shifts in the two dimensional case

$$f(\varphi) = \frac{1}{i\sqrt{2\pi k}} \sum_{m=-\infty}^{\infty} (e^{2i\delta_m} - 1) e^{im\varphi}, \tag{3.1.30}$$

and finally the differential cross-section (3.1.22) becomes:

$$\frac{d\sigma}{d\varphi} = \frac{2}{\pi k} \sum_{m=-\infty}^{\infty} e^{im\varphi} e^{2i\delta_m} \sin^2 \delta_m. \tag{3.1.31}$$

Now we insert the obtained differential cross section into Eq. (3.1.23) and integration gives the total cross section

$$\sigma_{tot} = \frac{4}{k} \sum_{-\infty}^{\infty} \sin^2 \delta_m, \tag{3.1.32}$$

also we are interested in the transport cross section [99, 112]

$$\sigma_{tr} = \int_0^{2\pi} |f(\varphi)|^2 (1 - \cos(\varphi)) d\varphi = \frac{4}{k} \sum_{-\infty}^{\infty} \sin^2(\delta_{m+1} - \delta_m) \tag{3.1.33}$$

3.1.3 The 2D Born approximation

The scattering cross section can be calculated in a general form in a very important condition, when the energy of the incident beam is large in comparison with the magnitude of the potential energy, i.e $|U| << E$ in Born approximation [100, 112]. We can start from the 2D schrodinger equation

$$\left[-\frac{\hbar^2}{2m} \nabla^2 + V(\rho) \right] \psi(\rho) = E\psi(\rho), \tag{3.1.34}$$

in the form

$$\left[\nabla^2 + k^2\right]\psi(\rho) = \frac{2m}{\hbar^2}V(\rho)\psi(\rho), \tag{3.1.35}$$

where $k = \sqrt{2mE/\hbar^2}$. The incoming plane wave $Ae^{ik\rho}$ is a solution to the equation

$$\left[\nabla^2 + k^2\right]\psi(\rho) = 0. \tag{3.1.36}$$

It is convenient to express the formal solution to (3.1.35) in the form

$$\psi(\vec{\rho}) = Ae^{ik\rho} + \frac{2m}{\hbar^2}\int d^2\rho' G(\vec{\rho},\vec{\rho'})V(\rho')\psi(\rho'). \tag{3.1.37}$$

The function $G(\rho,\rho')$ is Green's function of differential equation (3.1.36) and itself satisfies the differential equation. The Green function in (3.1.37) in the cylindrical geometry is the first kind zeroth order Hankel function [111] given by

$$G(\rho,\rho') = -\frac{i}{4}H_0^{(1)}(k|\rho-\rho'|). \tag{3.1.38}$$

At $(\rho'/\rho << 1)$, it has the asymptotic behaviour Hankel function

$$H_0^{(1)}(k|\rho-\rho'|) \simeq \frac{1-i}{\sqrt{\pi\rho k}}e^{ik(\rho-\vec{\rho'}.\vec{n})}, \tag{3.1.39}$$

where, $\vec{n} = \vec{\rho}/\rho$. Hence

$$G(\rho,\rho') = -\frac{1}{\sqrt{8\pi k}}\frac{1}{\sqrt{-i\rho}}e^{ik(\rho-\vec{\rho'}.\vec{n})}, \tag{3.1.40}$$

and

$$\psi(\rho) = Ae^{ik\rho} - \frac{m}{2\pi\hbar^2}\int d^2\rho' H_0^{(1)}(k\rho')V(\rho')\psi(\rho'). \tag{3.1.41}$$

Generally, the range of the ρ' integral is limited by the range of the potential energy $V(r')$ to a microscopic distance. In order to determine the scattering amplitude, we

need to examine the behavior of the wave function as $\rho \to \infty$. In this case, since $\rho >> |\rho'|$, we approximate

$$|\rho - \rho'| = \rho \left(1 - 2u_\rho \cdot \frac{\rho'}{\rho} + \frac{\rho'^2}{\rho^2}\right)^{1/2} \to \rho \left(1 - 2u_\rho \cdot \frac{\rho'}{\rho}\right), \tag{3.1.42}$$

where we have neglected terms of order (ρ'/ρ). Thus in (3.1.42) we can make replacement

$$\frac{1}{|\rho - \rho'|} \to \rho \left(1 - 2u_\rho \cdot \frac{\rho'}{\rho}\right) \to \frac{1}{\rho}, \tag{3.1.43}$$

since the terms that we are neglecting make a vanishing contribution to the integral relative to the one that we have retained as $\rho \to \infty$. However, within the exponent all that matters is the value of the phase $k\rho$ modulo 2π, no matter how large ρ is. Thus we need to retain both the first two terms in the expansion (3.1.42), namely,

$$e^{ik|\rho-\rho'|} \to e^{ik\rho\left(1-u_\rho \cdot \frac{\rho'}{\rho}\right)} = e^{ik\rho} e^{-ik_f \rho'}, \tag{3.1.44}$$

where

$$k_f = k u_\rho, \tag{3.1.45}$$

points in the direction of the outgoing scattered wave. Again, the terms of order $(\rho'/\rho)^2$ can be safely neglected relative to the two terms that we have retained. With these approximations, (3.1.41) in the asymptotic limit becomes

$$\psi(r) = Ae^{ik\rho} - \frac{me^{ik\rho}}{2\pi\hbar^2\rho} \int d^2\rho' e^{-ik_f \cdot \rho'} V(\rho')\psi(\rho'), \tag{3.1.46}$$

we are now ready for the Born approximation. As we remarked earlier, (3.1.46) is an integral equation that involves the wave function ψ on the right side within the integral, as well as on the left side. If the potential energy V were set to zero,

the solution for ψ would be simply $\psi = Ae^{ik\rho}$. This suggests that if magnitude of the potential energy is small compared with the energy E, we can replace the wave function $\psi(\rho')$ within the integral with that of incident wave. Then

$$\psi(\rho) = Ae^{ik\rho} - \frac{m}{2\pi\hbar^2}\frac{e^{ik\rho}}{\rho}\int d^2\rho' e^{-ik_f\cdot\rho'}V(\rho')\psi(\rho'). \tag{3.1.47}$$

Comparing this equation with the general asymptotic expression (3.1.15) reveals that the scattering amplitude is given in the Born approximation by

$$f(\varphi) = -\frac{m}{2\pi\hbar^2}\int d^2\rho' V(\rho')e^{iq\cdot\rho'}, \tag{3.1.48}$$

where we have introduced the incident wave vector k_i with magnitude k directed along the x-axis, the direction of the incident wave. Note that the wave vector $\hbar\mathbf{q} = \hbar\mathbf{k}_i - \hbar\mathbf{k}_f = \mathbf{p}_i - \mathbf{p}_f$ is just the momentum transferred from the incident beam to the target during the scattering process and that the scattering amplitude is, up to an over all constant, just the Fourier transform of the potential energy with respect to q.

3.2 Scattering theory for 2D Dirac electrons

3.2.1 Partial Wave Method

Equations for the radial functions

Next we concentrate on scattering problem of Dirac electrons by a radially symmetric potential, and calculate the cross section for them to be scattered and deflected by an angle φ. The elastic scattering of quantum relativistic charged particles by radially symmetric potential, V(r), in graphene was studied by Katsnelson and Novikov

[99, 112]. In comparison with the conventional two-dimensional electron gas with impurities [113]. We briefly review the theory in this section. We confine ourselves to massless quasiparticles in monolayer graphene. It is instructive to compare the scattering theory developed in those works with the two-dimensional scattering theory for the Schrodinger equation (Adhikari, 1986). Thus, we will consider the stationary Schrodinger equation

$$H\Psi = E\Psi, \tag{3.2.1}$$

with the two-component spinor wave function

$$\Psi = \begin{pmatrix} \psi_1 \\ \psi_2 \end{pmatrix}, \tag{3.2.2}$$

and the Hamiltonian

$$H = -iv_F\hbar\vec{\sigma}\cdot\nabla + V(r)\hat{\mathbf{1}}. \tag{3.2.3}$$

Here v_F is the velocity of electron in graphene, and V is a potential energy; we will write explicitly the identity matrix $\hat{\mathbf{1}}$ to show the spinor structure of the Hamiltonian. Let us consider the two-dimensional case $V = V(r)$ and $\psi_i = \psi_i(r)$. Equation (3.2.1) now takes the form

$$(-iv_F\hbar\vec{\sigma}\cdot\nabla + V(r)) \begin{pmatrix} \psi_1 \\ \psi_2 \end{pmatrix} = E \begin{pmatrix} \psi_1 \\ \psi_2 \end{pmatrix}, \tag{3.2.4}$$

where the potential $V(r)$ is supposed to be isotropic.

The confinement of electrons in a finite region leads to a discrete energy spectrum. Consider first the simplest case in which L is just a circle, $r = R$, where we pass to the polar coordinates

$$\begin{aligned} x &= r\cos\varphi, \\ y &= r\sin\varphi. \end{aligned} \tag{3.2.5}$$

In these coordinates,

$$i\vec{\sigma}\cdot\nabla = i\begin{pmatrix} 0 & e^{-i\varphi}\left(\frac{\partial}{\partial r}-\frac{i}{r}\frac{\partial}{\partial\varphi}\right) \\ e^{i\varphi}\left(\frac{\partial}{\partial r}+\frac{i}{r}\frac{\partial}{\partial\varphi}\right) & 0 \end{pmatrix}. \tag{3.2.6}$$

Then (3.2.4) can be transform to following equations

$$\begin{aligned} -iv_F\hbar e^{i\varphi}\left(\frac{\partial}{\partial r}+\frac{i}{r}\frac{\partial}{\partial\varphi}\right)\psi_1 + V(r)\psi_2 = E\psi_2, \\ -iv_F\hbar e^{-i\varphi}\left(\frac{\partial}{\partial r}-\frac{i}{r}\frac{\partial}{\partial\varphi}\right)\psi_2 + V(r)\psi_1 = E\psi_1, \end{aligned} \tag{3.2.7}$$

and we can write the two-component wave function below and to try the solution in the following form

$$\begin{aligned} \psi_1(\vec{r}) = g_l(r)e^{il\varphi}, \\ \psi_2(\vec{r}) = f_l(r)e^{i(l+1)\varphi}, \end{aligned} \tag{3.2.8}$$

where $l = 0, \pm1, \pm2, ...$ is the angular-momentum quantum number. Then the Dirac equation, Eq. (3.2.7) reduces to the following set of coupled ordinary differential equations for the radial wave function components

$$\begin{aligned} \frac{dg_l(r)}{dr} - \frac{l}{r}g_l(r) - \frac{i}{\hbar v_F}[E - V(r)]f_l(r) = 0, \\ \frac{df_l(r)}{dr} + \frac{l+1}{r}f_l(r) - \frac{i}{\hbar v_F}[E - V(r)]g_l(r) = 0, \end{aligned} \tag{3.2.9}$$

and to be specific, we will consider further the case of electrons with $E = \hbar v_F k > 0$. In two dimensions, the incident electron plane wave has the expansion

$$e^{i\mathbf{kx}} = e^{ikr\cos\varphi} = \sum_{l=-\infty}^{\infty} i^l J_l(kr)e^{il\varphi}, \tag{3.2.10}$$

where $J_l(kr)$ are the Bessel functions (Whittaker and Watson, 1927). At large values of the argument ($kr >> 1$), they have asymptotics

$$J_l(kr) = \sqrt{\frac{2}{\pi kr}}\cos\Delta_l, \tag{3.2.11}$$

where $\Delta_l = kr - \frac{l\pi}{2} - \frac{\pi}{4}$.

Then, the incident electron plane wave at large values of the argument ($kr >> 1$) has the expansion

$$e^{i\mathbf{kx}} = \sqrt{\frac{2}{\pi kr}} \sum_{l=-\infty}^{\infty} i^l \cos(\Delta_l) e^{il\varphi} = \sqrt{\frac{1}{2\pi kr}} \sum_{l=-\infty}^{\infty} i^l \left(e^{i\Delta_l} + e^{-i\Delta_l}\right) e^{il\varphi}. \tag{3.2.12}$$

The radial Dirac equation (3.2.9) with $V(r) = 0$ will be

$$\begin{aligned} \frac{dg_l(r)}{dr} - \frac{l}{r} g_l(r) - \frac{i}{\hbar v_F} E f_l(r) = 0, \\ \frac{df_l(r)}{dr} + \frac{l+1}{r} f_l(r) - \frac{i}{\hbar v_F} E g_l(r) = 0. \end{aligned} \tag{3.2.13}$$

And substitute one in to the other in Eqs.(3.2.13), we transform the two differential equations of first order into two differential equation of second order:

$$\begin{aligned} [\frac{d^2}{dr^2} - \frac{l}{r}\frac{d}{dr} + k^2 - \frac{l^2}{r^2}] g_l(r) = 0, \\ [\frac{d^2}{dr^2} - \frac{l}{r}\frac{d}{dr} + k^2 - \frac{(l+1)^2}{r^2}] f_l(r) = 0, \end{aligned} \tag{3.2.14}$$

where $k = E/\hbar v_F$, the solutions of Eqs. (3.2.14) can be represented in the form

$$\begin{aligned} g_l(r) = A\left[J_l(kr) + BY_l^1(kr)\right], \\ f_l(r) = \left[AJ_{l+1}(kr) + BY_{l+1}^1(kr)\right], \end{aligned} \tag{3.2.15}$$

where the terms proportional to Bessel (Neumann) functions describe incident (scattering) waves. For a given l, the two independent solutions, which are proportional to the Bessel and Neumann functions, $J_l(kr)$ and $Y_l(kr)$, the latter having the asymptotics ($kr >> 1$)

$$Y_l(kr) = \sqrt{\frac{2}{\pi kr}} \sin \Delta_l, \tag{3.2.16}$$

but the Neumann functions $Y_l(kr)$ are divergent at $r \to 0$. Instead, one can use Hankel functions

$$H_l^{(1,2)}(kr) = J_l(kr) \pm iY_l(kr), \tag{3.2.17}$$

with the asymptotics form of Hankel functions at ($kr >> 1$),

$$H_l^{(1,2)}(kr) = \sqrt{\frac{2}{\pi kr}} \exp\left[\pm i\Delta_l\right]. \tag{3.2.18}$$

Thus, the function H_l^1 describes the scattering wave and H_l^2 describes the wave falling at the centre.

Scattering amplitude and cross section

The scattering theory for the 2D Dirac fermions in the presence of the axially symmetric potential $V(r)$ can be solved as follows. We will express the scattering amplitude and the cross section in terms of the scattering phase shifts for the spinor spherical waves of the form (3.2.2). The relativistic 2D wave function, with the incident flux along the x-direction, has the asymptotic form

$$\Psi \simeq e^{ikx} \begin{pmatrix} 1 \\ 1 \end{pmatrix} + \begin{pmatrix} f_1 \\ f_2 \end{pmatrix} \frac{1}{\sqrt{-ir}} e^{ikr}. \tag{3.2.19}$$

If we assume that the potential perturbation, V (r) depends only on the radial coordinate and that the number of particles are conserved by the potential (the flux of incoming particles is matched by the flux of outgoing), when the potential is sufficient short-ranged (decreasing faster than 1/r), we can represent the solution of Eqs. (3.2.9) in a more conventional way, via scattering phases δ_l (Newton, 1966; Adhikari, 1986).

The ordinary deferential equations for the radial wave function components, (3.2.9), for non zero radially symmetric potential has a solution which are determined via the asymptotics of radial solutions at $kr >> 1$,

$$g_l(kr) \propto \frac{1}{\sqrt{kr}} \cos\left(\Delta_l + \delta_l\right), \tag{3.2.20}$$

$$f_l(kr) \propto \frac{1}{\sqrt{kr}} \sin\left(\Delta_l + \delta_{l+1}\right). \tag{3.2.21}$$

The spinor wave function (3.2.2) is represented in the basis [99, 100, 112]

$$\Psi = \sum_{l=-\infty}^{\infty} A_l \begin{pmatrix} g_l(r)e^{il\varphi} \\ f_l(r)e^{i(l+1)\varphi} \end{pmatrix}, \tag{3.2.22}$$

Rewriting the asymptotic of this component of Eqs. (3.2.20) and (3.2.21) as

$$\begin{aligned} g_l(kr) &= \frac{2}{\sqrt{kr}} \sum_{l=-\infty}^{\infty} A_l \cos(\Delta_l + \delta_l) \\ &= \frac{1}{\sqrt{2kr}} \sum_{l=-\infty}^{\infty} A_l \left(e^{i(\Delta_l+\delta_l)} + e^{-i(\Delta_l+\delta_l)}\right), \end{aligned} \tag{3.2.23}$$

$$\begin{aligned} f_l(kr) &= \frac{2}{\sqrt{kr}} \sum_{l=-\infty}^{\infty} A_l \sin(\Delta_l + \delta_{l+1}) \\ &= \frac{-i}{\sqrt{2kr}} \sum_{l=-\infty}^{\infty} A_l \left(e^{i(\Delta_l+\delta_{l+1})} - e^{-i(\Delta_l+\delta_{l+1})}\right). \end{aligned} \tag{3.2.24}$$

Following from the conservation of particle flux, $A_l = (e^{2i\delta_l(k)} - 1)/2$, defining the partial wave scattering amplitudes. Physically, the incoming component of the spherical wave is undisturbed by the potential while the separate components of the outgoing spherical wave are subject to a set of phase shifts, $\delta_l(k)$. Recast in the form of a perturbation.

Let us calculate now the scattering cross-section. The wave function of a free electron propagating along the x axis i.e the incident wave propagating along the x-axis we have

$$\Psi^{(0)} = \frac{1}{\sqrt{2}} \begin{pmatrix} 1 \\ 1 \end{pmatrix} e^{ikx}, \tag{3.2.25}$$

where the numerical factor provides normalization of the incident current:

$$j_x^{(0)} = [\Psi^{(0)}]^+ \sigma_x \Psi^{(0)} = 1. \tag{3.2.26}$$

Thus, one can choose $A = 1/\sqrt{2}$ in Eq. (3.2.15). Taking into account Eqs. (3.2.15) and (3.2.18), one finds for the asymptotic of the scattering waves at large distances

$$\Psi_{sc} \approx \frac{1}{\sqrt{\pi kr}} \exp\left(ikr - \frac{i\pi}{4}\right) \sum_{l=-\infty}^{\infty} A_l \begin{pmatrix} \exp[i(l+1)\varphi] \\ \exp[il\varphi] \end{pmatrix}. \tag{3.2.27}$$

The current operator in the direction $n = \vec{r}/r$ is

$$\hat{j}_n = \begin{pmatrix} 0 & e^{-i\varphi} \\ e^{-i\varphi} & 0 \end{pmatrix}, \tag{3.2.28}$$

which gives us for the scattering current

$$j^{(sc)} = \Psi_{sc}^{+} \hat{j}_n \Psi_{sc} = \frac{2}{\pi kr} |F(\varphi)|^2, \tag{3.2.29}$$

where

$$F(\varphi) = \sum_{l=-\infty}^{\infty} A_l e^{il\varphi}. \tag{3.2.30}$$

Equation (3.2.29) gives for the differential cross-section

$$\frac{d\sigma}{d\varphi} = \frac{2}{\pi kr} |F(\varphi)|^2. \tag{3.2.31}$$

The Dirac equation (3.2.9) for the massless case has an important symmetry with respect to the replacement $f \leftrightarrow g, l \leftrightarrow -l-1$, which leads to the result

$$A_l(k) = A_{-l-1}(k). \tag{3.2.32}$$

Taking into account Eq. (3.2.32), the equation (3.2.31) can be rewritten in the final form (Katsnelson and A Giem, 2008)[22]

$$\frac{d\sigma}{d\varphi} = \frac{8}{\pi k} \left| \sum_{l=0}^{\infty} A_l \cos\left[(l + \frac{1}{2})\varphi\right] \right|^2. \tag{3.2.33}$$

It follows immediately from Eq. (3.2.33) that $d\sigma/d\varphi = 0$ at $\varphi = \pi$, that is, backscattering is absent. This is in agreement with the general considerations of Section 4.2.

If we have 2D carrier concentration of, n , then, according the standard semiclassical Boltzmann theory (Ziman, 2001; Shon and Ando, 1998), their contribution to the resistivity is

$$\rho = \frac{2}{e^2 v_F^2 N(E_F)} \frac{1}{\tau(k_F)}, \qquad \frac{1}{\tau(k_F)} = n_{imp} v_F \sigma_{tr}, \tag{3.2.34}$$

where $\tau(k_F)$ is the mean-free-path time and v_F and k_F are the Fermi velocity and wavevector (the Fermi wavevector is given by $k_F = (\pi n)^{1/2}$)), $N(E_F)$ is density of states at the Fermi level,

$$\sigma_{tr} = \int_0^{2\pi} d\varphi \frac{d\sigma}{d\varphi}(1 - \cos(\varphi)) \tag{3.2.35}$$

is the transport cross-section. The applicability of the semiclassical Boltzmann theory to quantum relativistic particles in graphene is not clear.

Chapter 4

Electron Scattering in Graphene by impurities with Electric and Magnetic Dipole Moments

4.1 Introduction

The elastic electron scattering in graphene by different type of scatterers has been intensively studied since its experimental discovering ([99] and references there). It is known that the backscattering cross section of massless electrons by the impurities with radially symmetric potentials is equal to zero. But it is not true for the scattering by electric and magnetic dipoles that possess non radially symmetric potentials. Nonzero backscattering can considerably increase the transport cross section that has a much larger effect on current than the small-angle scattering [114].

The electron scattering in graphene has been studied via scattering phases [99, 112] and with the help of 2D Born approximation [112, 115, 116, 117]. It is interesting that there are many different versions of 2D Born approximation proposed including the "self-consistent Born approximation" [118]. Various mechanisms of electron scattering of massless Dirac fermions have been discussed in [22].

To study the electron scattering cross section by electric and magnetic dipoles, we developed our version of the Born approximation for the one layer graphene based on results of [100]. The calculated cross sections are not zero for the backscattering in both cases. Our analysis shows that the scattering by electric dipoles is more efficient than the scattering by magnetic dipoles. But only very large nanomagnetic impurities with gigantic magnetic moments [119] can provide the scattering cross section comparable with that one by the electric dipoles. A comparison of the transport cross sections by Coulomb potential and by electric dipoles shows that they could be comparable.

The chapter is designed as follows. In Section 4.2, we present the Born approximation for the scattering problems on the basis of 2D Dirac like equation of massless electrons. In Section 4.3, we calculate the electron cross section by an impurity with radially symmetric electrostatic potential to compare our result with the known results [112]. In Sections 4.4 and 4.5, we consider the electron scattering by the impurity with electric and magnetic dipole moments, respectively. In Section 4.6, we analyze and compare the obtained transport cross sections. The conclusion (Section 4.7) summarizes the chapter.

4.2 Born approximation

In this Section we try to develop the Born approximation of the Dirac equation in the presence of external field. In doing so, we shall consider cases with a remarkable consequence of the relativistic massless electrons in graphene and the Dirac like equation in crossed magnetic and electric fields, where the magnetic field remains perpendicular to the graphene sheet and the electric field is applied in the plane. The

Hamiltonian of 2D motion of the massless electron in graphene in the external field U can be written as [103]

$$\hat{H} = v_F \hat{\sigma} \cdot (\hat{\mathbf{p}} - \frac{e}{c}\mathbf{A}) + U, \tag{4.2.1}$$

where v_F is the Fermi velocity, $\sigma_x = \begin{pmatrix} 0 & 1 \\ 1 & 0 \end{pmatrix}$ and $\sigma_y = \begin{pmatrix} 0 & -i \\ i & 0 \end{pmatrix}$ are the Pauli matrices, e and c are the electron charge and speed of light in vacuum, respectively; $\hat{\mathbf{p}}$ is 2D momentum operator, $\mathbf{A}$ is the vector potential. The Schrodinger equation corresponding to the Hamiltonian (1)

$$\hat{H}\Psi = E\Psi, \tag{4.2.2}$$

with

$$\Psi = \begin{pmatrix} \psi_1 \\ \psi_2 \end{pmatrix} \tag{4.2.3}$$

can be presented as a system of coupled equations

$$v_F \hat{\pi}_+ \psi_1 = (E - U)\psi_2, \tag{4.2.4}$$

$$v_F \hat{\pi}_- \psi_2 = (E - U)\psi_1, \tag{4.2.5}$$

where ψ_1, ψ_2 are the wave functions,

$$\begin{aligned} \hat{\pi}_\pm &= \hat{p}_\pm - \frac{e}{c}A_\pm, \\ \hat{p}_\pm &= \hat{p}_x \pm i\hat{p}_y, \\ A_\pm &= A_x \pm iA_y, \end{aligned} \tag{4.2.6}$$

with $\hat{p}_x, \hat{p}_y$ and A_x, A_y are the components of the momentum operator and the vector potential, respectively. The wave functions ψ_1 and ψ_2 in the above two-equations can

be written as

$$\psi_2 = \frac{v_F}{(E-U)}\hat{\pi}_+\psi_1, \tag{4.2.7}$$

$$\psi_1 = \frac{v_F}{(E-U)}\hat{\pi}_-\psi_2. \tag{4.2.8}$$

Substitution of ψ_2 from equation (4.2.6) into (4.2.5) and ψ_1 in equation (4..2.7) into (4.2.4) allows one to separate the system of coupled equations as follows;

$$\hat{\pi}_-\frac{1}{(E-U)}\hat{\pi}_+\psi_1 = \frac{E-U}{v_F^2}\psi_1, \tag{4.2.9}$$

$$\hat{\pi}_+\frac{1}{E-U}\hat{\pi}_-\psi_2 = \frac{E-U}{v_F^2}\psi_2. \tag{4.2.10}$$

In the scattering problems we are interested in the solutions of these equations far from the scattering center, where the energy of the incident electrons E is much greater than the average potential energy of the scattering center $\bar{U}$. The Born approximation is valid in this case. And for $|\bar{U}|/E < 1$, equations (4.2.9) and (4.2.10) can be presented as follows

$$\hat{\pi}_-\left\{1+\frac{U}{E}+\frac{U^2}{(E)^2}+...\right\}\hat{\pi}_+\psi_1 = \frac{E^2}{v_F^2}\left(1-\frac{U}{E}\right)\psi_1, \tag{4.2.11}$$

$$\hat{\pi}_+\left\{1+\frac{U}{E}+\frac{U^2}{(E)^2}+...\right\}\hat{\pi}_-\psi_2 = \frac{E^2}{v_F^2}\left(1-\frac{U}{E}\right)\psi_2. \tag{4.2.12}$$

In the scattering problems, the terms containing the vector potential $\mathbf{A}$ and U are being small compared to the energy of electron E. We put them in the right hand side of equations (4.2.11), (4.2.12) keeping only terms linear on U/E and obtain the following equations:

$$\left\{\hat{\pi}_-\hat{\pi}_+ - \frac{E^2}{v_F^2}\right\}\psi_1 = -\left(\hat{\pi}_-\frac{U}{E}\hat{\pi}_+ + \frac{EU}{v_F^2}\right)\psi_1, \tag{4.2.13}$$

$$\left\{\hat{\pi}_+\hat{\pi}_- - \frac{E^2}{v_F^2}\right\}\psi_2 = -\left(\hat{\pi}_+\frac{U}{E}\hat{\pi}_- + \frac{EU}{v_F^2}\right)\psi_2. \tag{4.2.14}$$

Taking into account the explicit expressions of $\hat{\pi}_+$ and $A_\pm$ (see their definitions equation (4.2.6)), one can show that

$$\begin{aligned} \hat{\pi}_-\hat{\pi}_+ &= \hat{p}^2 + \frac{e^2}{c^2}A^2 - \frac{e}{c}[2\mathbf{A}\cdot\hat{\mathbf{p}} + \hbar B_z], \\ [\hat{\pi}_+, \hat{\pi}_-] &= 2\frac{e\hbar}{c}B_z, \end{aligned} \tag{4.2.15}$$

where $B_z = (\nabla \times \mathbf{A})_z$ is the z component of the magnetic field and $[\hat{\pi}_+, \hat{\pi}_-]$ denotes a commutator. Here we chose the Coulomb gauge

$$\nabla \cdot \mathbf{A} = 0. \tag{4.2.16}$$

Using the above equations (4.2.12), (4.2.13) and (4.2.14) we obtain the following;

$$(\nabla^2 + k^2)\psi_1 = \frac{1}{\hbar^2}\left\{\frac{e^2}{c^2}A^2 - \frac{e}{c}[2\mathbf{A}\cdot\hat{p} + \hbar B_z] + \frac{EU}{v_F^2} + \hat{\pi}_-\frac{U}{E}\hat{\pi}_+\right\}\psi_1, \tag{4.2.17}$$

$$(\nabla^2 + k^2)\psi_2 = \frac{1}{\hbar^2}\left\{\frac{e^2}{c^2}A^2 - \frac{e}{c}[2\mathbf{A}\cdot\hat{p} - \hbar B_z] + \frac{EU}{v_F^2} + \hat{\pi}_+\frac{U}{E}\hat{\pi}_-\right\}\psi_2. \tag{4.2.18}$$

We can write the above equations in compressed form as follows for functions $\psi_{1,2}$

$$(\nabla^2 + k^2)\psi_{1,2} = \hat{V}_{1,2}\psi_{1,2}. \tag{4.2.19}$$

Here we introduced the wave vector $k = E/(\hbar v_F)$ and operator

$$\hat{V}_{1,2} = \frac{1}{\hbar^2}\left\{\frac{e^2}{c^2}A^2 - \frac{e}{c}[2\mathbf{A}\cdot\hat{p} \pm \hbar B_z] + \frac{EU}{v_F^2} + \hat{\pi}_\mp\frac{U}{E}\hat{\pi}_\pm\right\}. \tag{4.2.20}$$

It consists of two parts: terms associated with the vector potential $\mathbf{A}$ and the corresponding component of magnetic field B_z transversal to the graphene plane, and terms associated with the potential energy of electron U. It is worth noting that this part of $V_{1,2}$ contains the space derivatives of U. The two equations (4.2.19) are independent and specify the wave functions $\psi_{1,2}$ of electrons belonging to different sublattices of graphene.

At large distances from the scattering center due to the smallness of the operator $\hat{V}_{1,2}$, the functions $\psi_{1,2}$ can be presented as

$$\psi_{1,2} = \psi_{1,2}^{(0)} + \psi_{1,2}^{(1)}, \tag{4.2.21}$$

where $\psi_{1,2}^{(1)}$ are the small corrections to the functions $\psi_{1,2}^{(0)}$, which satisfy equations (4.2.19) with the zeroth right hand side, i.e

$$(\nabla^2 + k^2)\psi_{1,2}^{(0)} = 0. \tag{4.2.22}$$

If the beam of incident electrons propagates along the $x-$ axis, then $\psi_{1,2}^{(0)} = 1/\sqrt{2}\exp(ikx)$. The incident wave function can be written as

$$\Psi_{inc}(x) = \begin{pmatrix} \psi_1^{(0)} \\ \psi_2^{(0)} \end{pmatrix} = \frac{1}{\sqrt{2}} \begin{pmatrix} 1 \\ 1 \end{pmatrix} \exp(ikx), \tag{4.2.23}$$

The factor $1/\sqrt{2}$ provides the normalization of the wave function (4.2.22) to unity. The wave functions $\psi_{1,2}^{(1)}$ satisfy the equations

$$(\nabla^2 + k^2)\psi_{1,2}^{(1)} = \hat{V}_{1,2}\psi_{1,2}^{(0)}. \tag{4.2.24}$$

At large distances from the scattering center, $\psi_{1,2}^{(1)}$ have the form

$$\Psi_{sc} = \begin{pmatrix} \psi_1^{(1)} \\ \psi_2^{(1)} \end{pmatrix} = \frac{\exp(ikr)}{\sqrt{r}} \begin{pmatrix} f_1(\varphi) \\ f_2(\varphi) \end{pmatrix}. \tag{4.2.25}$$

The functions $f_{1,2}(\varphi)$ are analogous to the scattering amplitudes with the scattering angle φ. They have dimension of the square root of length and are controlled by the scattering mechanism.

Let us now consider the differential cross section, the differential scattering cross section is defined as the scattering intensity per unit solid angle per unit incident flux. For the case of graphene where the electrons are confined to a thin sheet, reducing

the dimension from three to two, the 2D differential cross section or the differential cross length is a ratio of the scattered current J_{sc} through the elementary length dl (transversal to the radius vector $\mathbf{r}$) and the incident current J_{inc}

$$d\sigma(\varphi) = \frac{J_{sc}}{J_{inc}} dl. \tag{4.2.26}$$

The incident current is directed along the $x-$ axis and equals to

$$J_{inc} = v_F \Psi^+_{inc} \hat{\sigma}_x \Psi_{inc} = v_F. \tag{4.2.27}$$

The scattered current can be calculated as

$$J_{sc} = \sqrt{J_x^2 + J_y^2}, \tag{4.2.28}$$

where J_x and J_y are the components of the scattered current given by

$$\begin{aligned} J_x &= v_F \Psi^+_{sc} \hat{\sigma}_x \Psi_{sc}, \\ J_y &= v_F \Psi^+_{sc} \hat{\sigma}_y \Psi_{sc}. \end{aligned} \tag{4.2.29}$$

With the help of the wave functions (4.2.25), we obtain

$$\begin{aligned} J_x &= \frac{2v_F}{r} Re[f_1(\varphi)^* f_2(\varphi)], \\ J_y &= \frac{2v_F}{r} Im[f_1(\varphi)^* f_2(\varphi)]. \end{aligned} \tag{4.2.30}$$

The differential cross section (4.2.26) with account of (4.2.27) and (4.2.30) can be presented as

$$\frac{d\sigma(\varphi)}{d\varphi} = 2|f_1(\varphi)^* f_2(\varphi)|. \tag{4.2.31}$$

This formula will be used below for obtaining the cross section of electron scattering in graphene by impurities with nonsymmetric scattering potentials.

4.3 Scattering by impurity with radially symmetric electrostatic potential

Although our main interest will be electron scattering by magnetic and electric dipoles, here we shall briefly consider the electron scattering by impurity with radially symmetric electrostatic potential. We consider this, to see how our equation coincides with the obtained results. Let us begin to calculate the electron scattering cross-section by a nonmagnetic impurity with the radially symmetric electrostatic potential $U(r)$. In this case, operator (4.2.20) with account of $\mathbf{A} = 0$ takes the form

$$\hat{V}_{1,2} = \left(\frac{U}{E} k^2 + \frac{1}{\hbar^2} \hat{p}_{\mp} \frac{U}{E} \hat{p}_{\pm} \right). \tag{4.3.1}$$

It is convenient to use the rectangular coordinate system with the $x-$ axis along the incident electron beam. With account of the explicit form of $\psi^{(0)}_{1,2}$ (4.2.23), equations (4.2.24) can be written as

$$\{\nabla^2 + k^2\} \psi^{(1)}_{1,2} = V_{1,2}(\mathbf{r}) \frac{1}{\sqrt{2}} \exp[ikx], \tag{4.3.2}$$

where

$$V_{1,2}(\mathbf{r}) = \frac{k}{E} [2k + (-i \frac{\partial}{\partial x} \mp \frac{\partial}{\partial y})] U(r). \tag{4.3.3}$$

Now we can use the results [100] of 2D scattering problem and write down $f_{1,2}(\varphi)$ in the following form

$$f_{1,2}(\varphi) = -\frac{1}{4\sqrt{\pi k}} \int \exp(-i\mathbf{q} \cdot \mathbf{r}') V_{1,2}(\mathbf{r}') d^2 r', \tag{4.3.4}$$

where $\hbar\mathbf{q}$ is a transferred momentum under scattering and $V_{1,2}$ is given by (4.3.3).

Integral (4.3.4) can be done presenting $U(r)$ in the form of $2D$ Fourier transform

$$U(r) = \frac{1}{(2\pi)^2} \int U(\mathbf{g}) \exp(i\mathbf{g} \cdot \mathbf{r}) d^2 g. \tag{4.3.5}$$

Substituting (4.3.5) in (4.3.3) and performing integration in (4.3.4) over d^2r', we get $\delta(\mathbf{q}-\mathbf{g})$. Subsequent integration over d^2g gives

$$f_{1,2}(\varphi) = -\frac{U(\mathbf{q})}{4\hbar v_F\sqrt{\pi k}}[2k + q_x \mp iq_y]. \tag{4.3.6}$$

Here $U(\mathbf{q})$ is the Fourier transform of $U(r)$ according to (4.3.5).

In the coordinate system with the $x-$ axis along the wave vector $\mathbf{k}$ of the incident electrons $q_x = -q\sin\varphi/2$, $q_y = q\cos\varphi/2$ (see Fig.4.1). With the help of $q = 2k\sin\varphi/2$, we obtain

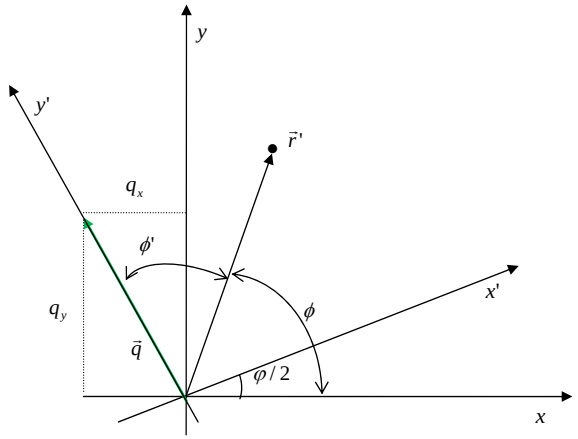

Figure 4.1: The coordinate system x, y (the incident beam electrons is along $x-$ axis) and the coordinate system x', y' (vector $\mathbf{q}$ is along the $y'-$ axis). The projections of $\mathbf{q}$ on axes x and y are $q_x = -q\sin\varphi/2$ and $q_y = q\cos\varphi/2$. The vector $\mathbf{r}$ in coordinate system $x-y$ is vector **r'** in the system $x'.y'$. It is seen that $\phi' + \phi - \varphi/2 = \pi/2$.

$$f_{1,2}(\varphi) = -\frac{U(\mathbf{q})}{4\hbar v_F}\sqrt{\frac{k}{\pi}}(1 + \exp(\mp i\varphi)). \tag{4.3.7}$$

The differential cross section of the electron scattering by the radially symmetric potential $U(r)$ according to (4.2.31) and (4.3.7) takes the form

$$\frac{d\sigma(\varphi)}{d\varphi} = \frac{k|U(\mathbf{q})|^2}{2\pi\hbar^2 v_F^2}\cos^2\varphi/2. \tag{4.3.8}$$

It coincides with corresponding result [112] obtained in a different way. It is clear that the cross section (4.3.8) is equal to zero for the backscattering

$$\frac{d\sigma(\varphi)}{d\varphi}|_{\varphi=\pi} = 0. \tag{4.3.9}$$

Next, we consider the electron scattering in graphene by the impurities with non radially symmetric potentials and show that the backscattering cross section does not equal to zero.

4.4 Scattering by impurity with electric dipole moment

An impurity possessing an electron dipole moment is modeled by a sphere of radius a_e with a built in point dipole d_e. The potential of the electron - dipole interaction in the coordinate system with the $x-$ axis along the incident beam of electrons is given by

$$U = \frac{ed_e}{\rho^3}[x\cos\alpha + y\sin\alpha] = \frac{ed_e}{\rho^2}\cos(\phi - \alpha), \tag{4.4.1}$$

where $\rho = \sqrt{x^2 + y^2}$ is the radius vector of electron, α and ϕ are the angles between the $x-$ axis and dipole moment and vector ρ, respectively.

Further, it will be convenient to use the dimensionless coordinates $r = \rho/a_e$. In this case, we again have to solve equations (4.3.2) for electric dipole potential given by (4.4.1). To do that let first simplify the operator $V_{1,2}$ in the left hand side of equation(4.4.1), which is given by the expression with in (4.3.3).

In view of the geometry of the profiles we consider polar coordinates. This is accomplished by the relations $x \pm iy = re^{\pm i\phi}$, $p_\pm = e^{\pm i\phi}[\partial/\partial r \pm (i/r)\partial/\partial\phi]$. Then we

can write (4.3.3) in the form

$$V_{1,2}(\mathbf{r}) = \frac{k}{E}[2k + (-i\frac{\partial}{\partial r} \mp \frac{1}{r}\frac{\partial}{\partial \phi})]U(r). \tag{4.4.2}$$

Inserting equation(4.4.1) in to (4.4.2), using the dimensionless coordinates $r = \rho/a_e$, we get the following

$$V_{1,2} = i\frac{\bar{k_e}U_0}{2\sqrt{2}Er^3}\left\{-4i\bar{k_e}r\cos(\phi-\alpha) + e^{\mp i\alpha} + 3e^{\mp i(2\phi-\alpha)}\right\}, \tag{4.4.3}$$

where $U_0 = ed_e/a_e^2$ and $\bar{k}_e = ka_e$. This result is obtained with the help of (4.4.1) with account of (4.4.2). The quantities $f_{1,2}$ are given by (4.3.4). The integration in (4.3.4) is convenient to perform in a new coordinate system with the $y'-$ axis along the vector $\mathbf{q}$. It is obtained by anticlockwise rotation of the initial coordinate system x, y by the angle $\varphi/2$. In this system the dot product in the exponent of (4.3.4) becomes $i\bar{q}r'\cos\phi'$, where $\phi' = \pi/2 - (\phi - \varphi/2)$ (see Fig.4.1). Here $\bar{q} = qa_e$.

$$f_{1,2}(\varphi) = -i\frac{U_0}{8\sqrt{2\pi k}\hbar v_F}\int\int \frac{d^2r'}{r'^3}e^{(-i\bar{q}r'\cos\phi')}\left\{-4i\bar{k_e}r'\cos(\phi'-\alpha) + e^{\mp i\alpha} + 3e^{\mp i(2\phi'-\alpha)}\right\}, \tag{4.4.4}$$

$$\begin{aligned} f_{1,2}(\varphi) = -i\frac{U_0}{8\sqrt{2\pi k}\hbar v_F}[-4i\bar{k_e}\int\frac{dr'}{r'}\int_0^{2\pi}d\phi' e^{(-i\bar{q}r'\cos\phi')}\cos(\phi'-\alpha) + \\ e^{\mp i\alpha}\int\frac{dr'}{r'^2}\int_0^{2\pi}d\phi' e^{(-i\bar{q}r'\cos\phi')} + 3e^{\pm i\alpha}\int\frac{dr'}{r'^2}\int_0^{2\pi}d\phi' e^{-i(\bar{q}r'\cos\phi'\pm 2\phi')}], \end{aligned} \tag{4.4.5}$$

The integration over ϕ' in (4.4.5) is carried out with the help of the relation [111]

$$J_n(z) = \frac{i^{-n}}{2\pi}\int_0^{2\pi}d\phi'\exp[i(z\cos\phi' + n\phi')], \tag{4.4.6}$$

where $J_n(z)$ is the first kind Bessel function with an integer n. The subsequent integration over dr' gives the modified bessel functions functions [Appendex D]. The

final result can be written as

$$f_{1,2}(\varphi) = -i\lambda_e\sqrt{\frac{a_e}{\bar{k}}}\{\exp(\mp i\alpha)I_0(\bar{q}) + 4\bar{k}\sin(\varphi/2-\alpha)I_1(\bar{q}) + 3\exp[\pm i(\alpha-\varphi)]I_2(\bar{q})\}, \tag{4.4.7}$$

where $\lambda_e = ed_e\sqrt{\pi}/(4\hbar v_F a_e)$ is dimensionless and we introduced the following denotations

$$\begin{aligned} I_0(\bar{q}) &= \bar{q}\int_{\bar{q}}^{\infty} J_0(z)\frac{dz}{z^2}, \\ I_1(\bar{q}) &= \int_{\bar{q}}^{\infty} J_1(z)\frac{dz}{z}, \\ I_2(\bar{q}) &= \bar{q}\int_{\bar{q}}^{\infty} J_2(z)\frac{dz}{z^2}. \end{aligned} \tag{4.4.8}$$

The lower limit of integrals (4.4.8) is chosen with account of the finiteness of the impurity radius a_e.

The differential cross section of the scattering by electric dipole (4.2.31) with account of (4.4.7) takes the form

$$\begin{aligned} \frac{d\sigma}{d\varphi} = \lambda_e^2\frac{a_e}{\bar{k}}[I_0^2 + 16k^2I_1^2\sin^2(\frac{\varphi}{2}-\alpha) + 9I_2^2 + 8kI_0I_1\sin(\frac{\varphi}{2}-\alpha)\cos\alpha + 6I_0I_2\cos(2\alpha-\varphi) \\ +24kI_1I_2\cos(\varphi-\alpha)\sin(\frac{\varphi}{2}-\alpha)], \end{aligned} \tag{4.4.9}$$

In the case of random orientation of the dipole moments of impurities, (4.4.9) simplifies after averaging over α :

$$\langle\frac{d\sigma}{d\varphi}\rangle = \lambda_e^2\frac{a_e}{\bar{k}}[I_0^2 + 9I_2^2 + 8k^2I_1^2 + 4kI_1\sin\frac{\varphi}{2}(I_0 - I_2)], \tag{4.4.10}$$

Fig.4.2 depicts the differential cross section versus angle for electric dipole scattering. It is interesting to consider what happens when $\varphi = \pi$, Eqs. (4.4.9) and (4.4.10) give a nonzero backscattering cross section. In particular,

$$\langle\frac{d\sigma}{d\varphi}\rangle\,|_{\varphi=\pi} = \lambda_e^2\frac{a_e}{\bar{k}}[I_0^2 + 9I_2^2 + 8k^2I_1^2 + 4kI_1(I_0 - I_2)]. \tag{4.4.11}$$

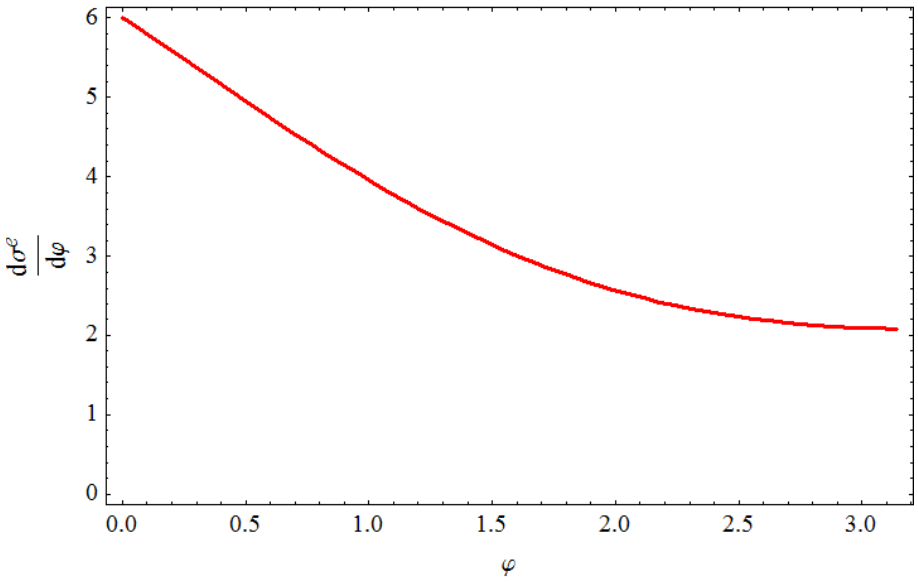

Figure 4.2: Differential cross section versus scattering angle φ for electric dipole potential, and at $\varphi = \pi$, give a nonzero backscattering cross section

It is known from the general theory of scattering [100] that the scattering cross section of fast particles $\bar{k} >> 1$, is relatively small and nonzero only for small scattering angles $\varphi << 1$, when $\bar{q} = 2\bar{k}\sin\varphi/2 \sim 1$. The integrals in (4.4.8) fast decreasing with $\bar{q}$ confirming this property of the scattering. They can be rewritten as

$$\begin{aligned} I_0(\bar{q}) &= J_0(\bar{q}) - \bar{q}I_1(\bar{q}), \\ I_1(\bar{q}) &= 1 - \int_0^{\bar{q}} J_1(z)\frac{dz}{z}, \\ I_2(\bar{q}) &= \bar{q}[\frac{1}{3} - \int_0^{\bar{q}} J_2(z)\frac{dz}{z^2}]. \end{aligned} \tag{4.4.12}$$

The first relation of (4.4.12) is obtained by integration of I_0 (4.4.8) by parts and using $J_1(z) = -dJ_z/dz$. The second and third relations obtained with the help of $\int_{\bar{q}}^{\infty} J_1(z)dz/z = 1 - \int_0^{\bar{q}} J_1(z)dz/z$ and $\int_{\bar{q}}^{\infty} J_2(z)dz/z^2 = 1/3 - \int_0^{\bar{q}} J_2(z)dz/z^2$. For $\bar{q} << 1$, the integration in (4.4.12) can be performed with the help of power series

expansion of the Bessel function [111]

$$J_n(z) = \sum_{s=0}^{\infty} \frac{(-1)^s}{s!(n+s)!} \left(\frac{z}{2}\right)^{n+2s}. \tag{4.4.13}$$

Keeping the terms up to $\bar{q}^2$ in (4.4.13), we obtain

$$\begin{aligned} I_0(\bar{q}) &= 1 - \bar{q} + \frac{\bar{q}^2}{2^2} + ..., \\ I_1(\bar{q}) &= 1 - \frac{\bar{q}}{2} + ..., \\ I_2(\bar{q}) &= \frac{\bar{q}}{3} - \frac{\bar{q}^2}{2^3} + ... \end{aligned} \tag{4.4.14}$$

Substituting these expansions in (4.4.10), we get

$$\langle \frac{d\sigma}{d\varphi} \rangle = \lambda_e^2 \frac{a_e}{\bar{k}} \{1 + \frac{2}{3}(ka_e)^2[5 + 7\cos^2\frac{\varphi}{2}]\}. \tag{4.4.15}$$

It is seen that the differential cross section (4.4.15) for slow electrons $ka_e << 1$ is practically isotropic and inversely proportional to the wave vector k of the incident electrons.

4.5 Scattering by impurity with magnetic dipole moment

We now turn our attention to the interaction between the electron and the magnetic dipole moment. An electron moving in the magnetic field $\mathbf{B}$ of the magnetic impurity described by the vector potential $\mathbf{A}$ is subjected to the Lorentz force acting on its charge. This interaction is described by the first and second terms in operator (4.2.20). The magnetic field also interacts with the intrinsic magnetic moment of electron $\mathbf{m}_e$, which is described by the potential

$$U = -\mathbf{m}_e \cdot \mathbf{B}, \tag{4.5.1}$$

where $|\mathbf{m}_e| = \mu_B$ is the Bohr magneton. It enters in the last two terms of (4.2.20).

Let us model the magnetic impurity by a sphere of radius a_m with a built in point magnetic moment $\mathbf{d}_m$. The vector potential of the dipole magnetic field is

$$\mathbf{A} = \frac{1}{a_m^2}\frac{\mathbf{d}_m \times \mathbf{r}}{r^3}. \tag{4.5.2}$$

Here we again use the dimensionless coordinate r and measure the distance in units of a_m. The vector potential of the magnetic dipole transversal to the graphene plane has two components

$$A_x = -\frac{d_m}{a_m^2}\frac{y}{r^3},\ A_y = \frac{d_m}{a_m^2}\frac{x}{r^3}. \tag{4.5.3}$$

The vector potential (4.5.2) satisfies the condition of the Coulomb gauge (4.2.16). The magnetic field of the dipole $\mathbf{B} = \nabla \times \mathbf{A}$ has only one nonzero component B_z

$$B_z = -\frac{d_m}{a_m^2 r^3}. \tag{4.5.4}$$

To find $f_{1,2}(\varphi)$ that control the scattering cross section, it is necessary to specify the operator $\hat{V}_{1,2}$ (4.2.20) in equations (4.2.24). With account of (4.5.3) and (4.5.4) after ignoring small terms proportional A^2 and U, we get

$$\hat{V}_{1,2}(\mathbf{r}) = -\frac{\lambda_1}{r^3}[2\hat{L}_z \pm 1], \tag{4.5.5}$$

where $\lambda_1 = ed_m/(a_m c\hbar)$ is the dimensionless coupling parameter and $\hat{L}_z = i(y\partial/\partial x - x\partial/\partial y)$ is z projection of the dimensionless angular momentum operator. Equation (4.3.4) contains $V_{1,2}$ that is obtained by acting operator (4.5.5) on the wave functions (4.2.23). The result reads

$$V_{1,2}(\mathbf{r}) = \frac{\lambda_1}{r^3\sqrt{2}}[2y\bar{k} \mp 1]. \tag{4.5.6}$$

The integrals (4.3.4) in this case take the form

$$f_{1,2}(\varphi) = -\frac{\lambda_1\sqrt{a_m}}{4\sqrt{\pi\bar{k}}}\int \exp(-i\bar{\mathbf{q}}\mathbf{r}')\times[2\bar{k}y' \mp 1]\frac{d^2r'}{r'^3}. \tag{4.5.7}$$

Here $\bar{q} = qa_m$ is the dimensionless transferred momentum.

The integration in (4.5.7) is performed in the same coordinate system as in the previous section with the $y'-$ axis along the vector $\mathbf{q}$. (see Fig.4.1). Passing to the cylindrical coordinates r', ϕ' with $y' = r'\cos(\phi' - \varphi/2)$, we rewrite (4.5.7) as follows

$$f_{1,2}(\varphi) = -\frac{\lambda_1\sqrt{a_m}}{4\sqrt{\pi\bar{k}}}\int_1^\infty \frac{dr'}{r'^2}\int_0^{2pi} \exp(-i\bar{q}r'cos\phi')[2\bar{k}r'\cos\phi'\cos\varphi/2 \mp 1]. \tag{4.5.8}$$

The term with $\sim \sin\phi'\sin\varphi/2$ gives no contribution to integral (4.5.8). The integration over r' is taken from 1 (in the dimension coordinates it corresponds to integration from a radius a of the manomagnet). Acting in same manner as in the previous section, we obtain

$$f_{1,2}(\varphi) = \frac{\lambda_1}{2}\sqrt{\frac{a_m\pi}{\bar{k}}}[2i\bar{k}\cos\frac{\varphi}{2}I_1(\bar{q}) \pm I_0(\bar{q})], \tag{4.5.9}$$

where $I_0(\bar{q})$ and $I_1(\bar{q})$ are given by the first two expressions of (4.4.12).

With the help of (4.2.31) and (4.5.9), we obtain the differential cross-section of electron scattering by the magnetic impurity

$$\frac{d\sigma(\varphi)}{d\varphi} = \lambda_m^2\frac{a_m}{\bar{k}}[4I_1^2(\bar{q})\bar{k}^2\cos^2\frac{\varphi}{2} + I_0^2(\bar{q})]. \tag{4.5.10}$$

Here we introduced $\lambda_m = ed_m\sqrt{\pi}/(2a_mc\hbar)$ to be consistent with the previous section. From (4.5.10) one can see that the backscattering cross section

$$\frac{d\sigma(\varphi)}{d\varphi}|_{\varphi=\pi} = \lambda_m^2\frac{a_m}{\bar{k}}I_0^2(2), \tag{4.5.11}$$

is not equal to zero.

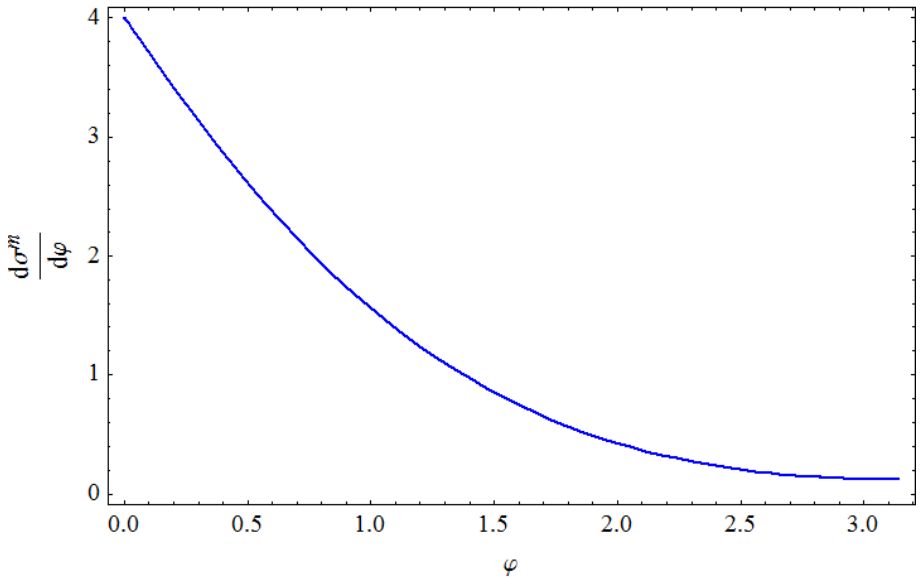

Figure 4.3: Differential cross section versus scattering angle φ for magnetic potential, and at $\varphi = \pi$, gives a nonzero backscattering cross section

From Fig 4.3 we can see that the differential cross section versus angle φ. The electron scattering by magnetic impurities may be important for the slow electrons $\bar{k} = ka_m << 1$. For the fast electrons $\bar{k} >> 1$ this type of scattering gives negligible contribution. To see the dependence of cross-section (4.5.10) on φ in the limit $\bar{k} << 1$, we use the first two relations of (4.4.14). The result reads

$$\frac{d\sigma(\varphi)}{d\varphi} = \lambda_m^2 \frac{a_m}{\bar{k}} \{1 - 4\bar{k} \sin \varphi/2 + 2\bar{k}^2[2 + \sin^2 \varphi/2]\}. \tag{4.5.12}$$

The cross section (4.5.12) comparing with cross section (4.4.15) contains linear term $\sim \bar{k} = ka_m$. For very slow electrons $ka_m << 1$, it is practically isotropic as (4.4.15).

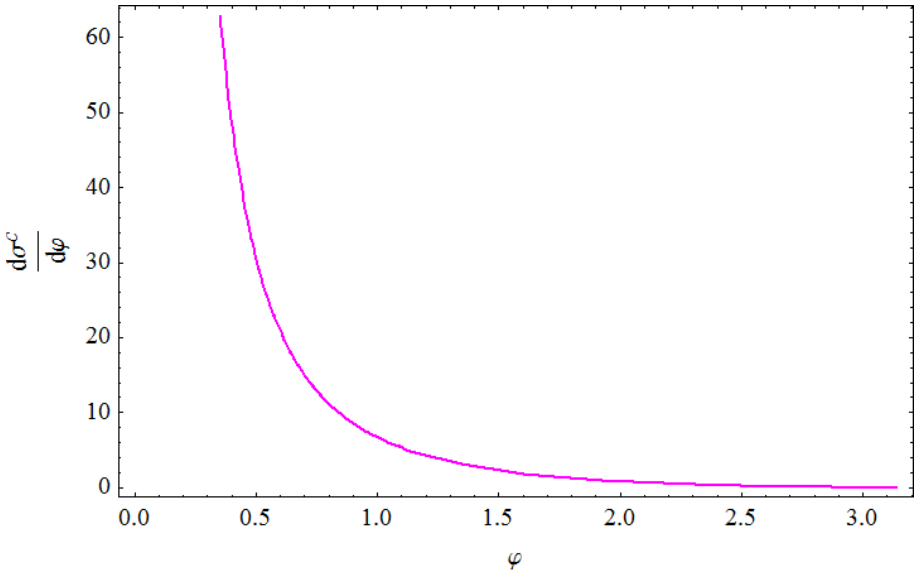

Figure 4.4: Differential cross section versus scattering angle φ for coulomb potential, and at $\varphi = \pi$, give a nonzero backscattering cross section

4.6 Transport cross section

The transport cross section or transport scattering length in 2D problems is the quantity which controls the collision time that enters in all kinetic coefficients. It is given by the relation (3.2.35)

$$\sigma_{tr} = \int_0^{2\pi} (1 - \cos\varphi) \frac{d\sigma}{d\varphi} d\varphi. \tag{4.6.1}$$

For slow electrons, it can be obtained analytically by substitution of (4.4.15) and (4.5.12) into (4.6.1) and integration over $d\varphi$. The transport cross sections by the electric and magnetic dipoles are given by

$$\sigma_{tr}^{(e)} = \lambda_e^2 \frac{2\pi a_e}{\bar{k}} \{1 + \frac{9}{2}\bar{k}^2\} \tag{4.6.2}$$

and

$$\sigma_{tr}^{(m)} = \lambda_m^2 \frac{\pi a_m}{\bar{k}} [1 - 4\bar{k}\sin\varphi/2 + 2\bar{k}^2(2 + \sin^2\varphi/2)]. \tag{4.6.3}$$

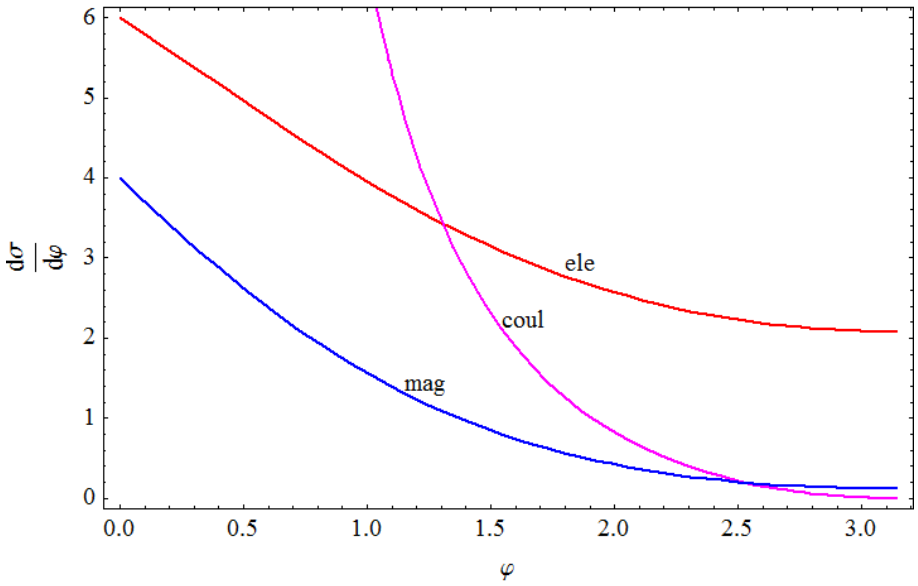

Figure 4.5: Compare the differential cross section by electric dipole (curve "ele"), electric charge (curve "coul"), and magnetic dipole (curve "mag") versus scattering angle φ.

The ratio of these quantities in the limit $\bar{k} = ka_{e,m} << 1$ is equal to

$$\frac{\sigma_{tr}^{(e)}}{\sigma_{tr}^{(m)}} = \frac{1}{2}\{\frac{c}{v_F}\frac{d_e}{d_m}\frac{a_m}{a_e}\}^2. \tag{4.6.4}$$

The large ratio $c/v_F \approx 300$ results in that the transport cross section of electric dipoles always dominates over the transport cross section of magnetic dipoles.

Even the nanomagnet impurities with the gigantic magnetic dipole moments cannot change the sign of inequality

$$\frac{\sigma_{tr}^{(e)}}{\sigma_{tr}^{(m)}} >> 1. \tag{4.6.5}$$

We can estimate the magnetic moment of these nanoinclusions as $d_m = Nn\mu_B 4\pi a_m^3/3$ (where N is a number of Bohr magnetons μ_B per atom, $n = 10^{22}cm^{-3}$ is the density number of atoms of nanomagnet). Taking a number $N = 10$ [119] and $a_m = \kappa 10^{-7}cm$,

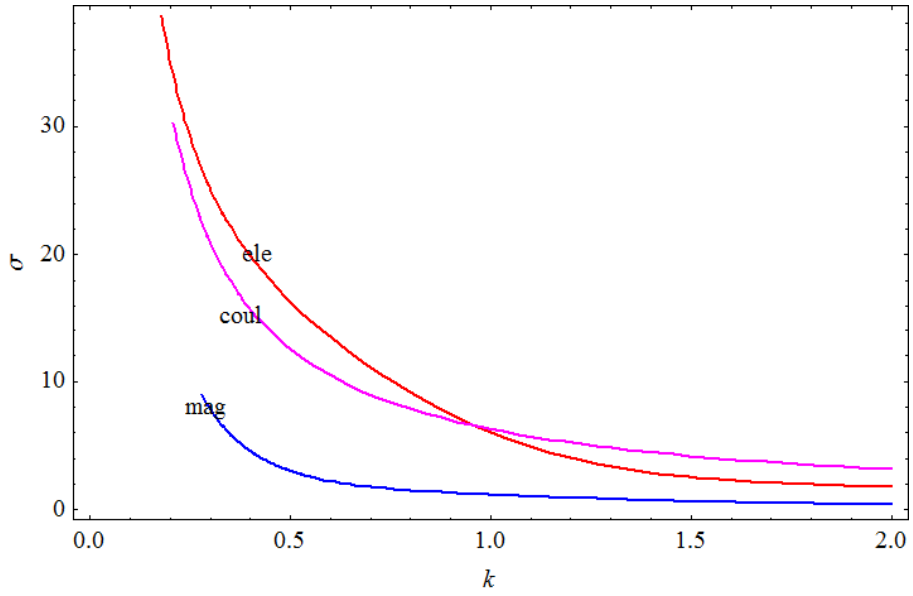

Figure 4.6: The electron transport cross section by electric dipole (curve "ele"), electric charge (curve "coul"), and magnetic dipole (curve "mag") versus dimensionless wave vector $\bar{k}$.

(κ the radius of nanomagnet in nm)and $\mu_B = 10^{-20}$, we get $d_m \approx \kappa^3 10^{-18}$. The typical value of the electric dipole moment is $d_e = 10^{-18}$ and we set $a_e = 10^{-8} cm$. With these parameters, we get

$$\sigma_{tr}^{(e)}/\sigma_{tr}^{(m)} = 50[c(v_F\kappa^2)] >> 1, \tag{4.6.6}$$

even for the large nanomagnets of the order of $10nm$.

It would be interesting to compare the transport cross sections of electric dipoles and charged impurities. The latter is formed by the Coulomb scattering potential $U(r) = -Ze^2/r$. For evaluation we neglect the screening effects. The Fourier component of $U(r)$ in 2D case is $U(\mathbf{q}) = -(\pi Ze^2/k)\sin\varphi/2$. According to (4.3.8), the electron differential cross section is

$$\frac{d\sigma^{(c)}}{d\varphi} = \frac{\pi Z^2 e^4}{2\hbar^2 v_F^2 k}\cot^2\varphi/2. \tag{4.6.7}$$

The corresponding transport cross section is obtained by substitution (4.6.7) into (4.6.1). After integration over $d\varphi$ we get

$$\sigma_{tr}^{(c)} = \frac{\lambda_c^2}{k}, \tag{4.6.8}$$

where $\lambda_c = \pi Z e^2/(\hbar v_F)$. Comparing (4.6.2) for $ka_e << 1$ and (4.6.8), we get

$$\frac{\sigma_{tr}^{(c)}}{\sigma_{tr}^{(e)}} = 4\pi Z^2 \frac{ea_e}{d_e}. \tag{4.6.9}$$

If $Z = 1$ and $ea_e = d_e$ then the ratio of the transport cross sections of charged and polar impurities for slow electrons is 4π.

For not so slow electrons $ka_{e,m} \leq 1$, the differential cross sections (4.4.10) and (4.5.10) and corresponding transport cross sections can be analyzed numerically. In Fig.2, we present the normalized transport cross sections $\sigma_{tr}^{(c,e,m)}$ divided by $\lambda_c^2 a_e, \lambda_e^2 2\pi a_e, \lambda_m^2 \pi a_m$, respectively, versus $\bar{k}$. These curves are denoted by letters $coul, ele, mag$. It is seen that $\sigma_{tr}^{(c)}$ and $\sigma_{tr}^{(e)}$ are comparable for $0.25 < \bar{k} < 1$. This allows us to claim that the electron scattering by the impurities with electric dipoles must be taken into account while analyzing the electron mobility in graphene.

4.7 Conclusion

The analysis of the electron scattering by the impurities with electric and magnetic dipole moments in graphene has shown the electric dipoles are more effective scatterers even compared with nanomagnet impurities with gigantic magnetic moments. The electron transport cross section of the polar impurities can be comparable with the transport cross section of charged scatterers with the symmetric Coulomb potential. The reason of this is that the backscattering cross section of electrons by polar

impurities is different from zero. The polar impurities are widespread and can affect the electron mobility in graphene along with the charged impurities.

In this chapter, we consider the magnetic impurities with magnetic moment transversal to the graphene plane. In this case the dominant interaction of an electron with the magnetic field of the dipole is described by the vector potential $\mathbf{A}$ in (4.2.20) and spin independent. However, the electron - magnetic dipole interaction U (4.5.1) is spin dependent. It can be important for the magnetic dipoles parallel to the graphene plane. In this case, instead of two component electron wave function (4.2.3), we deal with the four component wave function that is dictated by two possible electron spin orientations. The electron scattering cross section is spin dependent. The problem of electron spin dependent scattering by nanomagnets in 2DEG has been studied in [120]. Our preliminary calculations of the scattering cross section by the nanomagnets located over the graphene plane shows its anisotropy with respect to the spin orientation.

Chapter 5

Electron Scattering in Graphene by Remote Nanomagnet

5.1 Introduction

It is known that the electron scattering by charged impurities in graphene is dominant over all other mechanisms scattering but does not considerably affects the very high mobility of charge carriers in graphene [99]. The electron scattering in graphene by impurities with electric and magnetic dipoles have been studied in chapter 4 with the help of the modified Born approximation. It was shown that the non symmetric scattering potential of these impurities causes the nonzero backscattering cross sections. The scattering effects of the magnetic dipoles is negligible due to the comparative smallness of magnetic moments of natural atoms and molecules.

Modern technology enables to manufacture nanomagnets with anomalous magnetic moments that reportedly can be more than 10 Bohr magnetons per atom of the nanomagnet [122, 123]. In this chapter, we consider the elastic electron scattering in graphene by the nonhomogeneous magnetic field of remote nanomagnets with gigantic magnetic moments with the help of the Born approximation. The remote

nanomagnets can support the graphene plane or can be suspended above it and do not produce any deformations. The magnetic field of these nanomagnets is modeled by point dipoles and can be rather large up to $0.1T$. The nanomagnets with gigantic magnetic moments and considerably affect transport properties of electrons in graphene.

The chapter is tailored as follows. In the second Section, we formulate the problem and present the main equations. The third and fourth Sections are devoted to obtaining the electron scattering cross sections by remote magnetic dipoles perpendicular and parallel to graphene plane and their numerical simulation. The conclusion summarizes the results of the chapter.

5.2 Main equations

In this Section we briefly describe the main equations of chapter 4. The Schrodinger equation of the massless electron of graphene in an external magnetic field can be written as

$$v_F \hat{\sigma} \cdot (\hat{p} - \frac{e}{c}\mathbf{A}) \begin{pmatrix} \psi_1 \\ \psi_2 \end{pmatrix} = E \begin{pmatrix} \psi_1 \\ \psi_2 \end{pmatrix}, \tag{5.2.1}$$

where v_F is the Fermi velocity, $\hat{\sigma} = (\hat{\sigma}_x, \hat{\sigma}_y)$ are the Pauli matrices, $\hat{p}$ is 2D momentum operator, $\mathbf{A}$ is the vector potential; e and c are the electron charge and the speed of light in vacuum, respectively. The functions ψ_1 and ψ_2 describe the electron in states related to the two sublattices of graphene and satisfy to the following coupled equations

$$\begin{aligned} v_F \hat{\pi}_+ \psi_1 &= E\psi_2, \\ v_F \hat{\pi}_- \psi_2 &= E\psi_1, \end{aligned} \tag{5.2.2}$$

where $\hat{\pi}_\pm = \hat{p}_\pm - eA_\pm/c$, $\hat{p}_\pm = \hat{p}_x \pm i\hat{p}_y$, $A_\pm = A_x \pm iA_y$, where $\hat{p}_x, \hat{p}_y$ and A_x, A_y are the components of the momentum operator and the vector potential, respectively, E is the electron eigen energy.

Substituting ψ_2 from the first equation (5.2.2) into the second one and vice versa, we obtain the following independent Helmholtz type equations for ψ_1 and ψ_2

$$(\nabla^2 + k^2)\psi_{1,2} = \hat{V}_{1,2}\psi_{1,2}, \tag{5.2.3}$$

where we introduced the wave vector $k = E/(\hbar v_F)$ and the operator

$$\hat{V}_{1,2} = \frac{1}{\hbar^2}\left\{\frac{e^2}{c^2}A^2 - \frac{e}{c}[2\mathbf{A}\cdot\hat{p} \pm \hbar B_z]\right\}. \tag{5.2.4}$$

At large distances from the scattering center, the left hand side of (5.2.3) is small that allows us to seek its solution in the form

$$\psi_{1,2} = \psi_{1,2}^{(0)} + \psi_{1,2}^{(1)}, \quad \psi_{1,2}^{(1)} << \psi_{1,2}^{(0)}. \tag{5.2.5}$$

The wave functions $\psi_{1,2}^{(0)}$ describe the incident wave and satisfy the homogeneous equation (5.2.5). We chose them in the form of plane waves propagating along the $x-$axis

$$\psi_{1,2}^{(0)} = \frac{1}{\sqrt{2}}\exp(ikx). \tag{5.2.6}$$

The factor $1/\sqrt{2}$ provides the unit normalization of the incident wave function

$$\psi_{inc} = \frac{1}{\sqrt{2}}\begin{pmatrix} 1 \\ 1 \end{pmatrix}\exp(ikx). \tag{5.2.7}$$

Substituting (5.2.6) in (5.2.3) with account of (5.2.5) and the explicit form of operator (5.2.4), we obtain the equations for the scattered wave functions $\psi_{1,2}^{(1)}$

$$(\nabla^2 + k^2)\psi_{1,2}^{(1)} = V_{1,2}\psi_{1,2}^{(0)} \tag{5.2.8}$$

where

$$V_{1,2} = \frac{1}{\hbar^2}\left\{\frac{e^2}{c^2}A^2 - \frac{e\hbar}{c}[2A_x k \pm B_z]\right\}. \tag{5.2.9}$$

The scattered wave functions $\psi^{(1)}_{1,2}$ at large distances from the scattering center have the form chapter 4

$$\psi^{(1)}_{1,2} = f_{1,2}(\varphi)\frac{\exp(ikr)}{\sqrt{r}}, \tag{5.2.10}$$

where $f_{1,2}(\varphi)$ are the scattering amplitudes and φ is the scattering angle. The asymptotic solutions of (5.2.8) allows one to single out the scattering amplitudes from the solutions of (5.2.9) Chapter 4

$$f_{1,2}(\varphi) = -\frac{1}{4\sqrt{\pi k}}\int \exp(-i\mathbf{q}\cdot\mathbf{r})V_{1,2}(r)d^2r, \tag{5.2.11}$$

where $\mathbf{q}$ is a wave vector transferred to the electron under the elastic scattering $q = 2ksin\varphi/2$. The differential scattering cross section is given by (4.2.31)

$$\frac{d\sigma(\varphi)}{d\varphi} = 2|f_1^*(\varphi)f_2(\varphi)| = 2|f_1||f_2|. \tag{5.2.12}$$

Next we obtain the components of $\mathbf{A}$ and B_z entering in $V_{1,2}$ (5.2.9). Let us model

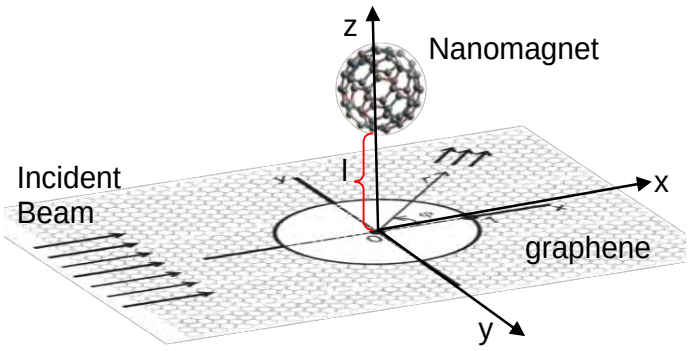

Figure 5.1: Electron scattering by large gigantic nanomagnet suspended above the graphene plane

the nanomagnet by a sphere of radius a with built in the point magnetic dipole $\mathbf{d}$.

Let it be located at the point $(0, 0, l \geq a)$ above the graphene plane $(x, y, 0)$ (See Fig.5.1). The vector potential and the corresponding magnetic field of the dipole can be obtained with the help of the known formulas

$$\mathbf{A} = \frac{\mathbf{d} \times \mathbf{R}}{R^3}, \quad \mathbf{B} = \frac{3(\mathbf{d} \cdot \mathbf{R})\mathbf{R} - R^2\mathbf{d}}{R^5}. \tag{5.2.13}$$

Here R is a distance from the dipole to the observation point. To find the vector potential and the magnetic field in the graphene plane one has to specify the orientation of $\mathbf{d}$ with respect to the graphene plane and set $z = l$ in (5.2.13).

In this Section, we consider the magnetic dipoles transversal and parallel to the graphene plane. It will be convenient to use the dimensionless coordinates and measure a distance in units l.

If the dipole transverse to the graphene plane $\mathbf{d} = (0, 0, d)$, we get from (5.2.13) the following components of $\mathbf{A}$ and B_z

$$\begin{aligned} A_x &= -\frac{d}{l^2}\frac{y}{\bar{R}^3}, \quad A_y = \frac{d}{l^2}\frac{x}{\bar{R}^3}, \quad A_z = 0, \\ B_z &= \frac{d}{l^3}\frac{2 - r^2}{\bar{R}^5}, \end{aligned} \tag{5.2.14}$$

Fig.5.2 shows vector potential and magnetic field for dipole perpendicular to graphene plane.

If the magnetic moment is parallel to the graphene plane, we get

$$\begin{aligned} A_x &= \frac{d}{l^2}\frac{\sin\alpha}{\bar{R}^3}, \quad A_y = -\frac{d}{l^2}\frac{\cos\alpha}{\bar{R}^3}, \\ A_z &= \frac{d}{l^2}\frac{y\cos\alpha - x\sin\alpha}{\bar{R}^3}, \quad B_z = 3\frac{d}{l^3}\frac{x\cos\alpha + y\sin\alpha}{\bar{R}^5}. \end{aligned} \tag{5.2.15}$$

Here $\bar{R} = \sqrt{1 + r^2}, r^2 = x^2 + y^2$ are dimensionless and the distance R related to $\bar{R}$ as $R = l\bar{R}$; α is an angle between $\mathbf{d}$ and the $x-$ axis. Fig.5.3 depicts the vector potential and magnetic field for dipole parallel to graphene plane.

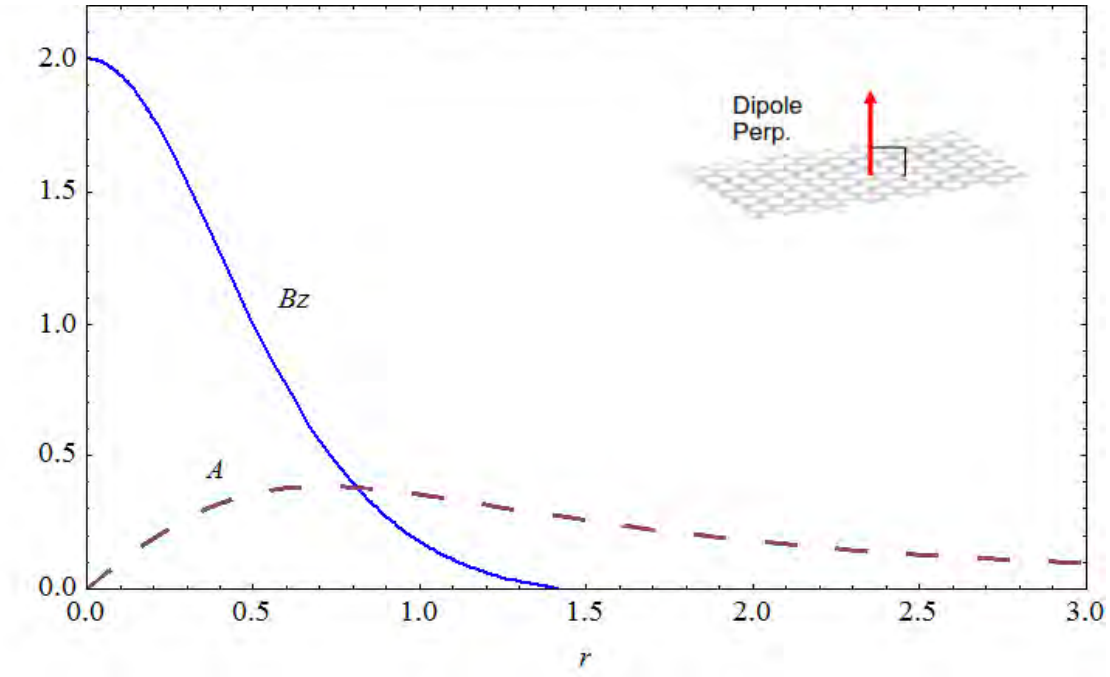

Figure 5.2: The radial component of vector potential (Pink dash curve), and perpendicular magnetic field(Blue solid curve)as functions of the radial coordinate for magnetic dipole is transversal to graphene plane Eq(5.2.14).

5.3 Scattering by magnetic dipole transverse to graphene plane

To find the scattering amplitudes $f_{1,2}(\varphi)$ according to (5.2.11), we have to substitute (5.2.9) with $\mathbf{A}$ and B_z given by (5.2.14). In the defined dimensionless coordinates we get

$$V_{1,2} = \frac{\lambda}{\bar{R}^3}\left\{\frac{\lambda r^2}{\bar{R}^3} + [2\bar{k}y \mp \frac{2-r^2}{\bar{R}^2}]\right\}, \tag{5.3.1}$$

where $\bar{k} = kl$ is the dimensionless wave vector of the electron and

$$\lambda = ed/(c\hbar l) \tag{5.3.2}$$

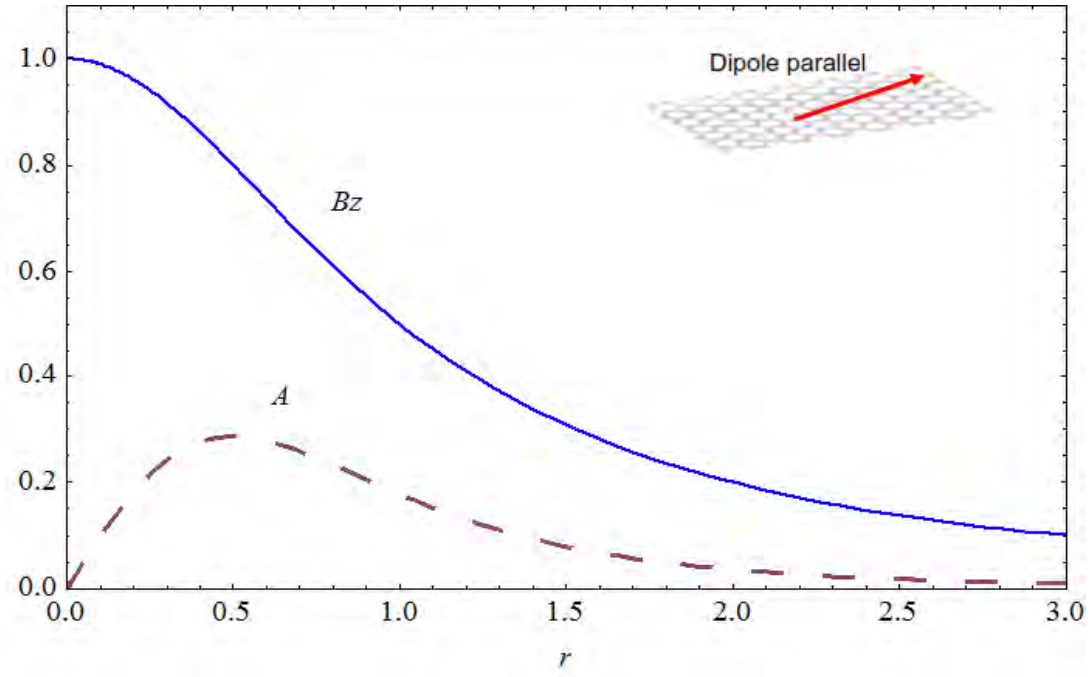

Figure 5.3: The radial component of vector potential (Pink dash curve), and perpendicular magnetic field(Blue solid curve)as functions of the radial coordinate for magnetic dipole is parallel to graphene plane Eq(5.2.15).

is the dimensionless coupling constant. Let us estimate its numeric value. The magnetic moment of a spherical nanomagnet of the radius a is

$$d = \frac{4\pi}{3}\mu_B a^3 n N, \tag{5.3.3}$$

where N is a number of the Bohr magnetons μ_B per one atom of the nanomagnet material and n is its density number. Taking the numerical value $\mu_B = 10^{-20} Gs\ cm^3$ and $n = 10^{22}$, we get an evaluation

$$\lambda \sim 7 \times 10^{-5} N \frac{a}{l} a^2, \tag{5.3.4}$$

where a and l must be in nanometers. It is reported that $10 < N < 100$ [122, 123]. Let $N = 10$. One can see that for $a = 10nm$ nanomagnets suspended over the

graphene plane at a distance of the same order, $\lambda \sim 10^{-2}$. In this case, we can neglect in (5.3.1) the term $\sim \lambda^2$, as it done in Chapter 4. But for "larger" nanomagnets $40 \leq a \leq 10^2 nm$, we can easily get $0.1 \leq \lambda \leq 1$. In this case, the term $\sim A^2$ in (5.2.9) must be taken into account. One more possibility to increase λ is to arrange nanomagnets from the both sides of the graphene plane.

The maximum magnetic field created by a nanomagnet according to (5.2.14), (5.2.15), and (5.3.3) is

$$B \sim \mu_B \frac{a^3}{l^3} nN. \tag{5.3.5}$$

This formula shows that the magnetic field of the remote magnetic dipole fast decreases with l. For $l \sim a$ and the numeric values of the parameters in (5.3.5) as above, we obtain that $B \sim 10^3 Gs = 0.1T$.

Now we calculate the scattering amplitudes $f_{1,2}(\varphi)$ in the case under consideration. Let us substitute (5.3.1) into (5.2.11), which we rewrite in the dimensionless coordinates, and obtain

$$\begin{aligned} f_{1,2}(\varphi) = -\frac{\lambda}{4}\sqrt{\frac{l}{\pi \bar{k}}} \int_0^\infty dr' \int_0^{2\pi} d\phi' \exp(-i\bar{q} r' \cos\phi') \\ \times \left\{ \frac{\lambda r'^3}{R'^6} + 2\frac{\bar{k} r'^2 \cos(\phi' - \varphi/2)}{R'^3} \mp \frac{2r' - r'^3}{R'^5} \right\}. \end{aligned} \tag{5.3.6}$$

Here $R' = \sqrt{1 + r'^2}$ and $\bar{q} = 2\bar{k} \sin\varphi/2$ is the dimensionless transferred wavevector. Integration in (5.3.6) is carried out in the x', y' coordinate system. With the vector $\bar{\mathbf{q}}$ is along the y' axis, where $\bar{\mathbf{q}} \cdot \mathbf{r}' = \bar{q} r' \cos\phi'$. The coordinate system x', y' is obtained by anti clockwise rotation of the initial x, y coordinate system by the angle $\varphi/2$. We substitute in the integrand $y' = r' \cos(\phi' - \varphi/2)$. Integration over ϕ' gives the Bessel functions according to the known relation [111]

$$\int_0^{2\pi} d\phi' \exp[i(z cos\phi' + n\phi')] = 2i^n \pi J_n(z), \tag{5.3.7}$$

where $J_n(z)$ is the Bessel function with an integer n. While integrating (5.3.6) over r' we obtain the following integrals

$$I_{nm}^{(p)}(q) = \int_0^\infty J_n(qr)\frac{r^p dr}{(1+r^2)^{m/2}}. \tag{5.3.8}$$

They can be calculated in the closed form (see Appendix D). Presenting the numerator of (5.3.8) as $r^p = (1+r^2-1)r^{p-2}$, one can obtain that

$$I_{nm}^{(p)}(\bar{q}) = I_{n\ m-2}^{(p-2)}(\bar{q}) - I_{nm}^{(p-2)}. \tag{5.3.9}$$

With the help of (5.3.8) and (5.3.9) we present the scattering amplitudes (5.3.6) as

$$f_{1,2}(\varphi) = -\frac{\lambda}{2}\sqrt{\frac{\pi l}{\bar{k}}}\left\{I_{\pm}(\bar{q}) + 2i\bar{k}I_{13}^{(2)}(\bar{q})\cos\varphi/2\right\}, \tag{5.3.10}$$

where $I_{\pm}(\bar{q}) = \lambda I_{06}^{(3)}(\bar{q}) \pm [2I_{05}^{(1)}(\bar{q}) - I_{05}^{(3)}(\bar{q})]$.

The differential cross section (5.2.12) with account of (5.3.10) and (39) of the Appendix D can be presented as

$$\begin{aligned}\frac{1}{L}\frac{d\sigma(\varphi)}{d\varphi} &= \bar{k}\{A_+^2\sin^2\varphi/2 + \exp(-2\bar{q})\cos^2\varphi/2\}^{1/2} \\ &\times \{A_-^2\sin^2\varphi/2 + \exp(-2\bar{q})\cos^2\varphi/2\}^{1/2},\end{aligned} \tag{5.3.11}$$

where $L = 2\pi\lambda^2 l$ is a quantity having dimension of length and $A_\pm = \lambda[K_1(\bar{q}) - \bar{q}K_2(\bar{q})/4]/2 \pm \exp(-\bar{q})$, $K_{1,2}(\bar{q})$ are the modified Bessel functions of the second kind of the order 1 and 2, respectively.

It follows from (5.3.11) that the backscattering differential cross section ($\varphi = \pi$) does not equal to zero and is given by the expression

$$\frac{1}{L}\frac{d\sigma(\varphi)}{d\varphi}|_{\varphi=\pi} = \bar{k}|\frac{\lambda^2}{4}[K_1(2\bar{k}) - \frac{\bar{k}}{2}K_2(2\bar{k})]^2 - \exp(-4\bar{k})|. \tag{5.3.12}$$

Here we used $\bar{q} = 2\bar{k}\sin\pi/2 = 2\bar{k}$.

Formula (5.3.11) allows one to analyze the differential cross-section as a function of the scattering angle φ and the dimensionless wave vector $\bar{k}$ that connected to the energy of incident electrons E as $\bar{k} = El/\hbar v_F$. The case of slow electrons ($\bar{k} << 1, \bar{k} > \lambda$) can be considered analytically with help of asymptotic expansions (41) of the Appendix D. With account of the leading terms (5.3.11) gives

$$\frac{1}{L}\frac{d\sigma(\varphi)}{d\varphi}|_{\varphi=\pi} = \bar{k}\exp(-4\bar{k}). \tag{5.3.13}$$

It is necessary to note that application of the Born approximation to the electron scattering in graphene by the nonhomogeneous magnetic field of remote nanomagnets requires that the following inequality must be true $\hbar k >> (e/c)A$) that follows from (5.2.1) (the magnetic field of nanomagnet must be a small perturbation). Introducing $\bar{k} = kl$ and the typical value of the vector potential (5.2.14) and (5.2.15) with account of (5.3.2), we get the inequality

$$\bar{k} >> \frac{ed}{\hbar cl} \equiv \lambda. \tag{5.3.14}$$

We may note that for $\lambda << 1$ inequality (5.3.14) becomes $\bar{k}^2 >> \lambda^2$. It can be easily seen from (5.2.3) and (5.2.3) if we use the dimensionless variables.

5.4 Scattering by magnetic dipole parallel to graphene plane

Next, we consider the electron scattering by remote magnetic dipoles parallel to the graphene plane. For the sake of simplicity, we consider two cases when the incident beam of electrons propagates along the magnetic dipole and transversal to it. The

expressions of $V_{1,2}^{\parallel,\perp}$ (5.2.9) with $\mathbf{A}$ and B_z from (5.2.15) where we set $\alpha = 0, \pi/2$, respectively, can be written in the dimensionless form as

$$V_{1,2}^{\parallel} = \frac{\lambda}{\bar{R}^3}\left\{\frac{\lambda(1+y^2)}{\bar{R}^3} \mp 3\frac{x}{\bar{R}^2}\right\}, \tag{5.4.1}$$

$$V_{1,2}^{\perp} = \frac{\lambda}{\bar{R}^3}\left\{\frac{\lambda(1+x^2)}{\bar{R}^3} + 2\bar{k} \mp 3\frac{y}{\bar{R}^2}\right\}. \tag{5.4.2}$$

With the help of these expressions the scattering amplitudes (5.2.11) after passing to the coordinate system with the vector $\mathbf{q}$ parallel to $y'-$ axis like in the previous section, we obtain the following integrals

$$\begin{aligned} f_{1,2}^{\parallel}(\varphi) = -\frac{\lambda}{4}\sqrt{\frac{l}{\pi\bar{k}}}\int_0^{\infty} dr' \int_0^{2\pi} d\phi' \exp(-i\bar{q}r'\cos\phi')\times \\ \left\{\frac{\lambda[r' + r'^3\cos^2(\phi' - \frac{\varphi}{2})]}{R'^6} \mp 3\frac{r'^2\sin(\phi' - \frac{\varphi}{2})}{R'^5}\right\}, \end{aligned} \tag{5.4.3}$$

$$\begin{aligned} f_{1,2}^{\perp}(\varphi) = -\frac{\lambda}{4}\sqrt{\frac{l}{\pi\bar{k}}}\int_0^{\infty} dr' \int_0^{2\pi} d\phi' \exp(-i\bar{q}r'\cos\phi')\times \\ \left\{\frac{\lambda[r' + r'^3\sin^2(\phi' - \frac{\varphi}{2})]}{R'^6} + \frac{2\bar{k}r'}{R'^3} \mp 3\frac{r'^2\cos(\phi' - \varphi/2)}{R'^5}\right\}. \end{aligned} \tag{5.4.4}$$

Integrals over φ' and r' in (5.4.3) and (5.4.4) are given in the Appendix D. The final results read

$$f_{1,2}^{\parallel}(\varphi) = -\frac{\lambda}{2}\sqrt{\frac{\pi l}{\bar{k}}}\left\{I_{\parallel}(\bar{q}) \mp 3iI_{15}^{(2)}(\bar{q})\sin\varphi/2\right\} \tag{5.4.5}$$

and

$$f_{1,2}^{\perp}(\varphi) = -\frac{\lambda}{2}\sqrt{\frac{\pi l}{\bar{k}}}\left\{I_{\perp}(\bar{q}) \pm 3iI_{15}^{(2)}(\bar{q})\cos\varphi/2\right\}. \tag{5.4.6}$$

Here $I_{\parallel}(\bar{q}) = \lambda[I_{06}^{(1)}(\bar{q}) - \frac{1}{\bar{q}}I_{16}^{(2)}\cos\varphi + I_{06}^{3}(\bar{q})\cos^2\varphi/2]$ and $I_{\perp}(\bar{q}) = \lambda[I_{06}^{(1)}(\bar{q}) + \frac{1}{\bar{q}}I_{16}^{(2)}(\bar{q})\cos(\varphi) + I_{06}^{(3)}\sin^2\varphi/2] + 2\bar{k}I_{03}^{(1)}(\bar{q})$.

The differential scattering cross sections by remote magnetic dipoles parallel and perpendicular to the incident beams of electrons in graphene according to (5.2.12)

and (5.4.5) and (5.4.6) with usage of (40) from the Appendix D are given by

$$\frac{1}{L}\frac{d\sigma_{\parallel}(\varphi)}{d\varphi} = \bar{k}\left\{\frac{\lambda^2}{64}[\bar{q}K_2(\bar{q})\sin^2\frac{\varphi}{2} + K_1(\bar{q})(2+\cos\varphi)]^2 + \exp(-2\bar{q})\sin^2\frac{\varphi}{2}\right\}\sin^2\frac{\varphi}{2},$$
$$\frac{1}{L}\frac{d\sigma_{\perp}(\varphi)}{d\varphi} = \bar{k}\left\{\left(\frac{\lambda}{8}\sin\frac{\varphi}{2}\left[\bar{q}K_2(\bar{q})\cos^2\frac{\varphi}{2} + K_1(\bar{q})(2-\cos\varphi)\right] + \exp(-\bar{q})\right)^2 + \frac{1}{4}\exp(-2\bar{q})\sin^2\varphi\right\}. \tag{5.4.7}$$

These formulas show that the backscattering cross section ($\varphi = \pi, \bar{q} = 2\bar{k}$) are nonzero in both cases

$$\begin{aligned}\frac{1}{L}\frac{d\sigma_{\parallel}(\varphi)}{d\varphi} &= \bar{k}\left\{\frac{\lambda^2}{64}[2\bar{k}K_2(2\bar{k}) + K_1(2\bar{k})]^2 + \exp(-4\bar{k})\right\},\\ \frac{1}{L}\frac{d\sigma_{\perp}(\varphi)}{d\varphi} &= \bar{k}\left(\frac{3\lambda}{8}K_1(2\bar{k}) + \exp(-2\bar{k})\right)^2.\end{aligned} \tag{5.4.8}$$

For $\bar{k} > 1$, the cross sections (5.4.7) are practically equal but they are small due the asymptotic behavior (see Appendix D).

Figure 5.4 depicts the graphs of $d\sigma(\varphi)/d\varphi$ versus the scattering angle φ in units L for particular value of $\bar{k}$ built according to (5.3.11) (curve 1, blue online) and (5.4.7) (dipole parallel to incident electron beam curve 2, brown online and dipole transverse to incident electron beam curve 3, khaki color online). Here we consider $\lambda = 0.1; \bar{k} = 0.8$. Comparing curve 1 with the result obtained in Chapter 4, the differential scattering cross-section enhanced 20 times. Curve 2 is drawn for the case when the magnetic dipole of the nanomagnet is parallel to both the graphene plane and the incident beam of electrons. As one can see from the graph the differential cross-section is much smaller than those shown by curve 1 and 3. This indicates that if one is interested to obtain large scattering lengths, he/she has to arrange the electrons beam transverse to the direction of the dipole of the nanomagnet. One more feature of the graphs is that the similarity between curve 1 and 3.

One common feature of the differential cross-section graphs is that for $\bar{k} << 1$ the

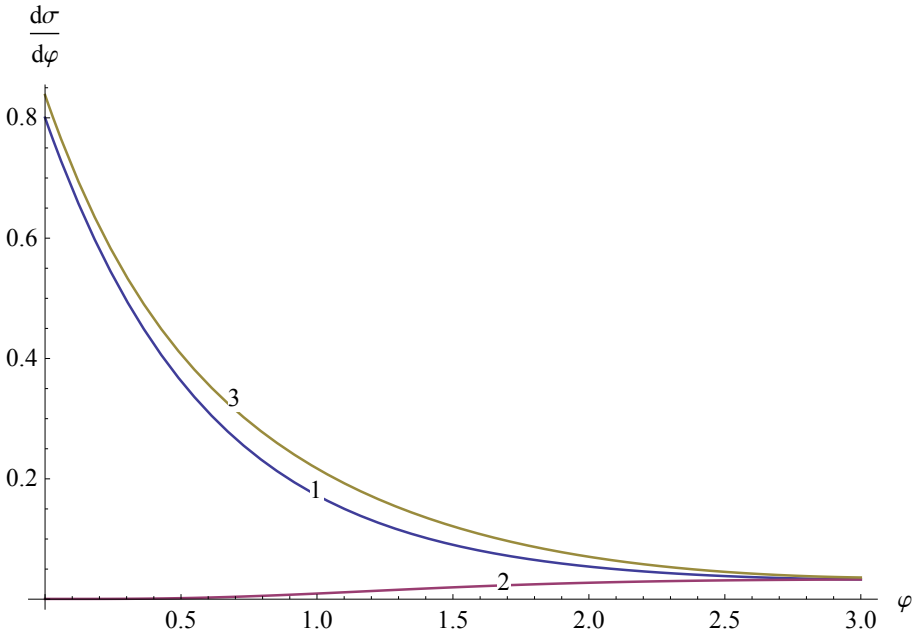

Figure 5.4: The differential cross-section $d\sigma/d\varphi$ in units of L versus scattering angle φ for $\lambda = 0.1$ and $\bar{k} = 0.8$. Curve 1 (blue) for magnetic dipole moment of the nanomagnet perpendicular to the graphene plane, curve 2 (brown) for magnetic dipole moment of the nanomagnet parallel to the incident electron beam in the graphene plane, curve 3 (khaki) magnetic dipole moment of the nanomagnet parallel to the graphene plane and perpendicular to the incident electron beam in the graphene plane Eqs.(5.3.11), (5.4.7).

graphs show isotropic property and for $\bar{k} >> 1$ goes to zero. Our graphs pattern and the numerical results are similar to the the results obtained in [125].

5.5 Transport electron cross sections

The transport cross section or transport scattering length, the quantity which controls the transport phenomena, is given by the relation

$$\sigma_{tr} = \int_0^{2\pi} (1 - \cos\varphi) \frac{d\sigma}{d\varphi} d\varphi. \tag{5.5.1}$$

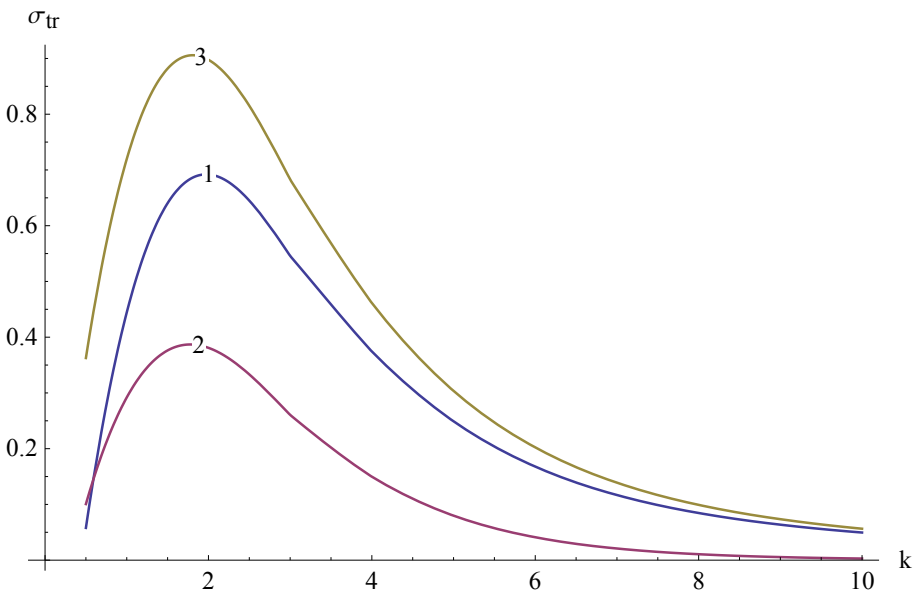

Figure 5.5: The transport cross-section σ divided by L versus the dimensionless energy $\bar{k}$ for $\lambda = 0.1$. Curve 1 the magnetic dipole is transverse to the graphene plane. Curve 2,the magnetic dipole is parallel to the graphene plane and parallel to the incident beam of electrons. Curve 3, the magnetic dipole is parallel to the graphene plane and perpendicular to the incident beam of electrons. Here we consider few leading terms of (5.3.11) and (5.4.7), and extrapolation method were applied.

Graphs in Figures 3 illustrate the electron transport cross-section built in according to (5.5.1). The graphs show that the electron transport cross-section, which directly related to the the resistivity of the material is large when the electron beams in the graphene plane are perpendicular to the suspended dipole of the nanomagnet, curve 1 and 3. One common feature of these curves is that they have maxima around $\bar{k} = 1.8$ with little variation. Other numerical results show that the peak of these maxima shifted to left for small value of λ.

Comparing the present result with Chapter 4, it is possible to enhance the scattering length and the transport cross-section 10 to 100 times depending on the value of λ,

but we have to be alert about the inequality given by (5.3.14). Our graphs pattern results are similar to the the results obtained in [126].

5.6 Conclusions

In this Chapter, we studied elastic electron scattering by remote nanomagnets transverse and parallel to the graphene plane. We analyze the scattering of massless Dirac fermions by a fixed magnetic dipole moment located at a height l above the origin of the 2D-graphene plane. With the help of specially developed Born approximation, we derived the differential cross-section and the transport cross-section. The differential scattering cross-section and the transport cross-section are dominant when the magnetic dipole of the remote nanomagnet is transverse to the electron beam in the graphene plane. Our results show that one has to consider higher terms in the expansion of potential given by (5.2.9), which has significant contribution to the scattering parameters, when the coupling parameter λ is in the order of 0.1 to 1. And we found that the backscattering cross-section of electrons are non-zero for all orientations.

Appendix A

A.1 Eigenvalue and Eigenfunction of Massless Dirac Equation

A Dirac equation describing massless spin-half particles moving in the plane $\mathbf{r} = (x, y)$ of graphene is given by

$$v_F \vec{\sigma} \cdot \vec{p} \begin{pmatrix} \psi_1 \\ \psi_2 \end{pmatrix} = E \begin{pmatrix} \psi_1 \\ \psi_2 \end{pmatrix}, \tag{A.1.1}$$

where the pauli matrices $\vec{\sigma} = (\sigma_x, \sigma_y)$,

$$\sigma_x = \begin{pmatrix} 0 & 1 \\ 1 & 0 \end{pmatrix}, \sigma_y = \begin{pmatrix} 0 & -i \\ i & 0 \end{pmatrix}, \tag{A.1.2}$$

p is momentum of the particle, v_F is the speed of Dirac neutrino and (ψ_1, ψ_2) are two component column spinor wavefunctions. Substituting the components of the pauli matrix

$$v_F[\sigma_x p_x + \sigma_y p_y] \begin{pmatrix} \psi_1 \\ \psi_2 \end{pmatrix} = E \begin{pmatrix} \psi_1 \\ \psi_2 \end{pmatrix}. \tag{A.1.3}$$

We can rewrite the above equation in matrix form

$$v_F \begin{pmatrix} 0 & p_x - ip_y \\ p_x + ip_y & 0 \end{pmatrix} \begin{pmatrix} \psi_1 \\ \psi_2 \end{pmatrix} = E \begin{pmatrix} \psi_1 \\ \psi_2 \end{pmatrix}. \tag{A.1.4}$$

And the wavefunctions can be written in the form of plane wave

$$\begin{pmatrix} \psi_1 \\ \psi_2 \end{pmatrix} = \begin{pmatrix} U_1 \\ U_2 \end{pmatrix} e^{i\mathbf{k}.\mathbf{r}}. \tag{A.1.5}$$

After the action of the Operators p_x and p_y on the wavefunctions, (A.1.5) can be simplified as

$$v_F\hbar \begin{pmatrix} 0 & k_x - ik_y \\ k_x + ik_y & 0 \end{pmatrix} \begin{pmatrix} U_1 \\ U_2 \end{pmatrix} = E \begin{pmatrix} U_1 \\ U_2 \end{pmatrix}. \tag{A.1.6}$$

To find the eigenvalue and eigenfunctions lets rearrange the equation as follows

$$\begin{pmatrix} -\frac{E}{v_F\hbar} & k_x - ik_y \\ k_x + ik_y & -\frac{E}{v_F\hbar} \end{pmatrix} \begin{pmatrix} U_1 \\ U_2 \end{pmatrix} = 0. \tag{A.1.7}$$

Eqaution(A.1.7) to have non zero value, the determinate of the 2x2 matrix must be set to zero, i.e

$$\begin{vmatrix} -\frac{E}{v_F\hbar} & k_x - ik_y \\ k_x + ik_y & -\frac{E}{v_F\hbar} \end{vmatrix} = 0, \tag{A.1.8}$$

from which we get the eigenvalue

$$E = \pm v_F\hbar k. \tag{A.1.9}$$

The $\pm$ sign refers to the two sublattice 1 and 2. To get the eigenfunction lets substitute the eigenvalue, $E = v_F\hbar k$ (positive) in to (A.1.7)

$$\begin{pmatrix} -k & k_x - ik_y \\ k_x + ik_y & -k \end{pmatrix} \begin{pmatrix} U_1 \\ U_2 \end{pmatrix} = 0, \tag{A.1.10}$$

from this matrix equation we can get two simultaneous equations

$$\begin{aligned} kU_1 &= (k_x - ik_y)U_2, \\ kU_2 &= (k_x + ik_y)U_1, \end{aligned} \tag{A.1.11}$$

or

$$\begin{aligned} U_1 &= \frac{(k_x - ik_y)}{k} U_2, \\ U_2 &= \frac{(k_x + ik_y)}{k} U_1. \end{aligned} \tag{A.1.12}$$

The component of the two column spinor wavefunctions are

$$\begin{pmatrix} U_1 \\ U_2 \end{pmatrix} = U_2 \begin{pmatrix} \frac{(k_x - ik_y)}{k} \\ 1 \end{pmatrix}, \tag{A.1.13}$$

or

$$\begin{pmatrix} U_1 \\ U_2 \end{pmatrix} = U_1 \begin{pmatrix} 1 \\ \frac{(k_x + ik_y)}{k} \end{pmatrix}, \tag{A.1.14}$$

insert the wavevectors $k_x = k\cos\theta, k_y = k\sin\theta$, then

$$\begin{pmatrix} U_1 \\ U_2 \end{pmatrix} = U_2 \begin{pmatrix} e^{-i\theta} \\ 1 \end{pmatrix}, \tag{A.1.15}$$

or

$$\begin{pmatrix} U_1 \\ U_2 \end{pmatrix} = U_1 \begin{pmatrix} 1 \\ e^{i\theta} \end{pmatrix}. \tag{A.1.16}$$

To get the normalized wavefunctions (U_n), we divide the wavefunction by its length ($|U|$), i.e

$$U_n = \frac{U}{|U|}. \tag{A.1.17}$$

The length

$$|U| = U_2\sqrt{e^{-2i\theta} + 1} = U_2\sqrt{2}\sqrt{cos\theta}e^{-i\theta/2}, \tag{A.1.18}$$

or

$$|U| = U_1\sqrt{e^{2i\theta} + 1} = U_1\sqrt{2}\sqrt{cos\theta}e^{i\theta/2}, \tag{A.1.19}$$

using mathematical relation

$$\begin{aligned} e^{2i\theta} + 1 &= 2cos\theta e^{i\theta}, \\ e^{-2i\theta} + 1 &= 2cos\theta e^{-i\theta}, \end{aligned} \tag{A.1.20}$$

we obtain the eigenfunction

$$\begin{pmatrix} U_1 \\ U_2 \end{pmatrix} = \frac{1}{\sqrt{2}} \begin{pmatrix} e^{-i\theta/2} \\ e^{i\theta/2} \end{pmatrix}. \tag{A.1.21}$$

Finally interims of the plane wave

$$\begin{pmatrix} \psi_1 \\ \psi_2 \end{pmatrix} = \frac{1}{\sqrt{2}} \begin{pmatrix} e^{-i\theta/2} \\ e^{i\theta/2} \end{pmatrix} e^{i\mathbf{k.r}}. \tag{A.1.22}$$

Again to get the eigenfunction if we substitute the eigenvalue, $E = -v_F\hbar k$ (negative) in to (7). Following the same steps we get

$$\begin{pmatrix} \psi_1 \\ \psi_2 \end{pmatrix} = \frac{1}{\sqrt{2}} \begin{pmatrix} e^{-i\theta/2} \\ -e^{i\theta/2} \end{pmatrix} e^{i\mathbf{k.r}}. \tag{A.1.23}$$

Appendix B

B.1 Massless Dirac Equation in Spherical Coordinate

In this part we will solve Dirac equation for massless spin-half particles

$$i\vec{\sigma}\cdot\vec{\nabla}\begin{pmatrix}\psi_1\\ \psi_2\end{pmatrix}=k\begin{pmatrix}\psi_1\\ \psi_2\end{pmatrix}. \tag{B.1.1}$$

Let us write the (B.1.1) in spherical polar coordinate

$$i\begin{pmatrix}0 & e^{-i\varphi}\left(\frac{\partial}{\partial r}-\frac{i}{r}\frac{\partial}{\partial\varphi}\right)\\ e^{i\varphi}\left(\frac{\partial}{\partial r}+\frac{i}{r}\frac{\partial}{\partial\varphi}\right) & 0\end{pmatrix}\begin{pmatrix}\psi_1\\ \psi_2\end{pmatrix}=k\begin{pmatrix}\psi_1\\ \psi_2\end{pmatrix}, \tag{B.1.2}$$

the wave functions can be written as plane wave

$$\begin{aligned}\psi_1(r,\varphi)&=\psi_1(r)e^{il\varphi},\\ \psi_2(r,\varphi)&=\psi_2(r)e^{i(l+1)\varphi},\end{aligned} \tag{B.1.3}$$

where l is integer, on substituting the (B.1.3) in to the (B.1.2) and solve the matrix, we get

$$\begin{aligned}e^{-i\varphi}\left(\frac{\partial}{\partial r}-\frac{i}{r}\frac{\partial}{\partial\varphi}\right)\psi_2(r)e^{i(l+1)\varphi}&=ik\psi_1(r)e^{il\varphi},\\ e^{i\varphi}\left(\frac{\partial}{\partial r}+\frac{i}{r}\frac{\partial}{\partial\varphi}\right)\psi_1(r)e^{il\varphi}&=ik\psi_2(r)e^{i(l+1)\varphi}.\end{aligned} \tag{B.1.4}$$

Simplifying (B.1.4) will result

$$\begin{aligned}\left(\frac{\partial}{\partial r}+\frac{l+1}{r}\right)\psi_2(r)&=ik\psi_1(r),\\ \left(\frac{\partial}{\partial r}-\frac{l}{r}\right)\psi_1(r)&=ik\psi_2(r),\end{aligned}\tag{B.1.5}$$

or in this form

$$\begin{aligned}\psi_1(r)&=\frac{1}{ik}\left(\frac{\partial}{\partial r}+\frac{l+1}{r}\right)\psi_2(r),\\ \psi_2(r)&=\frac{1}{ik}\left(\frac{\partial}{\partial r}-\frac{l}{r}\right)\psi_1(r).\end{aligned}\tag{B.1.6}$$

Substitute one in to the other in (B.1.6)

$$\begin{aligned}\left(\frac{\partial}{\partial r}+\frac{l+1}{r}\right)\left(\frac{\partial}{\partial r}-\frac{l}{r}\right)\psi_1(r)&=-k^2\psi_1(r),\\ \left(\frac{\partial}{\partial r}-\frac{l}{r}\right)\left(\frac{\partial}{\partial r}+\frac{l+1}{r}\right)\psi_2(r)&=-k^2\psi_2(r).\end{aligned}\tag{B.1.7}$$

Multiplying the operators in (B.1.7)

$$\begin{aligned}\left[\frac{\partial^2}{\partial r^2}+\frac{l+1}{r}\frac{\partial}{\partial r}-\frac{\partial}{\partial r}\left(\frac{l}{r}\right)-\frac{l(l+1)}{r^2}\right]\psi_1(r)&=-k^2\psi_1(r),\\ \left[\frac{\partial^2}{\partial r^2}-\frac{l}{r}\frac{\partial}{\partial r}+\frac{\partial}{\partial r}\left(\frac{l+1}{r}\right)-\frac{l(l+1)}{r^2}\right]\psi_2(r)&=-k^2\psi_2(r).\end{aligned}\tag{B.1.8}$$

Further simplifying we obtain

$$\begin{aligned}\left[\frac{\partial^2}{\partial r^2}+\frac{1}{r}\frac{\partial}{\partial r}-\frac{l^2}{r^2}\right]\psi_1(r)&=-k^2\psi_1(r),\\ \left[\frac{\partial^2}{\partial r^2}+\frac{1}{r}\frac{\partial}{\partial r}-\frac{(l+1)^2}{r^2}\right]\psi_2(r)&=-k^2\psi_2(r),\end{aligned}\tag{B.1.9}$$

we get Bessel equation of the form

$$\begin{aligned}\left[\frac{d^2}{dr^2}+\frac{1}{r}\frac{d}{dr}+k^2-\frac{l^2}{r^2}\right]\psi_1(r)&=0,\\ \left[\frac{d^2}{dr^2}+\frac{1}{r}\frac{d}{dr}+k^2-\frac{(l+1)^2}{r^2}\right]\psi_2(r)&=0.\end{aligned}\tag{B.1.10}$$

Now, let $x = kr$, the (B.1.10) interims of x can be written as

$$\begin{aligned} \left[\frac{d^2}{dx^2} + \frac{1}{x}\frac{d}{dx} + 1 - \frac{n^2}{x^2}\right]\psi_1(x) = 0, \\ \left[\frac{d^2}{dx^2} + \frac{1}{x}\frac{d}{dx} + 1 - \frac{m^2}{x^2}\right]\psi_2(x) = 0, \end{aligned} \tag{B.1.11}$$

where $n^2 = k^2 l^2$, $m^2 = k^2(l+1)^2$. The general solutions of Bessel equation of order n and order m are given by

$$\begin{aligned} \psi_1(x) = c_1 J_n(x) + c_2 Y_n(x), \\ \psi_2(x) = c_1 J_m(x) + c_2 Y_m(x), \end{aligned} \tag{B.1.12}$$

where J_n is Bessel functions of the first kind order n, Y_n is Bessel function of the second kind of order n.

Appendix C

C.1 Massless Dirac Equation In External Magnetic Field

The Dirac equation for massless electron in graphene inside an external magnetic field written as

$$[v_F\vec{\sigma}\cdot(\vec{p}-\frac{e\vec{A}}{c})]\begin{pmatrix}\psi_1\\ \psi_2\end{pmatrix}=E\begin{pmatrix}\psi_1\\ \psi_2\end{pmatrix}, \tag{C.1.1}$$

the pauli matrices $\vec{\sigma}=(\sigma_x,\sigma_y)$

$$\sigma_x=\begin{pmatrix}0&1\\1&0\end{pmatrix}, \qquad \sigma_y=\begin{pmatrix}0&-i\\i&0\end{pmatrix}. \tag{C.1.2}$$

Substitute the x-comp and y-comp Pauli matrices in to the massless Dirac equation

$$v_F[\sigma_x(p_x-\frac{eA_x}{c})+\sigma_y(p_y-\frac{eA_y}{c})]\begin{pmatrix}\psi_1\\ \psi_2\end{pmatrix}=E\begin{pmatrix}\psi_1\\ \psi_2\end{pmatrix}, \tag{C.1.3}$$

Again substitute the value of pauli matrices

$$v_F\begin{pmatrix}0&(p_x-\frac{eA_x}{c})-i(p_y-\frac{eA_y}{c})\\(p_x-\frac{eA_x}{c})+i(p_y-\frac{eA_y}{c})&0\end{pmatrix}\begin{pmatrix}\psi_1\\ \psi_2\end{pmatrix}=E\begin{pmatrix}\psi_1\\ \psi_2\end{pmatrix}, \tag{C.1.4}$$

let the value π_+, π_-

$$\begin{aligned}\pi_+ &= (p_x - \frac{eA_x}{c}) + i(p_y - \frac{eA_y}{c}),\\ \pi_- &= (p_x - \frac{eA_x}{c}) - i(p_y - \frac{eA_y}{c}).\end{aligned} \tag{C.1.5}$$

The massless Dirac equation can be

$$v_F \begin{pmatrix} 0 & \pi_- \\ \pi_+ & 0 \end{pmatrix} \begin{pmatrix} \psi_1 \\ \psi_2 \end{pmatrix} = E \begin{pmatrix} \psi_1 \\ \psi_2 \end{pmatrix}. \tag{C.1.6}$$

Expand the (C.1.6)

$$\begin{aligned} v_F \pi_+ \psi_1 &= E\psi_2,\\ v_F \pi_- \psi_2 &= E\psi_1. \end{aligned} \tag{C.1.7}$$

The wave functions can be written

$$\begin{aligned}\psi_1 &= \frac{v_F}{E}\pi_-\psi_2,\\ \psi_2 &= \frac{v_F}{E}\pi_+\psi_1.\end{aligned} \tag{C.1.8}$$

Substitute one in to the other in (C.1.8)

$$\begin{aligned}\pi_-\pi_+\psi_1 &= \left(\frac{E}{v_F}\right)^2 \psi_1,\\ \pi_+\pi_-\psi_2 &= \left(\frac{E}{v_F}\right)^2 \psi_2.\end{aligned} \tag{C.1.9}$$

Product of Operators

Let us calculate the product of the two operators $\pi_-\pi_+$

$$\begin{aligned}\pi_-\pi_+ &= \left[(p_x - \frac{eA_x}{c}) - i(p_y - \frac{eA_y}{c})\right]\left[(p_x - \frac{eA_x}{c}) + i(p_y - \frac{eA_y}{c})\right],\\ &= (p_x - \frac{eA_x}{c})^2 + (p_y - \frac{eA_y}{c})^2 + i\left[(p_x - \frac{eA_x}{c})(p_y - \frac{eA_y}{c}) - (p_y - \frac{eA_y}{c})(p_x - \frac{eA_x}{c})\right],\\ &= (p - \frac{eA}{c})^2 - i\left[[p_y, p_x] + \frac{e}{c}[p_xA_y - p_yA_x] + \frac{e^2}{c^2}[A_y, A_x]]\right],\end{aligned} \tag{C.1.10}$$

since $[p_y, p_x] = 0$, $[A_y, A_x] = 0$,

$$\pi_-\pi_+ = (p - \frac{eA}{c})^2 - i\frac{e}{c}\Big[p_xA_y - p_yA_x\Big]. \tag{C.1.11}$$

Expanding the expression $(p - \frac{eA}{c})^2$,

$$\pi_-\pi_+ = \Big[p^2 - \frac{e}{c}(\frac{\hbar}{i}\nabla \cdot A + 2A \cdot p) + \frac{e^2}{c^2}A^2 - i\frac{e}{c}\Big[p_xA_y - p_yA_x\Big]\Big], \tag{C.1.12}$$

using Gauge invariance $\nabla \cdot A = 0$,

$$\pi_-\pi_+ = \Big[p^2 - 2\frac{e}{c}(A \cdot p) + \frac{e^2}{c^2}A^2 - i\frac{e}{c}\Big[p_xA_y - p_yA_x\Big]\Big]. \tag{C.1.13}$$

Again we have

$$p_xA_y - p_yA_x = \frac{\hbar}{i}\Big[\frac{\partial}{\partial x}A_y - \frac{\partial}{\partial y}A_x\Big] = \frac{\hbar}{i}B_z, \tag{C.1.14}$$

then

$$\pi_-\pi_+ = \Big[p^2 - 2\frac{e}{c}(A \cdot p) + \frac{e^2}{c^2}A^2 - \frac{e}{c}\hbar B_z\Big], \tag{C.1.15}$$

or

$$\pi_-\pi_+ = \Big[p^2 + \frac{e^2}{c^2}A^2 - \frac{e}{c}\Big[2(A \cdot p) + \hbar B_z\Big]\Big]. \tag{C.1.16}$$

And the inverse $\pi_+\pi_-$

$$\begin{aligned}\pi_+\pi_- &= \Big[(p_x - \frac{eA_x}{c}) + i(p_y - \frac{eA_y}{c})\Big]\Big[(p_x - \frac{eA_x}{c}) - i(p_y - \frac{eA_y}{c})\Big],\\ = (p_x - \frac{eA_x}{c})^2 + (p_y - \frac{eA_y}{c})^2 &+ i\Big[(p_y - \frac{eA_y}{c})(p_x - \frac{eA_x}{c}) - (p_x - \frac{eA_x}{c})(p_y - \frac{eA_y}{c})\Big],\\ &= (p - \frac{eA}{c})^2 + i\Big[[p_y, p_x] + \frac{e}{c}\Big[p_xA_y - p_yA_x\Big] + \frac{e^2}{c^2}[A_y, A_x]]\Big],\end{aligned} \tag{C.1.17}$$

again $[p_y, p_x] = 0$, $[A_y, A_x] = 0$,

$$\pi_+\pi_- = (p - \frac{eA}{c})^2 + i\frac{e}{c}\Big[p_xA_y - p_yA_x\Big]. \tag{C.1.18}$$

Expanding the expression $(p - \frac{eA}{c})^2$,

$$\pi_+\pi_- = \Big[p^2 - \frac{e}{c}(\frac{\hbar}{i}\nabla \cdot A + 2A \cdot p) + \frac{e^2}{c^2}A^2 + i\frac{e}{c}\Big[p_xA_y - p_yA_x\Big]\Big], \tag{C.1.19}$$

using Gauge invariance $\nabla \cdot A = 0$,

$$\pi_+\pi_- = \Big[p^2 - 2\frac{e}{c}(A \cdot p) + \frac{e^2}{c^2}A^2 + \frac{e}{c}\hbar B_z\Big], \tag{C.1.20}$$

or

$$\pi_+\pi_- = \Big[p^2 + \frac{e^2}{c^2}A^2 - \frac{e}{c}\Big[2(A \cdot p) - \hbar B_z\Big]\Big]. \tag{C.1.21}$$

Helmonz like equations

In this part Helmonz like equations derived from massless Dirac electrons in the presence of external magnetic field. we substitute the value of the product of the two operators (C.1.16),(C.1.21) in to (C.1.9), we get

$$\begin{aligned}\Big[p^2 + \frac{e^2}{c^2}A^2 - \frac{e}{c}\Big[2(A \cdot p) + \hbar B_z\Big]\Big]\psi_1 &= \left(\frac{E}{v_F}\right)^2\psi_1,\\ \Big[p^2 + \frac{e^2}{c^2}A^2 - \frac{e}{c}\Big[2(A \cdot p) - \hbar B_z\Big]\Big]\psi_2 &= \left(\frac{E}{v_F}\right)^2\psi_2,\end{aligned} \tag{C.1.22}$$

since $p = -i\hbar\nabla$, and $E/v_F = \hbar k$,

$$\begin{aligned}\Big[-\hbar^2\nabla^2 + \frac{e^2}{c^2}A^2 - \frac{e}{c}\Big[2(A \cdot p) + \hbar B_z\Big]\Big]\psi_1 &= \hbar^2k^2\psi_1,\\ \Big[-\hbar^2\nabla^2 + \frac{e^2}{c^2}A^2 - \frac{e}{c}\Big[2(A \cdot p) - \hbar B_z\Big]\Big]\psi_2 &= \hbar^2k^2\psi_2.\end{aligned} \tag{C.1.23}$$

Rearranging the (C.1.23) we will obtain the following

$$\begin{aligned}[\nabla^2 + k^2]\psi_1 &= \frac{1}{\hbar^2}\left[\frac{e^2}{c^2}A^2 - \frac{e}{c}\left[2(A\cdot p) + \hbar B_z\right]\right]\psi_1, \\ [\nabla^2 + k^2]\psi_2 &= \frac{1}{\hbar^2}\left[\frac{e^2}{c^2}A^2 - \frac{e}{c}\left[2(A\cdot p) - \hbar B_z\right]\right]\psi_2,\end{aligned} \tag{C.1.24}$$

or combined form of the above equations can be rewritten as

$$[\nabla^2 + k^2]\psi_{1,2} = \frac{1}{\hbar^2}\left[\frac{e^2}{c^2}A^2 - \frac{e}{c}\left[2(A\cdot p) \pm \hbar B_z\right]\right]\psi_{1,2}. \tag{C.1.25}$$

The Helmonz type equation is

$$[\nabla^2 + k^2]\psi_{1,2} = \hat{V}_{1,2}\psi_{1,2}, \tag{C.1.26}$$

where

$$\hat{V}_{1,2} = \frac{1}{\hbar^2}\left[\frac{e^2}{c^2}A^2 - \frac{e}{c}[2(A\cdot p) \pm \hbar B_z]\right]. \tag{C.1.27}$$

At large distance from the scattering center the wave function can be written as

$$\psi_{1,2} = \psi^0_{1,2} + \psi^1_{1,2}, \quad \psi^1_{1,2} << \psi^0_{1,2}. \tag{C.1.28}$$

The wavefunction is described as the incident wave, we chose them in the form of plane wave propagating along x-axis

$$\psi^0_{1,2} = \frac{1}{\sqrt{2}}\begin{pmatrix} 1 \\ 1 \end{pmatrix} exp(ikx). \tag{C.1.29}$$

The factor $\frac{1}{\sqrt{2}}$ is the unit normalization of the incident wave. After the operation of of the momentum operator on the wave function the Helmonz type equation can be rewritten as

$$[\nabla^2 + k^2]\psi_{1,2} = V_{1,2}\psi^0_{1,2}, \tag{C.1.30}$$

where now the potential can be written as

$$V_{1,2} = \frac{1}{\hbar^2}\left[\frac{e^2}{c^2}A^2 - \frac{e\hbar}{c}[2A_x k \pm B_z]\right]. \tag{C.1.31}$$

Appendix D

D.1 Scattering Amplitude And Differential Cross Sections

Magnetic dipole Oriented Perpendicular to the Graphene

By considering different positions of dipole with respect to the graphene plane, we will solve the Helmonz equation (C.1.30). Now in this part when the magnetic dipole is perpendicular to the graphene plane.

Potential

The potential of the Helmonz equation (C.1.31) is

$$V_{1,2} = \frac{1}{\hbar^2}\left[\frac{e^2}{c^2}A^2 - \frac{e\hbar}{c}[2A_x k \pm B_z]\right], \tag{D.1.1}$$

where components of dimensionless vector potential for perpendicular orientation of the dipole can be given

$$A_x = -\frac{d}{l^2}\frac{y}{\bar{R}^3}, \quad A_y = \frac{d}{l^2}\frac{x}{\bar{R}^3}, \quad A_z = 0, \quad A^2 = \frac{d^2}{l^4}\frac{r^2}{\bar{R}^6}, \tag{D.1.2}$$

and z-component magnetic field of the dipole a distance R from the graphene plane

$$B_z = \frac{d}{l^3}\frac{(2-r^2)}{\bar{R}^5}. \tag{D.1.3}$$

Substitute the value of A^2, A_x, and B_z into (D.1.1)

$$V_{1,2} = \left[\frac{e^2d^2}{c^2\hbar^2l^4}\frac{r^2}{\bar{R}^6} + \frac{ed}{c\hbar l}\left[\frac{2}{l^2}\frac{y}{\bar{R}^3}kl \mp \frac{1}{l^2}\frac{(2-r^2)}{\bar{R}^5}\right]\right], \tag{D.1.4}$$

using the coupling constants $\lambda = \frac{ed}{c\hbar l}$ and $\bar{k} = kl$

$$V_{1,2} = \frac{1}{l^2}\left[\lambda^2\frac{r^2}{\bar{R}^6} + \lambda\left[2\frac{y}{\bar{R}^3}\bar{k} \mp \frac{(2-r^2)}{\bar{R}^5}\right]\right]. \tag{D.1.5}$$

The dimensionless potential

$$V_{1,2} = \frac{\lambda}{\bar{R}^3}\left[\lambda\frac{r^2}{\bar{R}^3} + \left[2\bar{k}y \mp \frac{2-r^2}{\bar{R}^2}\right]\right]. \tag{D.1.6}$$

Scattering Amplitude

Scattering amplitude in the dimensionless potential is given by

$$f_{1,2}(\varphi) = -\frac{1}{4}\sqrt{\frac{1}{\pi k}}\int \exp(-i\mathbf{q}.\mathbf{r}')V_{1,2}(r')d^2r', \tag{D.1.7}$$

and explicit form of scattering amplitude, $d^2r' = r'dr'd\phi'$

$$f_{1,2}(\varphi) = -\frac{1}{4}\sqrt{\frac{1}{\pi k}}\int_0^\infty r'dr'\int_0^{2\pi} d\phi' \exp(-iqr'\cos\phi')V_{1,2}. \tag{D.1.8}$$

Substitute the potential $V_{1,2}$ is given by (D.1.6) into (D.1.8), we get

$$f_{1,2}(\varphi) = -\frac{\lambda}{4}\sqrt{\frac{l}{\pi\bar{k}}}\int_0^\infty r'dr'\int_0^{2\pi} d\phi' \exp(-i\bar{q}r'\cos\phi')\left[\lambda\frac{r'^2}{\bar{R}^6} + \left[\frac{2\bar{k}y'}{\bar{R}^3} \mp \frac{2-r'^2}{\bar{R}^5}\right]\right]. \tag{D.1.9}$$

One can expand the equations like this $y' = r'\cos(\phi' - \varphi/2)$ (see Fig 4.1)

$$f_{1,2}(\varphi) = -\frac{\lambda}{4}\sqrt{\frac{l}{\pi\bar{k}}}\int_0^\infty dr'\int_0^{2\pi} d\phi' \exp(-i\bar{q}r'\cos\phi')\left[\lambda\frac{r'^3}{\bar{R}^6} + \left[2\bar{k}r'^2\cos(\phi'-\varphi/2) \mp \frac{2r'-r'^3}{\bar{R}^5}\right]\right], \tag{D.1.10}$$

or

$$f_{1,2}(\varphi) = -\frac{\lambda}{4}\sqrt{\frac{l}{\pi\bar{k}}}\Big[\lambda\int_0^\infty dr'\frac{r'^3}{R'^6}\int_0^{2\pi} d\phi'\exp(-i\bar{q}r'\cos\phi')+ \\ 2\bar{k}\int_0^\infty dr'\frac{r'^2}{R'^3}\int_0^{2\pi} d\phi'\exp(-i\bar{q}r'\cos\phi')\cos(\phi'-\varphi/2) \\ \mp\int_0^\infty dr'\frac{2r'-r'^3}{R'^5}\int_0^{2\pi} d\phi'\exp(-i\bar{q}r'\cos\phi')\Big]. \tag{D.1.11}$$

Now by considering the following integrals

$$\int_0^{2\pi} d\phi'\exp(-i\bar{q}r'\cos\phi') = 2\pi J_0(qr), \\ \int_0^{2\pi} d\phi' e^{(-i\bar{q}r'\cos\phi')}\cos(\phi'-\varphi/2) = -2\pi i J_1(qr)\cos(\varphi/2). \tag{D.1.12}$$

We can write (D.1.11) as follows

$$f_{1,2}(\varphi) = -\frac{\lambda}{2}\sqrt{\frac{\pi l}{\bar{k}}}\left\{\int_0^\infty dr'\frac{\lambda r'^3}{R'^6}J_0(qr') - 2i\int_0^\infty dr'\frac{\bar{k}r'^2}{R'^3}J_1(qr')\cos(\varphi/2) \mp \int_0^\infty dr'\frac{2r'-r'^3}{R'^5}J_0(qr')\right\} \tag{D.1.13}$$

From (D.1.13), we get the following integrals

$$I_{nm}^{(p)}(q) = \int_0^\infty J_n(qr)\frac{r^p dr}{(1+r^2)^{m/2}}, \tag{D.1.14}$$

and the scattering amplitude in terms of the integrals (D.1.14)

$$f_{1,2}(\varphi) = -\frac{\lambda}{2}\sqrt{\frac{\pi l}{\bar{k}}}\left\{\lambda I_{06}^3 - 2\bar{k}iI_{13}^2\cos(\varphi/2) \mp [2I_{05}^1 - I_{05}^3]\right\}. \tag{D.1.15}$$

If we let

$$I_\pm = \lambda I_{06}^3 \mp [2I_{05}^1 - I_{05}^3], \tag{D.1.16}$$

The more precise form of the scattering amplitude will be

$$f_{1,2}(\varphi) = -\frac{\lambda}{2}\sqrt{\frac{\pi l}{\bar{k}}}\left\{I_\pm - 2\bar{k}iI_{13}^2\cos(\varphi/2)\right\}. \tag{D.1.17}$$

Absolute value of the scattering amplitude can be obtained

$$|f_1(\varphi)| = \frac{\lambda}{2}\sqrt{\frac{\pi l}{\bar{k}}}\left\{I_+^2 + 4\bar{k}^2(I_{13}^2\cos(\varphi/2))^2\right\}^{1/2}, \\ |f_2(\varphi)| = \frac{\lambda}{2}\sqrt{\frac{\pi l}{\bar{k}}}\left\{I_-^2 + 4\bar{k}^2(I_{13}^2\cos(\varphi/2))^2\right\}^{1/2}. \tag{D.1.18}$$

Differential cross section

The differential cross section given by

$$\frac{d\sigma}{d\varphi} = 2|f_1(\varphi)||f_2(\varphi)|. \tag{D.1.19}$$

Substitute the magnitude of the scattering amplitude (D.1.18) in to the differential cross section (D.1.19)

$$\frac{d\sigma}{d\varphi} = \frac{2\lambda^2\pi l}{4k}\left\{I_+^2 + 4\bar{k}^2(I_{13}^2\cos(\varphi/2))^2\right\}^{1/2} \times \left\{I_-^2 + 4\bar{k}^2(I_{13}^2\cos(\varphi/2))^2\right\}^{1/2}, \tag{D.1.20}$$

or more explicit form by inserting the value of $I_\pm$, we get the following expression

$$\begin{aligned}\frac{d\sigma}{d\varphi} = \frac{2\lambda^2\pi l}{4k}&\left\{(\lambda I_{06}^3 + [2I_{05}^1 - I_{05}^3])^2 + 4\bar{k}^2(I_{13}^2\cos(\varphi/2))^2\right\}^{1/2} \\ &\times \left\{(\lambda I_{06}^3 - [2I_{05}^1 - I_{05}^3])^2 + 4\bar{k}^2(I_{13}^2\cos(\varphi/2))^2\right\}^{1/2}.\end{aligned} \tag{D.1.21}$$

Integral entering into the electron differential cross section (D.1.21) are solved by mathematica and the results are shown below:

$$\begin{aligned} I_{06}^{(3)} &= \frac{q}{2}[K_1(q) - \frac{q}{4}K_2(q)], \\ I_{05}^{(1)} &= \frac{1+q}{3}\exp(-q), \quad I_{05}^{(3)} = \frac{2-q}{3}\exp(-q), \\ I_{13}^{(2)} &= \exp(-q), \end{aligned} \tag{D.1.22}$$

where K is the modified Bessel function. Inserting the results of these integrals in to (D.1.21) and let $L = 2\lambda^2\pi l$

$$\begin{aligned}\frac{1}{L}\frac{d\sigma}{d\varphi} = \frac{1}{4k}&\left\{(\frac{\lambda q}{2}[K_1(q) - \frac{q}{4}K_2(q)] + [2\frac{1+q}{3}\exp(-q) - \frac{2-q}{3}\exp(-q)])^2 + 4\bar{k}^2(\exp(-q)\cos(\varphi/2))^2\right. \\ &\times\left\{(\frac{\lambda q}{2}[K_1(q) - \frac{q}{4}K_2(q)] - [2\frac{1+q}{3}\exp(-q) - \frac{2-q}{3}\exp(-q)])^2 + 4\bar{k}^2(\exp(-q)\cos(\varphi/2))^2\right.\end{aligned} \tag{D.1.23}$$

simplify (D.1.23)

$$\frac{1}{L}\frac{d\sigma}{d\varphi} = \frac{1}{4k}\left\{\left\{\frac{\lambda q}{2}[K_1(q) - \frac{q}{4}K_2(q)] + q\exp(-q)\right\}^2 + 4\bar{k}^2\exp(-2q)\cos^2(\varphi/2)\right\}^{1/2} \times \left\{\left\{\frac{\lambda q}{2}[K_1(q) - \frac{q}{4}K_2(q)] - q\exp(-q)\right\}^2 + 4\bar{k}^2\exp(-2q)\cos^2(\varphi/2)\right\}^{1/2} \tag{D.1.24}$$

we have $q = 2\bar{k}sin(\varphi/2)$

$$\frac{1}{L}\frac{d\sigma}{d\varphi} = \frac{1}{4k}\left\{4\bar{k}^2sin^2(\varphi/2)\left\{\frac{\lambda}{2}[K_1(q) - \frac{q}{4}K_2(q)] + \exp(-q)\right\}^2 + 4\bar{k}^2\exp(-2q)\cos^2(\varphi/2)\right\}^{1/2} \times \left\{4\bar{k}^2sin^2(\varphi/2)\left\{\frac{\lambda}{2}[K_1(q) - \frac{q}{4}K_2(q)] - \exp(-q)\right\}^2 + 4\bar{k}^2\exp(-2q)\cos^2(\varphi/2)\right\}^{1/2} \tag{D.1.25}$$

taking $4\bar{k}^2$ common

$$\frac{1}{L}\frac{d\sigma}{d\varphi} = k\left\{\sin^2(\varphi/2)\left\{\frac{\lambda}{2}[K_1(q) - \frac{q}{4}K_2(q)] + \exp(-q)\right\}^2 + \exp(-2q)\cos^2(\varphi/2)\right\}^{1/2} \times \left\{\sin^2(\varphi/2)\left\{\frac{\lambda}{2}[K_1(q) - \frac{q}{4}K_2(q)] - \exp(-q)\right\}^2 + \exp(-2q)\cos^2(\varphi/2)\right\}^{1/2} \tag{D.1.26}$$

this can be rewritten as

where

$$A_\pm = \frac{\lambda}{2}[K_1(q) - \frac{q}{4}K_2(q)] \pm \exp(-q) \tag{D.1.27}$$

at $\varphi = \pi$, $\cos(\pi/2) = 0$ and $\sin(\pi/2) = 1$

$$\frac{1}{L}\frac{d\sigma}{d\varphi} = k\{A_+A_-\} \tag{D.1.28}$$

substitute A_+ and A_-

$$\frac{1}{L}\frac{d\sigma}{d\varphi} = k\left\{\frac{\lambda^2}{16}[2K_1(2\bar{k}) - \bar{k}K_2(2\bar{k})]^2 - \exp(-4\bar{k})\right\} \tag{D.1.29}$$

Magnetic Dipoles Parallel to the graphene plane

The vector potential of the magnetic dipole is oriented parallel to the graphene plane. We calculate the scattering amplitude and the differential cross section.

Potential

The expressions of $V_{1,2}^{\parallel,\perp}$ (D.1.1) with $\mathbf{A}$ and B_z by

$$\begin{aligned} A_x &= \frac{d}{l^2}\frac{\sin\alpha}{\bar{R}^3}, \quad A_y = -\frac{d}{l^2}\frac{\cos\alpha}{\bar{R}^3}, \\ A_z &= \frac{d}{l^2}\frac{y\cos\alpha - x\sin\alpha}{\bar{R}^3}, \quad B_z = 3\frac{d}{l^3}\frac{x\cos\alpha + y\sin\alpha}{\bar{R}^5}, \end{aligned} \tag{D.1.30}$$

where we set $\alpha = 0, \pi/2$, for magnetic dipole oriented parallel and perpendicular to incident beam of electrons respectively, can be written in the dimensionless form as

$$V_{1,2}^{\parallel} = \frac{\lambda}{\bar{R}^3}\left\{\frac{\lambda(1+y^2)}{\bar{R}^3} \mp 3\frac{x}{\bar{R}^2}\right\}, \tag{D.1.31}$$

$$V_{1,2}^{\perp} = \frac{\lambda}{\bar{R}^3}\left\{\frac{\lambda(1+x^2)}{\bar{R}^3} + 2\bar{k} \mp 3\frac{y}{\bar{R}^2}\right\}. \tag{D.1.32}$$

Scattering Amplitude

With the help (D.1.31) and (D.1.31) the scattering amplitudes (D.1.7) after passing to the coordinate system with the $y'-$ axis parallel to $\mathbf{q}$ like in the previous section,

we obtain the following integrals

$$f^{\parallel}_{1,2}(\varphi) = -\frac{\lambda}{4}\sqrt{\frac{l}{\pi\bar{k}}}\int_0^\infty dr' \int_0^{2\pi} d\phi' \exp(-i\bar{q}r'\cos\phi')\times \\ \left\{\frac{\lambda[r' + r'^3\cos^2(\phi' - \frac{\varphi}{2})]}{R'^6} \mp 3\frac{r'^2\sin(\phi' - \frac{\varphi}{2})}{R'^5}\right\}, \tag{D.1.33}$$

$$f^{\perp}_{1,2}(\varphi) = -\frac{\lambda}{4}\sqrt{\frac{l}{\pi\bar{k}}}\int_0^\infty dr' \int_0^{2\pi} d\phi' \exp(-i\bar{q}r'\cos\phi')\times \\ \left\{\frac{\lambda[r' + r'^3\sin^2(\phi' - \frac{\varphi}{2})]}{R'^6} + \frac{2\bar{k}r'}{R'^3} \mp 3\frac{r'^2\cos(\phi' - \varphi/2)}{R'^5}\right\}. \tag{D.1.34}$$

Integrals over φ' and r' in (D.1.33) and (D.1.34) can be written as in the form (D.1.14). The final results read

$$f^{\parallel}_{1,2}(\varphi) = -\frac{\lambda}{2}\sqrt{\frac{\pi l}{\bar{k}}}\left\{I_{\parallel}(\bar{q}) \mp 3iI^{(2)}_{15}(\bar{q})\sin\varphi/2\right\} \tag{D.1.35}$$

and

$$f^{\perp}_{1,2}(\varphi) = -\frac{\lambda}{2}\sqrt{\frac{\pi l}{\bar{k}}}\left\{I_{\perp}(\bar{q}) \pm 3iI^{(2)}_{15}(\bar{q})\cos\varphi/2\right\}. \tag{D.1.36}$$

Here

$$I_{\parallel}(\bar{q}) = \lambda[I^{(1)}_{06}(\bar{q}) - \frac{1}{\bar{q}}I^{(2)}_{16}\cos\varphi + I^{3}_{06}(\bar{q})\cos^2\varphi/2], \\ I_{\perp}(\bar{q}) = \lambda[I^{(1)}_{06}(\bar{q}) + \frac{1}{\bar{q}}I^{(2)}_{16}(\bar{q})\cos(\varphi) + I^{(3)}_{06}\sin^2\varphi/2] + 2\bar{k}I^{(1)}_{03}(\bar{q}). \tag{D.1.37}$$

The integrals in (D.1.37) can be solved using mathematica and given as follows:

A. The magnetic moment parallel to both the graphene plane incident beam of electrons:

$$I^{(3)}_{06} = \frac{\bar{q}}{2}[K_1(\bar{q}) - \frac{\bar{q}}{4}K_2(\bar{q})], \\ I^{(1)}_{05} = \frac{1+\bar{q}}{3}\exp(-\bar{q}), \quad I^{(3)}_{05} = \frac{2-\bar{q}}{3}\exp(-\bar{q}), \\ I^{(2)}_{13} = \exp(-\bar{q}). \tag{D.1.38}$$

B. The magnetic moment parallel to the graphene plane and parallel or perpendicular to the incident beam of electrons:

$$
\begin{aligned}
&I_{06}^{(1)} = \frac{\bar{q}^2}{8} K_2(\bar{q}), \quad I_{26}^{(3)} = \frac{\bar{q}^2}{8} K_0(\bar{q}), \\
&I_{15}^{(2)} = \frac{\bar{q}}{3} \exp(-\bar{q}), \quad I_{03}^{(1)} = \exp(-\bar{q}), \quad I_{16}^{(2)} = \frac{\bar{q}^2}{8} K_1(\bar{q}).
\end{aligned}
\tag{D.1.39}
$$

Differential cross section

The differential scattering cross sections by remote magnetic dipoles parallel and perpendicular to the incident beams of electrons in graphene according to (D.1.19) and (D.1.35), (D.1.36) with usage of (D.1.38) and (D.1.39) are given by

$$
\begin{aligned}
&\frac{1}{L}\frac{d\sigma_{\parallel}(\varphi)}{d\varphi} = \bar{k}\left\{\frac{\lambda^2}{64}[\bar{q}K_2(\bar{q})\sin^2\frac{\varphi}{2} + K_1(\bar{q})(2+\cos\varphi)]^2 + \exp(-2\bar{q})\sin^2\frac{\varphi}{2}\right\}\sin^2\frac{\varphi}{2}, \\
&\frac{1}{L}\frac{d\sigma_{\perp}(\varphi)}{d\varphi} = \bar{k}\left\{\left(\frac{\lambda}{8}\sin\frac{\varphi}{2}\left[\bar{q}K_2(\bar{q})\cos^2\frac{\varphi}{2} + K_1(\bar{q})(2-\cos\varphi)\right] + \exp(-\bar{q})\right)^2 + \frac{1}{4}\exp(-2\bar{q})\sin^2\varphi\right\}.
\end{aligned}
\tag{D.1.40}
$$

These formulas show that the backscattering cross section ($\varphi = \pi, \bar{q} = 2\bar{k}$) are nonzero in both cases

$$
\begin{aligned}
&\frac{1}{L}\frac{d\sigma_{\parallel}(\varphi)}{d\varphi} = \bar{k}\left\{\frac{\lambda^2}{64}[2\bar{k}K_2(2\bar{k}) + K_1(2\bar{k})]^2 + \exp(-4\bar{k})\right\}, \\
&\frac{1}{L}\frac{d\sigma_{\perp}(\varphi)}{d\varphi} = \bar{k}\left(\frac{3\lambda}{8}K_1(2\bar{k}) + \exp(-2\bar{k})\right)^2.
\end{aligned}
\tag{D.1.41}
$$

For $\bar{k} > 1$, the cross sections (D.1.40) are practically equal but they are small due the asymptotic behavior.

List of Publications and conferences

- Electron scattering in graphene by impurities with electric and magnetic dipole, *Yohannes A., V. N. Malnev, and Teshome Senbeta,, Physica E 60 (2014) 214- 219 2.*
- Electron scattering in graphene by impurities with electric and magnetic dipole, *Baku world Science Forum of Young Scientists 2014 , Baku, Azerbaijan.*
- Electron scattering in graphene by by remote Nanomagnet, *Research in science exposition "Science for Development" Addis Ababa university, Ethiopia*
- Quantum Hall effect in monolayer and bilayer graphene . *International conference on the School of science and Technology in University of Gondar, Ethiopia*
- Some Electronic properties of Monolayer graphene, *National conference of Ethiopian Physical science Society , Mekele University , Ethiopia*
- Electron scattering in graphene by impurities with electric and magnetic dipole, *National conference of Ethiopian Physical science Society , Addis Ababa university , Ethiopia*

Bibliography

[1] A.W. Moore, Highly Oriented Pyrolytic Graphite, Vol. 11. Marcel Dekker, NewYork, 1973.

[2] J. Heremans, C.H. Olk, G.L. Eesley, J. Steinbeck, and G. Dresselhaus, Phys. Rev. Lett. 60 (1988), p. 452

[3] Xuekun Lu, Hui Huang, Nikolay Nemchuk, and Rodney S. Ruoff , App. Phys. Lett. Vol. 75 no 2 (1999)

[4] Kroto H W, Heath J R, O'Brien S C, Curl R F and Smalley R E. C, Nature 318:162-3, 1985.

[5] Sumio lijima, Nature Vol. 354 (1991)

[6] Paul L. McEuen, Marc Bockrath, David H. Cobden, Young-Gui Yoon, and Steven G. Louie, Phys. Rev. Lett. Vol 85 no 24 (1999)

[7] M.S. Dresselhaus , G. Dresselhaus , A. Jorio , A.G. Souza Filho R. Saito, Carbon 40 (2002) 20432061

[8] Chenguo Hu , Yiyi Zhang , Gang Bao , Yuelan Zhang , Meilin Liu b , Zhong Lin Wang, Chemical Physics Letters 418 (2005) 520525

[9] E.N. Ganesh, ISSN: 2278-3075, Vol. 2, Issue-4 (2013)

[10] A. Jorio, M.S. Dresselhaus, and G. Dresselhaus, Carbon Nanotubes: Advanced Topics in the Synthesis, Structure, Properties and Applications, Vol. 111, Springer, Berlin, 2008.

[11] R. Saito, G. Dresselhaus, and M.S. Dresselhaus, Physical Properties of Carbon Nanotubes, Imperial College Press, London, 1998. London.

[12] S. Reich, C. Thomsen, and P. Ordejon, Elastic Properties and Pressure-induced Phase Transitions of Single-walled Carbon Nanotubes, Vol. 235, Wiley Online Library, 2003.

[13] M. Endo, M.S. Strano, and P.M. Ajayan, Carbon Nanotubes: Advanced Topics in the Synthesis, Structure, Properties and Applications, Vol. 111, Springer, Berlin, 2008.

[14] A. Jorio, R. Saito, G. Dresselhaus, and M.S. Dresselhaus, Raman Spectroscopy in Graphene Related Systems, Wiley-VCH Verlag GmbH and Co KGaA, Weinheim, Germany, 2010.

[15] P.R. Wallace, Phys. Rev. 71, 622 (1947) H.P. Boehm, A. Clauss,

[16] U. Hofmann, and G.O. Fischer, Z. Naturforschung B 17(3) (1962), p. 150.

[17] R. E. Peierls, Helv. Phys. Acta 7, 81 (1934).

[18] R. E. Peierls, Ann. Inst. Henri Poincare 5, 177 (1935).

[19] L. D. Landau, Phys. Z. Sowjetunion 11, 26 (1937).

[20] L. D. Landau and E. M. Lifshitz, Statistical Physics, Third Edition, Part 1: Volume 5, 3 ed. (Butterworth-Heinemann, 1980).

[21] N. D. Mermin, Phys. Rev. 176, 250 (1968).

[22] M.I. Katsnelson, A.K. Geim, Philos. Trans. R. Soc. A 366 (2008)195.

[23] K.S. Novoselov, A.K. Geim, S.V. Morozov, D. Jiang, Y. Zhang, S.V. Dubonos, I.V. Grigorieva, A.A. Firsov, Science 306, 666 (2004)

[24] A.K. Geim and K.S. Novoselov, Nat. Mater. 6(3) (2007), pp. 183191.

[25] A. Castro Neto, F. Guinea, N.M.R. Peres, K.S. Novoselov, and A.K. Geim, Rev. Mod. Phys. 81(1) (2009), pp. 109162.

[26] M.S. Dresselhaus and P.T. Araujo, ACS Nano 4(11) (2010), pp. 62976302.

[27] C. Lee, X. Wei, J.W. Kysar, and J. Hone, Science 321(5887) (2008), p. 385.

[28] A.A. Balandin and O.L. Lazarenkova, Appl. Phys. Lett. 82 (2003), p. 415. D.

[29] Teweldebrhan and A.A. Balandin, Appl. Phys. Lett. 94 (2009), p. 13101.

[30] K.I. Bolotin, K.J. Sikes, Z. Jiang, M. Klima, G. Fudenberg, J. Hone, P. Kim, and H.L. Stormer, Solid State Commun. 146(910) (2008), pp. 351355.

[31] S. Morozov, K. Novoselov, M. Katsnelson, F. Schedin, D. Elias, J. Jaszczak, and A. Geim, Phys. Rev. Lett. 100(1) (2008), p. 16602.

[32] B. Lee, Y. Chen, F. Duerr, D. Mastrogiovanni, E. Garfunkel, E.Y. Andrei, and V. Podzorov, Nano Lett. 10 (2010), pp. 14071433.

[33] X. Du, I. Skachko, A. Barker, and E.Y. Andrei, Nat. Nanotechnol. 3(8) (2008), pp. 491495.

[34] G. Li and E.Y. Andrei, Nat. Phys. 3 (2007), p. 623.

[35] X. Du,I. Skachko, F. Duerr, A. Luican, and E.Y. Andrei, Nature 462(2009), pp.192195.

[36] K.S. Novoselov, A.K. Geim, S.V. Morozov, D. Jiang, M.I. Katsnelson, I.V. Grigorieva, S.V. Dubonos, and A.A. Firsov, Nature 438(7065) (2005), pp. 197200.

[37] K.S. Novoselov, E. McCann, S.V. Morozov, V.I. Falko, M.I. Katsnelson, U. Zeitler, D. Jiang, F. Schedin, and A.K. Geim, Nat. Phys. 2(3) (2006), pp. 177180.

[38] Phaedon Avouris, Materialstoday (2012) VOL. 15 NO. 3

[39] A. F. Young and P. Kim, Annu. Rev. Condens. Matter Phys. 2011. 2:10120

[40] C.W.J. Beenakker, Rev. Mod. Phys. 80(4) (2008), pp. 13371354.

[41] M.I. Katsnelson, K.S. Novoselov, and A.K. Geim, Nat. Phys. 2(9) (2006), pp. 620 - 625.

[42] Vadim V. Cheianov and Vladimir I. Falko, PHYS. REV. B 74, 041403(R) (2006)

[43] J.M. Pereira Jr., V. Mlinar, F.M. Peeters, and P. Vasilopoulos, Phys. Rev. B 74(4) (2006), p. 45424.

[44] F. Miao, S. Wijeratne, Y. Zhang, U.C. Coskun, W. Bao, and C.N. Lau, Science 317(5844) (2007), pp. 15301533.

[45] A.K. Geim, Science (NewYork) 324(5934) (2009), pp. 15301534.

[46] Y.-M. Lin, C. Dimitrakopoulos, K. A. Jenkins, D. B. Farmer, H.-Y. Chiu, A. Grill, and Ph. Avouris, IBM T. J. Watson Research Center, Yorktown Heights, NY 10598

[47] Yu-Ming Lin, Keith A. Jenkins, Alberto Valdes-Garcia, Joshua P. Small, Damon B. Farmer, and Phaedon Avouris, IBM T. J. Watson Research Center, Yorktown Heights, NY 10598

[48] Xiaogan Liang, Zengli Fu, and Stephen Y. Chou*, Nano Lett. Vol. 7 No. 12 3840 3844 (2007)

[49] Viktor Ariel,

[50] Xiying Ma, Weixia Gu, Jiaoyan Shen and Yunhai Tang, Nanoscale Research Letters 2012, 7:677

[51] Beom Joon Kim, Jong-Hyun Ahn, Houk Jang, Seoung-Ki Lee, and Jeong Ho Cho, Byung Hee Hong, Nano Lett. 2010, 10, 34643466

[52] Frank schwierz, Naturenanotechnology Rev. Lett. Vol. 5 (2010)

[53] Javad Bavaghar Chahardeh, International Journal of Advanced Research in Computer and Communication Engineering Vol. 1, Issue 4 (2012)

[54] Mark P. Levendorf, and Jiwoong Park, Carlos S. Ruiz-Vargas, Shivank Garg, Nano Let. 2009 Vol. 9, no. 12 4479-4483

[55] Floriano Traversi, Valeria Russo, and Roman Sordan, App. Phys. Let.94, 223312 (2009)

[56] Ph. Avouris, Y-.M. Lin, F. Xia, D.B. Farmer, Y. Wu, T. Mueller, K. Jenkins, C. Dimitrakopoulos, A. Grill, IBM T.J. Watson Research Center, Yorktown Heights, NY 10598

[57] By Inanc Meric, Cory R. Dean, Nicholas Petrone, Lei Wang, James Hone, Philip Kim, and Kenneth L. Shepard, Proceedings of the IEEE Vol. 101, No. 7 (2013)

[58] Omid Habibpour, JosipVukusic, and Jan Stake, IEEE TRANSACTIONS ON MICROWAVE THEORY AND TECHNIQUES, VOL. 61, NO. 2,FEB. 2013 2.

[59] Yu-Ming Lin, Alberto Valdes-Garcia, Shu-Jen Han, Damon B. Farmer, Inanc Meric, Yanning Sun, Yanqing Wu, Christos Dimitrakopoulos, Alfred Grill, Phaedon Avouris, Keith A. Jenkins, SCIENCE 10 JUNE 2011 VOL 332

[60] Erica Guerriero, Laura Giorgia Rizzi, Laura Polloni, Eric Pop, Massimiliano Bianchi, and Roman Sordan, Ashkan Behnam, Enrique Carrion, American Chemical Society VOL.7 NO.6 , 5588 5594 (2013)

[61] Xuetao Gan, Ren-Jye Shiue,YuandaGao, Inanc Meric,TonyF.Heinz, Kenneth Shepar, James Hone, SolomonAssefa,and Dirk Englund, Nat. Rev.Lett., DOI: 10.1038/NPHOTON.2013.253

[62] Daniel Schall, Martin Otto, Daniel Neumaier and Heinrich Kurz, SCIENTIFIC REPORTS — 3 : 2592 — DOI: 10.1038/srep02592

[63] F. Bonaccorso, Z. Sun, T. Hasan and A. C. Ferrari, Nat. Rev. (2010) doi: 10.1038/nphoton.2010.186

[64] Qiaoliang Bao, and Kian Ping Loh, acsnano VOL. 6 NO. 5 36773694 (2012)

[65] Ming Liu, Xiaobo Yin, and Xiang Zhang, American Chemical Society Nano Lett. dx.doi.org/10.1021/nl204202k

[66] Dong Wook Chang, Hyun-Jung Choi, Alan Filer and Jong-Beom Baek, J. Mater. Chem. A, 2, 12136 (2014)

[67] Hyesung Park and Jing Kong, Jill A Rowehl, KiKangKim, Vladimir Bulovic, iop publishing, Nanotechnology 21 505204 (6pp) (2010)

[68] Kyuwook Ihm, Kyung-Jae Lee, Jong Tae Lim, Tai-Hee Kang, Sukmin Chung, Byung Hee Hong, and Geun Young Yeom, John and Wiley , Surf. Interface Anal, 44, 744748. (2011)

[69] Xiaochang Miao, Sefaattin Tongay, Andrew G. Rinzler, Maureen K. Petterson, Bill R. Appleton, and Arthur F. Hebard, Kara Berke, arXiv:1209.0432v1. [cond-mat.mtrl-sci] (2012)

[70] Riccardo Messina and Philippe Ben-Abdallah, scientific reports 3 : 1383 DOI: 10.1038/srep01383

[71] Marshall Cox, Philip Kim, Alon Gorodetsky, Colin Nuckolls, Bumjung Kim, and Ioannis Kymissis, Keun Soo Kim, Zhang Jia, App. Phys. Let. 98, 123303 (2011)

[72] Lewis Gomez De Arco, Yi Zhang, Cody W. Schlenker, Koungmin Ryu, Mark E. Thompson, and Chongwu Zhou, American chemical Society Vol. 4 No. 5 28652873 (2010)

[73] J.C. Slonczewski, P.R. Weiss, Phys. Rev. 109, 272 (1958)

[74] J.W. McClure, Phys. Rev. 108, 612 (1957)

[75] M.S Dresselhaus, G. Dresselhaus, Adv. Phys. 51, 1 (2010)

[76] D.P. DiVincenzo, E.J. Mele, Phys. Rev. B 29, 1685 (1984)

[77] J. Gonzalez, F. Guinea, M.A.H. Vozmediano, Phys. Rev. Lett. 69,172 (1992).

[78] H. Ajiki, T. Ando, J. Phys. Soc. Jpn. 62, 1255 (1993)

[79] C.L. Kane, E.J. Mele, Phys. Rev. Lett. 78, 1932 (1997)

[80] T. Ando, T. Nakanishi, R. Saito, J. Phys. Soc. Jpn. 67, 2857 (1998).

[81] P.L. McEuen, M. Bockrath, D.H. Cobden, Y.-G. Yoon, S.G. Louie, Phys. Rev. Lett. 83, 5098 (1999)

[82] R. Saito, M.S. Dresselhaus, G. Dresselhaus, Physical Properties of Carbon Nanotubes, (Imperial College Press, London, 1998)

[83] G.W. Semeno, Phys. Rev. Lett. 53, 2449 (1984)

[84] F.D.M. Haldane, Phys. Rev. Lett. 61, 2015 (1988)

[85] Y.B. Zhang, Y.W. Tan, H.L. Stormer, P. Kim, Nature 438, 201 (2005)

[86] N.W. Ashcroft, N.D. Mermin, Solid-State Physics, (Brooks/Cole, Belmont, 1976)

[87] C. Bena, G. Montambaux, New J. Phys. 11, 095003 (2009)

[88] Das Sarma, S.,Shafque Adam, E. H. Hwang, and E. Rossi, Mod. Phys. Rev. Vol.83, 2011.

[89] K. Sasaki, S. Murakami, R. Saito, Appl. Phys. Lett. 88, 113110 (2006)

[90] N.M.R. Peres, F. Guinea, A.H. Castro Neto, Phys. Rev. B 73, 125411(2006)

[91] E. McCann, V.I. Falko, Phys. Rev. Lett. 96, 086805 (2006)

[92] S.B. Trickey, F. Muller-Plathe, G.H.F. Diercksen, J.C. Boettger, Phys. Rev. B 45, 4460 (1992)

[93] J.R. Schrieffer, P. A. Wolff, Phys. Rev. 149, 491 (1966) O.

[94] Klein, Zeitschrift fr Physik 53, 157 (1929).

[95] Viktor Ariel, arXiv :1205.3995v1 [physics.gen-ph] 14 May 2012

[96] Viktor Ariel and Amir Natan, arXiv : 1206.6100v2 [physics.gen-ph] 12 Aug 2012

[97] Vincent E. Dorgan, Myung-Ho Bae, and Eric Pop, APPLIED PHYSICS LETTERS 97, 082112 (2010)

[98] V. Ryzhii and A. Satou, T. Otsuji, JOURNAL OF APPLIED PHYSICS 101, 024509 (2007)

[99] M.I. Katsnelson, *Graphene, Carbon in Two dimensions*, Cambridge University Press, 2012.

[100] L. D. Landau and E. M. Lifshits, *Quantum Mechanics (Nonrelativistic Theory)*, Elsevier, Oxford, 1977.

[101] L.D.Landau, Z. Phys. 64, 629 (1930) 40.

[102] K. von Klitzing, G. Dorda, M. Pepper, Phys. Rev. Lett. 45, 494 (1980) 41.

[103] R.E. Prange, S.M. Girvin (eds.), The Quantum Hall Effect, (Springer-Verlag, New York, 1986) 42.

[104] A.H. MacDonald (ed.), Quantum Hall Eect: A Perspective, (Kluwer, Boston, 1989) 43.

[105] J.W. McClure, Phys. Rev. 104, 666 (1956) 44.

[106] H.J. Fischbeck, Phys. Status Solidi 38, 11 (1970) 45.

[107] Y. Zheng, T. Ando, Phys. Rev. B 65, 245420 (2002) 46.

[108] V.P. Gusynin, S.G. Sharapov, Phys. Rev. Lett. 95, 146801 (2005) 47.

[109] I.F. Herbut, Phys. Rev. B 75, 165411 (2007) 48.

[110] L.M. Lifshitz, Zh. Exp. Teor. Fiz. , 1565 (1960) Sov. Phys. JETP , 1130

[111] G.B. Arfken, H.J. Weber, *Mathematical Methods for Physicists*, Elsevir Science, 2001.

[112] D.S. Novikov, Phys.Rev. B **76**, 245435(2007).

[113] Ando, T., Fowler, A. B. and Stern, F. 1982 Electronic properties of two-dimensional systems. Rev. Mod. Phys. 54, 437672. (doi:10.1103/RevModPhys.54.437)

[114] John H. Davies, *The Physics of low-dimensional semiconductors*, Cambridge University Press, 1998.

[115] T. Ando, J. Phys. Soc. Jpn. **75**, 074716(2006).

[116] K.Nomura and A.H. Macdonald, Phys.Rev. Lett.**96**, 256602(2006)

[117] E.H. Hwang, S. Adam, and S. Das Sarma, Phys.Rev. Lett.**98**, 186806(2007).

[118] Mikito Koshino amd Tsuneya Ando, arXiv:cond-mat/0606166v1 [cond-mat.mes-hall] 7 June 2006.

[119] A. Tiwari, et al., Appl. Phys. Lett. **88**, 142511 (2006).

[120] V.N. Mal'nev and Teshome Senbeta, Magnetism and Magnetic Materials, **323**, 1581(2011).

[121] V.N. Malnev, Teshome Senbeta, Yahannes Anchenfe, Physica E 2014, 60, 214-219.

[122] Kabir, M.; Kanhere,D. G.; and Mookerjee, A. Phys. Rev. B. 2006, 73, 075210-1 - 075210-4.

[123] Liu, L.; Guo, G. Y.; Jayanthi, C. S.; Wu, S. Y. Phys. Rev. Lett. 2002, 88, 217206-1 - 217206-4.

[124] P.S. Novikov, Phys. Rev. B. 2006, 245935.

[125] A. Jablonski, F. Salvat and C. J. Powell, J. Phys. Chem. Ref. Data,Vol. 33, No. 2, 2004

[126] Alex Zazunov, Arijit Kundu, Artur Hutten, and Reinhold Egger.Phys. Rev. B 82, 155431, 2010

DECLARATION

I hereby declare that this thesis is my original work and has not been presented for a degree in any other University. All sources of material used for the thesis have been duly acknowledged.

Name: Yohannes Achenefe
Email: y.achenefe@yahoo.com

This thesis has been submitted for examination with my approval as University advisor.

Prof. V. N. Malnev
Addis Ababa University